

Well-ordered iron oxide and sulfide thin films: growth methods and characterisation

vorgelegt von
Master of Science
Earl Matthew Davis
geb. in London

von der Fakultät II - Mathematik und Naturwissenschaften
der Technischen Universität Berlin
zur Erlangung des akademischen Grades

Doktor der Naturwissenschaften
Dr.rer.nat.

genehmigte Dissertation

Promotionsausschuss:

Vorsitzende: Prof. Dr. Kathy Lüdge
Gutachter: Prof. Dr. Hans-Joachim Freund
Gutachter: Prof. Dr. Mario Dähne

Tag der wissenschaftlichen Aussprache: 20. November 2018

Berlin 2018

Contents

List of Tables	v
List of Figures	vi
Acknowledgments	viii
Abstract	x
Zusammenfassung	xi
Abbreviations	xii
Chapter 1 Introduction	1
1.1 Surface science for catalysis	1
1.2 Thin film growth	3
1.2.1 Growth modes	3
1.2.2 Substrate choice	5
1.2.3 Surface reconstruction	6
1.3 Fe ₃ O ₄	7
1.3.1 Structure	8
1.4 Iron sulfides	10
1.5 Thesis organisation	12
Chapter 2 Experimental Methods	14
2.1 X-ray photoelectron spectroscopy	14
2.1.1 Features of an XPS spectrum	16
2.1.2 Quantification from XPS	21
2.1.3 Calibration	22

2.2	Scanning tunnelling microscopy	23
2.2.1	Principle of operation	24
2.2.2	Experimental set-up	25
2.2.3	Image processing	26
2.3	Low energy electron diffraction	27
2.3.1	Diffraction conditions	27
2.3.2	Ewald construction	29
2.3.3	Experimental setup	29
2.3.4	Interpretation of LEED patterns	31
2.4	X-ray diffraction	32
Chapter 3 Theoretical Methods		35
3.1	I/V-LEED	35
3.1.1	Principles	36
3.1.2	Comparing theory and experiment	42
3.1.3	Search algorithms	43
Chapter 4 Fe₃O₄(001) Growth on Pt(001)		47
4.1	Introduction	47
4.2	Experimental details	48
4.3	Results and analysis	48
4.4	Conclusions	57
Chapter 5 Iron Sulfide Growth		58
5.1	Introduction	58
5.2	Growth chamber	58
5.3	Iron and sulfur sources	59
5.4	Choosing a substrate	61
5.4.1	Pt(111)	61
5.4.2	Pt(001)	63
5.4.3	Au(111)	72
5.5	Conclusions	75
Chapter 6 Iron Sulfide Film Characterisation		76
6.1	Introduction	76

6.2	XPS	76
6.2.1	Fe 2p	77
6.2.2	S 2p	78
6.3	STM	81
6.4	I/V-LEED	85
6.5	X-ray diffraction	92
6.6	Conclusions	95
Chapter 7 Summary and Conclusions		96
Bibliography		97

List of Tables

1.1	Table showing various iron sulfides	11
6.1	Table of x-ray photoelectron spectroscopy (XPS) Fe 2p peak assignments	78
6.2	Table showing R-factors from bulk greigite $\text{Fe}_3\text{S}_4(111)$ terminations	88
6.3	Table showing R-factors from bulk pyrite $\text{FeS}_2(111)$ terminations	89
6.4	Table showing the intensities of the measured and calculated x-ray diffraction (XRD) reflections	93
6.5	Table showing the refined atomic positions of the best fit to the XRD measurements	94

List of Figures

1.1	Catalysis potential energy diagram	2
1.2	Thin film growth modes	4
1.3	Schematic of film island on substrate	5
1.4	Fe_3O_4 structure and surface terminations	8
2.1	Universal curve for attenuation length	15
2.2	XPS schematic	15
2.3	Example XPS spectrum	17
2.4	XPS energy level diagram	23
2.5	Electron tunnelling through barrier	24
2.6	STM schematic	26
2.7	Bragg diffraction	28
2.8	Ewald construction in 2D	30
2.9	Schematic of LEED experimental setup	30
2.10	Ewald construction in 2D	34
3.1	Flow chart of I/V-LEED procedure	36
3.2	Reflected LEED intensities from 1D crystal	38
3.3	Representation of multiple scattering processes in low energy electron diffraction (LEED)	39
3.4	Heirarchy of I/V-LEED calculations	40
3.5	Phase shift of electron above potential well	41
4.1	LEED images from $\text{Fe}_3\text{O}_4(001)$ growth	50
4.2	STM images of $\text{Fe}_3\text{O}_4(111)$ film on $\text{Pt}(001)$	51
4.3	STM images of B-terminated $\text{Fe}_3\text{O}_4(001)$	51
4.4	STM images of mixed Fe_3O_4 film orientations	52

4.5	STM and LEED images of $\text{Fe}_3\text{O}_4(001)$ film grown in high O_2 pressure	53
4.6	STM images of dimer-terminated $\text{Fe}_3\text{O}_4(001)$	54
4.7	STM images of intermediate terminations of $\text{Fe}_3\text{O}_4(001)$. . .	54
4.8	STM images of metastable intermediate terminations $\text{Fe}_3\text{O}_4(001)$	56
5.1	Photograph of corrosion of Cu gaskets caused by sulfur	59
5.2	Electrochemical sulfur cell schematic	60
5.3	First sulfide film growth attempt on $\text{Pt}(111)$	62
5.4	Second sulfide film growth attempt on $\text{Pt}(111)$	64
5.5	First iron sulfide film growth attempts on $\text{Pt}(001)$	65
5.6	Film growth on $\text{Pt}(001)$ using reduced S deposition rates . . .	67
5.7	First iron sulfide film growth on $\text{Pt}(001)$ in second ultra-high vacuum (UHV) chamber	67
5.8	Iron sulfide film grown on $\text{Pt}(001)$ with buffer layer	68
5.9	LEED and XPS from iron sulfide film annealed in S_2	69
5.10	LEED and XPS from iron sulfide films grown at 775 K	70
5.11	TPD showing decomposition of iron sulfide film on $\text{Pt}(001)$.	71
5.12	LEED of iron sulfide film grown at 625 K on $\text{Pt}(001)$	72
5.13	LEED patterns from iron sulfide film growth on $\text{Au}(111)$. . .	73
5.14	LEED and XPS of iron sulfide film following annealing in S_2 and then UHV	74
5.15	Reconstructed LEED pattern following Fe deposition of film .	75
6.1	Fe 2p peak from XPS spectrum of iron sulfide film	77
6.2	S 2p peaks of XPS spectra from iron sulfide film	80
6.3	Large scale STM images from iron sulfide film	81
6.4	Atomic resolution STM images from iron sulfide film	83
6.5	STM images showing surface orientation across terraces	84
6.6	STM images showing domain boundaries and effect of bias changes	84
6.7	Diagrams showing symmetry of the LEED pattern and of the P3m1 unit cell	87
6.8	$\text{Fe}_3\text{S}_4(111)$ unit cell and layer labels	89
6.9	I/V-LEED curves from the reconstructed greigite surface . . .	92
6.10	NiAs structure of iron sulfide film	94

Acknowledgments

My first thanks must go to Professor Freund for the opportunity to study for my PhD in such a world-class institution, and for all of the support throughout my time here. I would also like to thank my group leader, Helmut Kühlenbeck for his continual guidance during my studies and for many interesting conversations along the way. Thanks also go to Shamil Shaikhutdinov for his role in the first few months of my PhD while studying iron oxides.

I cannot go without thanking various staff members for their technical support. Matthias Naschitzki has given reliable assistance in many aspects throughout my time here, and without the experience of Klaus-Peter Vogelgesang, building the sulfur source for iron sulfide films would have been much more troublesome. Moreover, I have received invaluable support from Walter Wachsmann and Uwe Härtel over the course of my PhD. Additional thanks are extended to Andreas Stierle for allowing me to do an XRD experiment in his group at DESY, and Vedran Vonk and Simon Geile for their help in finally solving the structure of my iron sulfide film.

I have had the pleasure of working alongside many colleagues, both within and outside of my working group. My experience has been greatly enriched by your presence! Special thanks to Francesca Mirabella, who has been my office buddy since we both started and finished our PhDs within a couple of months of each other, going through many ups and downs over the years. Stefanie Stuckenholtz helped me to get settled into the department,

along with Christin Büchner. Yi Cui taught me how to use STM, while Felix Feiten helped with measuring IV-LEED curves and the spot-tracking program. Kristin Werner has been a good friend and lunch buddy since her arrival, and I've also enjoyed working with, and having tea-breaks with, many other colleagues during my studies. A special mention to Wolf-Dieter Schneider, with whom I enjoyed many intense games of table football while at the annual department seminar in Schloss Ringberg.

Away from work, I have received much love and support from my family in London, who I know I can always turn to, and who I've grown closer to over the past couple of years despite the distance. I must also thank my church family at International Baptist Church Berlin for support, prayer, and a place that I've been able to call home and have been able to build treasured relationships. It's also the place where I met my now wife, Vilma, who has been gracious and loving to me beyond what words can describe, and with whom I'm looking forward to spending a whole lifetime. *Te amo mi preciosa.*

Lastly, but most importantly, I thank God for His grace, mercy, and love in transforming my life, and for creating this world that I have the pleasure of studying with the tools He has given me.



Abstract

In this thesis, the growth of iron oxide and iron sulfide thin films has been investigated. These are materials that are abundantly found in the earth's crust and have long been studied by humanity, having a wide range of properties that have seen their use in many applications.

Among these applications, iron oxides have played an important role in catalytic processes such as the Haber-Bosch process. Surface science techniques are applied to gain insight into structure and reactivity at the atomic scale. Some of these techniques require a single-crystalline thin film. In this thesis, a growth recipe for high-quality $\text{Fe}_3\text{O}_4(001)$ thin films on a $\text{Pt}(001)$ substrate is presented. Additionally, it was discovered that the surface termination of $\text{Fe}_3\text{O}_4(001)$ thin films can be tuned via different thicknesses of a buffer layer included in the growth process.

Iron sulfides play a role in many biogeochemical processes, as well as being involved in industrial processes such as froth flotation. Furthermore, their presence in various locales such as undersea hydrothermal vents and iron-sulfur reaction centres in various enzymes have led to speculation that iron sulfides were involved in processes leading to the first metabolic organisms. Despite the interest in iron sulfides coming from many areas of science, surface science studies of their surfaces are rare. With the exception of pyrite (FeS_2), the production of high-quality single-crystalline samples is difficult. This thesis presents a reproducible growth recipe that allows well-ordered iron sulfide thin films to be prepared and studied using surface science techniques. Furthermore, surface science techniques and x-ray diffraction (XRD) are used in characterising the thin film, revealing a NiAs structure with an Fe occupancy of 77 %.

Zusammenfassung

In dieser Thesis wurde das Wachstum von dünnen Eisenoxid- und -sulfidfilmen untersucht. Diese Materialien sind wesentliche Bestandteile der Erdkruste und werden seit langem wissenschaftlich studiert. Vielfältige Anwendungen ergeben sich aus einem weiten Bereich von Eigenschaften.

Einer der Anwendungen von Eisenoxid ist der Einsatz in Katalysatoren, wie in dem des Haber-Bosch-Verfahrens. Zum Studium der Reaktivität und der Struktur auf mikroskopischer Skala wurden oberflächenphysikalische Methoden eingesetzt. Einige dieser Methoden erfordern einkristalline dünne Filme. In dieser Thesis wird eine Methode für die Präparation von $\text{Fe}_3\text{O}_4(001)$ -Filmen auf $\text{Pt}(001)$ vorgestellt. Es wird gezeigt, dass die Oberflächenterminierung des $\text{Fe}_3\text{O}_4(001)$ -Films durch Änderung der Dicke der Eisenlage, die als Puffer zwischen der Unterlage und dem Film dient, modifiziert werden kann.

Eisensulfide spielen eine Rolle in vielen biogeochemischen Prozessen und auch in industriell-technischen Prozessen wie der Schaumflotation. Sie finden sich in vielen geologischen Lokalitäten, wie zum Beispiel in der Nähe von unterseeischen hydrothermalen Quellen, aber auch als Eisen-Schwefel-Reaktionszentren in verschiedenen Enzymen, was zu der Spekulationen geführt hat, dass sie in Prozessen involviert waren, die zu den ersten metabolischen Organismen geführt haben. Oberflächenchemische Studien von Eisensulfiden sind selten, obwohl sie von Interesse in verschiedenen wissenschaftlichen Bereichen sind. Eine Ausnahme ist Pyrit (FeS_2), für das hochqualitative einkristalline Proben nur schwierig herzustellen sind. In dieser Thesis wird eine Methode zum reproduzierbaren Wachstum von wohlgeordneten Eisensulfidfilmen vorgestellt. Die Filme wurden mit verschiedenen oberflächenphysikalischen Methoden sowie mit Röntgenbeugung (XRD) untersucht. Die Röntgenbeugungsdaten zeigen, dass die Filme eine NiAs-artige Volumenstruktur mit einer Besetzungswahrscheinlichkeit der Eisenplätze von 77% aufweisen.

Abbreviations

AES	Auger electron spectroscopy
DE	differential evolution
DFT	density functional theory
DOS	density of states
FFT	fast Fourier transform
FM	Frank-van der Merve
FWHM	full-width at half-maximum
HREELS	high resolution electron energy loss spectroscopy
IMFP	inelastic mean free path
I/V-curve	intensity-voltage curve
I/V-LEED	intensity-voltage LEED
LEED	low energy electron diffraction
MBE	molecular beam epitaxy
MCP	microchannel plate
ML	monolayer
QMB	quartz microbalance
QMS	quadropole mass spectrometer
RFS	renormalised forward scattering
SCV	subsurface cation vacancy
SK	Stranski-Krastanov
STM	scanning tunnelling microscopy
TPD	temperature programmed desorption
UHV	ultra-high vacuum

VBM	valence band maximum
VW	Vollmer-Weber
XPS	x-ray photoelectron spectroscopy
XRD	x-ray diffraction

Chapter 1

Introduction

The study of surfaces plays a key role in the understanding of many physical phenomena. In recent decades, since the invention of surface science techniques such as x-ray photoelectron spectroscopy (XPS) and low energy electron diffraction (LEED), as well as the development of ultra-high vacuum (UHV) systems, great contributions have been made to many branches of modern research. Modern surface science deals principally with well-defined crystal surfaces, which are either free of adsorbates or are intentionally covered with a controlled amount. While surface science finds many applications in a diverse array of fields, in this thesis the primary motivation involves the preparation and characterisation of surfaces in order to understand chemical reactions for the purpose of catalysis.

1.1 Surface science for catalysis

Catalysis is used throughout industry for the enhancement of chemical processes. A catalyst decreases the energy required (the activation energy E_a) for a reaction to take place, as shown in the potential energy diagram in Figure 1.1, while not being consumed [1]. This has the effect of increasing the reaction rate and reducing the energetic cost of the reaction. Catalysis is involved in the processing of more than 80 % of all manufactured products [2], therefore it is easy to see that the improvement of existing catalysts and the discovery of better catalysts is an important goal of surface science research.

Heterogeneous catalysis, where the physical state of the catalyst is dif-

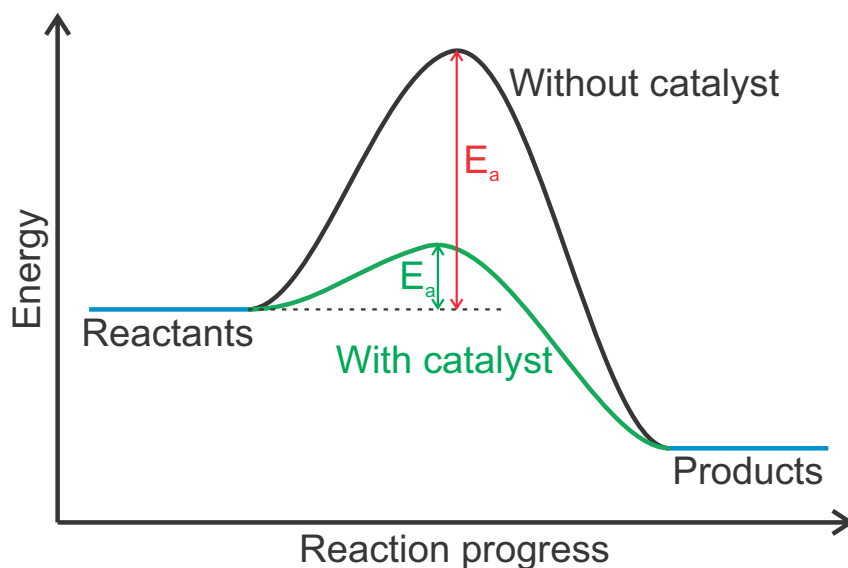


Figure 1.1: Simplified potential energy diagram showing how the presence of a catalyst opens a reaction pathway between the reactants and the products with a smaller activation energy E_a .

ferent from that of the reagents, typically uses a solid catalyst with liquid or gaseous reactants and products. The reaction occurs at the surface of the catalyst, therefore to maximise the catalytic activity per mass of a catalyst such catalysts are usually in the form of powders, pellets, or oxide-supported nanoparticles. This increases the total surface area, and therefore the catalytic activity.

Many catalysts are developed in a trial-and-error approach, without fundamental understanding of the physical processes occurring at the atomic scale. Indeed, the size and complexity of the catalysts and the reaction conditions prohibit their study at such a scale using current technology, despite the fact that such knowledge of the processes could be of great benefit to the design, enhancement, and development of future catalysts. To overcome the obstacles presented, a surface science approach is taken [3, 4]. The complexity is reduced by the use of model systems, and studies are performed under UHV conditions to ensure that characterisation of the surfaces and mechanisms can occur without contamination. Single crystals and epitaxial thin films often expose the same surfaces as nanoparticles used in catalysis, therefore their use in model systems allows a study of how particular facets of the catalyst

contribute to reactions. From the study of the most simple model, once it has been characterised and understood at the atomic level, additional complexity can then be added to the system in the form of nanoparticles or molecules adsorbed on the surface [4–6].

1.2 Thin film growth

In many cases, using thin films for the studies of the crystal surfaces is advantageous [7]. Many materials may be difficult to produce as a stand-alone single crystal to a size that can be analysed using surface science. Epitaxial growth on a substrate may permit this by providing a template for growth. Many support materials are also insulating in bulk, however by using thin films it is possible to replenish charge via the substrate to enable investigation using electron spectroscopies, for example. Methods of preparing such thin films for the use of surface science to investigate their catalytic activity is therefore an important field of investigation [8].

1.2.1 Growth modes

Epitaxial growth of crystalline thin films can generally be divided into three principal modes (illustrated in Figure 1.2) and can be understood through the interplay of the interface and surface energies [9, 10]. The first growth mode is called layer-by-layer, or Frank-van der Merwe (FM) (Figure 1.2(a)). In this case, atoms that are deposited are bound more strongly to the substrate than to each other. Due to this, each layer is completed before the next layer begins to grow, leading to two-dimensional growth.

The second growth mode is known as island growth, or Vollmer-Weber (VW) (Figure 1.2(c)). In this instance, the deposited atoms are most strongly bound to each other, and in order to maximise this interaction they nucleate and form three-dimensional islands on the substrate surface.

Finally, an intermediate case of the above two modes called layer-plus-island, or Stranski-Krastanov (SK), growth can occur (Figure 1.2(b)). Following the completion of one or several complete two-dimensional layers of FM growth, the binding energy of atoms to this layer decreases such that VW

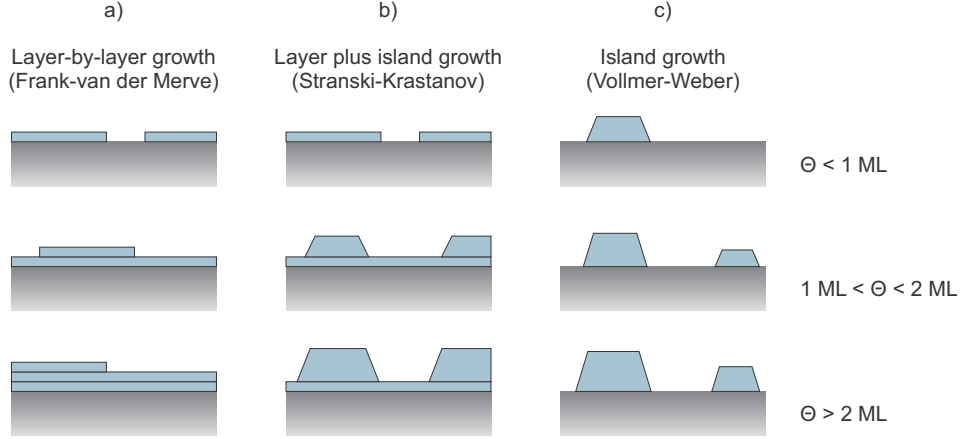


Figure 1.2: A schematic representation of the three important growth modes for different film coverages Θ in monolayers (MLs): (a) layer-by-layer (Frank-van der Merve) growth, (b) layer plus island (Stranski-Krastanov) growth, and (c) island (Vollmer-Weber) growth.

island growth becomes more favourable.

These conditions can be distinguished through consideration of surface and interface energies γ_i , i.e. the free energies required to create a surface or interface per unit area. As depicted in Figure 1.3, if the wetting angle of the atoms on the surface is θ , then equilibrium at the point where the film and the substrate touch is reached when

$$\gamma_S = \gamma_{F/S} + \gamma_F \cos \theta, \quad (1.1)$$

where γ_S , $\gamma_{F/S}$, and γ_F are the free energies of the substrate-vacuum, substrate-film, and film-vacuum interfaces, respectively.

The cases can be differentiated through examination of the free energies when $\theta = 0$. In the condition where

$$\gamma_S \geq \gamma_{F/S} + \gamma_F, \quad (1.2)$$

γ_S will be minimised by the film staying flat and FM growth occurs, whereas if

$$\gamma_S < \gamma_{F/S} + \gamma_F, \quad (1.3)$$

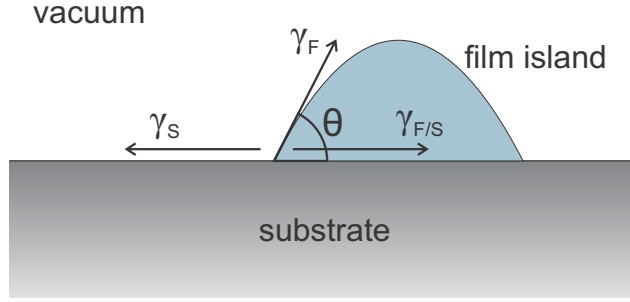


Figure 1.3: Schematic representation of the free energies involved for a film island on a substrate. γ_S , $\gamma_{F/S}$, and γ_F are the free energies of the substrate-vacuum, substrate-film, and film-vacuum interfaces, respectively.

the area of γ_S is maximised by having VW growth occur i.e. θ increases. For SK growth, initially condition 1.2 is realised and FM growth ensues, however as the intermediate layer is formed, the values of γ_S and $\gamma_{F/S}$ are altered such that condition 1.3 is fulfilled and VW growth takes place. Of the three growth modes, FM growth produces the most atomically flat surfaces, i.e. the best surfaces for study using surface science techniques.

Kinetic effects also have a role in determining how the growth of the thin film proceeds. Factors such as temperature influence how easily atoms can be transported across the surface, thereby affecting the probability of an atom finding the energetically optimal site. For example, film growth often takes place at elevated temperatures to ensure that atoms have enough kinetic energy to reach the substrate layer to produce FM growth. Alternatively, annealing steps can be incorporated in the preparation.

1.2.2 Substrate choice

The choice of substrate is also instrumental in achieving well-ordered growth of crystalline films. As shown in Section 1.2.1, minimising the energy required to form the substrate-film interface, and therefore encouraging FM growth, is critical in the formation of well-ordered crystalline films. One of the decisive factors determining this is the lattice mismatch between the substrate surface and the film.

Because the substrate is usually a different material than the film, the lattice constant will most likely be different. This lattice mismatch ϵ is usually

given by

$$\epsilon = \frac{b - a}{a}, \quad (1.4)$$

where a and b are lattice constants of the substrate surface and the film. The higher the lattice mismatch, the greater the energetic cost of the surface-film interface. A small mismatch can be accommodated by straining the lattice of the film in the plane of the interface, though this energy cost increases linearly as the film thickness increases. Dislocations can occur within the film in order to relax the strain. Where the lattice mismatch is high, the growth will either be incommensurate, leading to more disorder within the film, in the VW growth mode, or amorphous.

1.2.3 Surface reconstruction

The surface of a crystal represents a break in the 3D periodicity of the crystal lattice. As such, the local environment of the atoms in the terminating plane differs greatly from those in the bulk, with missing bonds in the direction above the plane. Due to this modification of the forces acting upon the surface atoms, the equilibrium structure of the top atomic layer will be different from that of the corresponding layer within the crystal bulk. This results in either relaxation or reconstruction.

In the case of surface relaxation, the structure of the atomic layers is conserved, however the interlayer distances are modified. Usually, this relaxation takes the form of a compression (or extension) in the direction normal to the surface plane. In some cases, however, there can be a lateral shift. Relaxation normal to the surface often extends to several atomic layers in a damped, oscillatory fashion.

The case where the atomic structure of the topmost layer (or layers) is modified is known as reconstruction. This can take many forms. In some cases, it may simply be lateral shifts of surface atoms within the unit cell, whereas in more extreme cases the number of atoms in the reconstructed layer is changed in comparison with the bulk. In most cases, surface reconstructions exhibit symmetry and periodicity different from those of the bulk. If this is the case, the reconstruction is described by its 2D unit cell relative to that of the bulk e.g. if the reconstructed unit cell has lattice vectors twice as large as

those of the bulk it is termed a (2×2) reconstruction.

For ionic crystal surfaces, Tasker [11] developed a method of determining whether the surface would exhibit relaxation or reconstruction by looking at charges in layers, or groups of layers, of the crystal. He found that where there is a dipole moment perpendicular to the surface within the repeat unit of the charged layers, the surface energy becomes very large. A surface reconstruction therefore becomes a likely mode by which the surface may be stabilised.

1.3 Fe_3O_4

Iron oxides are some of the most abundant minerals found on earth, with a number of phases commonly found existing as naturally grown crystals such as FeO (wüstite), Fe_3O_4 (magnetite), and Fe_2O_3 (hematite, maghemite). Of these, magnetite is one of the most copious, and therefore cheap, and is used as a catalyst in many industrial processes such as the Haber-Bosch, water-gas shift, and Fischer-Tropsch processes [12–14]. The magnetic properties of magnetite have been known to man for millennia, being written about by Greek philosophers around 800 BC, and used as a type of compass in China as early as the third century BC [15]. Magnetite has many properties of interest, for example it undergoes the Verwey transition [16], is ferrimagnetic [17], and is predicted to be semi-metallic at room temperature [18–20], however, only in recent years have magnetite surfaces been studied extensively [21]. This is due to their potential and actual applications in fields such as magnetic data storage and, as mentioned above, as catalysts.

In this thesis, understanding the surface reactivity for application in catalysis is the main motivation. Single crystal surfaces and thin films are required in order to understand the structure and chemistry of such surfaces. Although passivating oxide layers form readily on iron metal surfaces, these often exhibit complex stoichiometry dependent on preparation conditions, and are generally not well-ordered. In order to overcome this, growth of well-ordered crystalline films has been developed to facilitate surface science investigations [8].

To date, the close packed surfaces of iron oxides, such as $\text{Fe}_3\text{O}_4(111)$

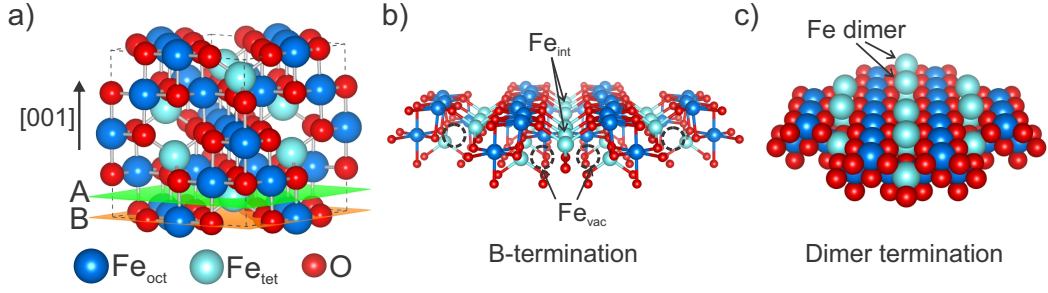


Figure 1.4: a) Cubic inverse spinel structure of Fe_3O_4 showing alternating layers labelled A and B, b) B-termination of Fe_3O_4 as resolved by Blum et al. [23] with an ordered array of SCVs (dashed circles, Fe_{vac}) and additional interstitial tetrahedrally-coordinated Fe atoms (Fe_{int}), c) dimer termination as proposed by Spiridis et al [24].

and $\text{Fe}_2\text{O}_3(0001)$, have received the majority of attention in research. However, due to recent studies suggesting a large difference in reactivity between the $\text{Fe}_3\text{O}_4(111)$ and (001) surfaces, more effort has been directed toward understanding the (001) surface [22].

1.3.1 Structure

Fe_3O_4 crystallises in the cubic inverse spinel structure with 56 atoms in the unit cell as shown in Figure 1.4(a). This consists of a cubic close packed array of 32 O^{2-} anions and a mixture of 16 Fe^{3+} and 8 Fe^{2+} cations in interstitial sites. The Fe^{2+} ions occupy half of the octahedral sites within the structure, and the Fe^{3+} ions occupy the remaining octahedral sites and the tetrahedral sites. Along the $[001]$ direction of the crystal lattice, the structure consists of two alternating layers of tetrahedrally coordinated iron atoms, known as A-layers, and mixed octahedrally coordinated iron and oxygen layers, termed B-layers, with a 90° rotation between each pair of layers.

$\text{Fe}_3\text{O}_4(001)$ surfaces have been found to exhibit a $(\sqrt{2} \times \sqrt{2})\text{R}45^\circ$ reconstruction, which was initially understood in terms of charge neutrality being a driving force under the formulation given by Tasker, as mentioned above, or in terms of autocompensation of covalent bonds [25]. The autocompensation approach led to models with either a half-filled A-layer or with a modified

distribution of charges and O-vacancies within a B-layer termination [26–29]. In fact, scanning tunnelling microscopy (STM) images of $\text{Fe}_3\text{O}_4(001)$ surfaces showed two apparently different terminations which were highly dependent on surface preparation conditions but do not appear together [8].

Later density functional theory (DFT) calculations led to an interpretation of the most stable surface reconstruction being a modified B-layer termination without vacancies but instead with a Jahn-Teller distortion [30] of the surface atoms causing a wavelike structure along the $[1\ 1\ 0]$ direction, and hence the observed $(\sqrt{2} \times \sqrt{2})\text{R}45^\circ$ reconstruction [31]. Further DFT calculations performed by Yu et al. showed that the Jahn-Teller distorted B-layer termination had a similar energy to a proposed model with iron dimers in an A-layer surface [32], again confirming the sensitivity to preparation conditions. Indeed, Parkinson et al. showed that within one sputter/anneal cycle, both the B-termination and a metastable A-termination can be reproducibly prepared on a single crystal sample [33]. Bliem et al., from the same research group, later used a combination of STM, intensity-voltage LEED (I/V-LEED), and DFT to resolve the structure of the B-terminated surface as shown in Figure 1.4(b) [23]. They found that the surface was stabilised through an ordered array of subsurface cation vacancies (SCVs) due to the tendency of iron oxides to redistribute cations within the crystal lattice in response to reducing or oxidising environments.

A commonly used substrate for $\text{Fe}_3\text{O}_4(001)$ film growth is $\text{MgO}(001)$ due to the low lattice mismatch, however problems were initially encountered with Mg diffusion into the film during annealing procedures. Spiridis et al. found that the insertion of an Fe buffer layer not only prevented the migration of Mg atoms into the Fe_3O_4 film, but also led to a dimer-terminated surface [24, 34]. Their model for this dimer termination is shown in Figure 1.4(c). In addition, Novotny et al. found that a dimer termination could be produced via depositing Fe on a B-terminated surface followed by annealing [35]. As both the SCV B-layer and the dimer surface terminations exhibit the $(\sqrt{2} \times \sqrt{2})\text{R}45^\circ$ reconstruction, they are difficult to distinguish without an imaging technique.

1.4 Iron sulfides

Iron sulfides are abundantly found within the earth’s crust and play a key role in many biogeochemical and industrial processes [36, 37]. They constitute a diverse group of solids with a range of stoichiometries and are found in a variety of environments, having a key role to play in the earth’s sulfur cycle and the evolution of the earth’s surface environment [38]. Iron sulfides also have an important role to play in industrial processes, for example in froth flotation: an industrial process that selectively separates sulfides from valuable metals such as gold. This process requires the modification of, and wetting of adsorbants on, the sulfide surface, and is an industry worth \$100 million each year [37, 39]. Some properties of various iron sulfides are given in Table 1.1.

An area of great interest is the catalytic activity of iron sulfides. It has been suggested that iron sulfides facilitate chemistry within active hydrothermal vents, and there are iron-sulfur reaction centres in ferredoxins. These point to potential applications of iron sulfides as industrial catalysts. Indeed, it has been shown that under certain conditions pyrrhotite (Fe_{1-x}S) slurries facilitate Fischer-Tropsch chemistry [41, 42] and other iron sulfides catalyse N_2 conversion to ammonia [43]. In addition, due to their role in catalysing various reactions and their ubiquitousness in the earth’s crust, particularly in the early earth, origin-of-life theories propose iron-sulfides as key catalysts in the formation of the earliest metabolic organisms. These theories are known as the iron-sulfur world hypothesis by Wächtershäuser [44–48] and the iron-sulfur membrane hypothesis by Russell and Hall [49–52].

In order to better understand the reactivity of the iron sulfides, a surface science approach can be taken as mentioned in Section 1.1. However, although iron sulfide minerals are common in the earth’s crust, it remains difficult to obtain pure single-crystalline samples for analysis. The most studied of the iron sulfides to date is pyrite (FeS_2), with surface science studies mainly focussing on the (001) surface, and has been summarised in detail in a report by Murphy and Strongin [39]. The reason for this focus is the large contribution of pyrite to chemistry in diverse marine and terrestrial settings, leading to potential solutions to many problems in the environment, in technology, and in human health issues.

Table 1.1: Table showing various iron sulfides and their properties, taken from Rickard [40].

material	composition	structure	properties	natural abundance
mackinawite	FeS	tetragonal $P4/nmm$	Commonly nanoparticulate, metastable material which is the major constituent of the FeS precipitated from aqueous solutions	widespread mineral in low-temperature aqueous environments
cubic FeS	FeS	cubic $F\bar{4}3m$	highly unstable phase formed before mackinawite	not found naturally
troilite	FeS	hexagonal $P\bar{6}2c$	stoichiometric end member of the Fe_{1-x}S group	mainly found in meteorites
pyrrhotite	Fe_{1-x}S	monoclinic, for example, $A2/a$; hexagonal $P6/mmc$	nonstoichiometric stable group, where $x > 0.2$; monoclinic form is approximately Fe_7S_8 ; hexagonal form is approximately Fe_9S_{11}	most abundant iron sulfides in the Earth and solar system; rare in marine systems
smythite	Fe_9S_{11}	hexagonal $R3m$	metastable phase related to the Fe_{1-x}S group	rare mineral, mainly found in hydrothermal systems usually associated with carbonates
greigite	Fe_3S_4	cubic $Fd\bar{3}m$	metastable Fe(II) Fe(III) sulfide: the thiospinel of iron	fairly widespread mineral particularly associated with fresh water systems
pyrite	FeS_2	cubic $Pa\bar{3}$	stable iron(II) disulfide known as “fool’s gold”	the most abundant mineral on the Earth’s surface
marcasite	FeS_2	orthorhombic $Pnnm$	metastable iron(II) disulfide	common mineral in hydrothermal systems and in sedimentary rocks

In recent years, other iron sulfides have generated more research interest. For example, greigite (Fe_3S_4), which was only discovered in 1964 [53], shares a common cubane Fe_4S_4 structure with ferredoxins [54], and has been shown to be a promising material for CO_2 conversion [55, 56], leading to increased study of this material. Furthermore, greigite, which is found in the chimney cavities of hydrothermal vents [57], is believed to have catalysed CO_2 reduction reactions leading to primitive reaction pathways similar to those found in contemporary enzymes [58–60]. Despite these promising reaction mechanisms, progress is restricted because greigite only occurs in micro- or nanoparticulate form in nature, and to date no well ordered single-crystalline surfaces have been prepared for analysis.

While pyrrhotite is perhaps the most abundant iron sulfide on earth, and in the universe, much of its surface properties remain unknown or uncharacterised [61]. In fact, there is still great uncertainty even of the bulk structure of its many forms [62]. The pyrrhotites exhibit a structure based on the NiAs structure, with an ordered network of Fe vacancies. This can cause distortion to the lattice, making it monoclinic, or it can remain as hexagonal - usually at higher temperatures [36, 62, 63]. The end member of this group, troilite (FeS), was first discovered in a meteorite by Domenico Trioli in 1766 [64].

A goal of this thesis is the preparation of well-ordered iron sulfide surfaces to facilitate the use of surface science tools and techniques in order to gain insight and understanding of chemical reactions that may be catalysed. To date no thin film preparation of a single-crystalline iron sulfide except pyrite [65] has been reported in literature.

1.5 Thesis organisation

In Chapter 2, the main experimental techniques used throughout this thesis will be presented, and in Chapter 3 the theoretical background for complementary calculations will be described. In Chapter 4, the preparation of thin films of $\text{Fe}_3\text{O}_4(001)$ will be detailed, including methods of tuning the surface termination by varying the thickness of an intermediate buffer layer. Chapter 5 will present the growth for well-ordered iron sulfide thin films, with Chapter 6 showing progress toward characterising the surface structure of this sulfide. Fi-

nally, Chapter 7 will briefly summarise the findings of this thesis and potential future directions of research.

Chapter 2

Experimental Methods

The main experimental techniques used within this thesis to investigate the properties of samples are x-ray photoelectron spectroscopy (XPS), scanning tunnelling microscopy (STM), and low energy electron diffraction (LEED). This chapter describes their theoretical background and the requisite equipment.

2.1 X-ray photoelectron spectroscopy

In this thesis, x-ray photoelectron spectroscopy (XPS) is used for the analysis of the surface composition of iron sulfide samples. This technique uses the photoelectric effect, whereby a sample ejects electrons when irradiated with photons of an energy above a threshold. The interaction between one of these photons and a bound electron may result in absorption. In this case, the electron will be ejected with a kinetic energy that is linearly related to the threshold (binding) energy of the electron within the atom. This binding energy is dependent on the atomic element and its local bonding environment. The following equation relates the kinetic energy of an ejected electron, E_{kin} , to the energy of the incoming photon, $h\nu$, the binding energy of the electron, E_B , and the work function of the sample, ϕ_s , i.e. the minimum energy energy required to remove an electron from the surface of the material:

$$E_B = h\nu - E_{kin} - \phi_s. \quad (2.1)$$

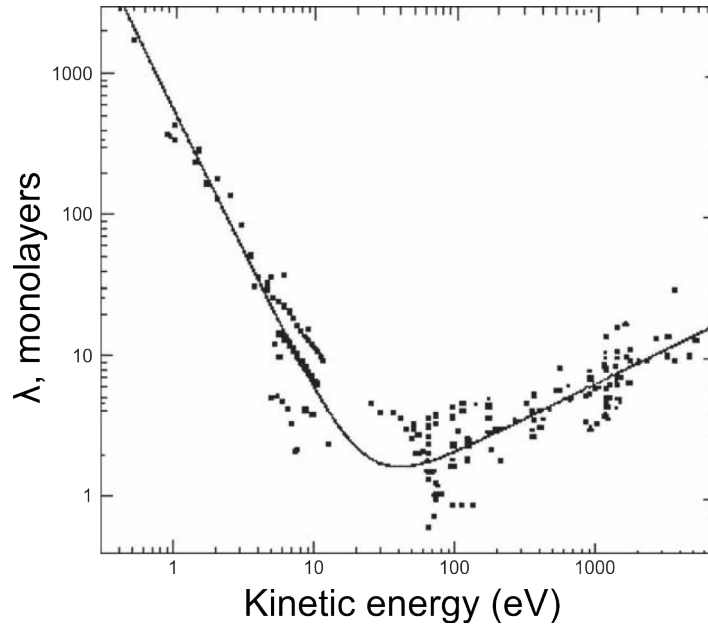


Figure 2.1: Universal curve for the dependence of attenuation length, λ , on the electron kinetic energy for various elements. X-rays with an energy of ~ 1 keV are typically used in XPS. From the work of Seah and Dench [66].

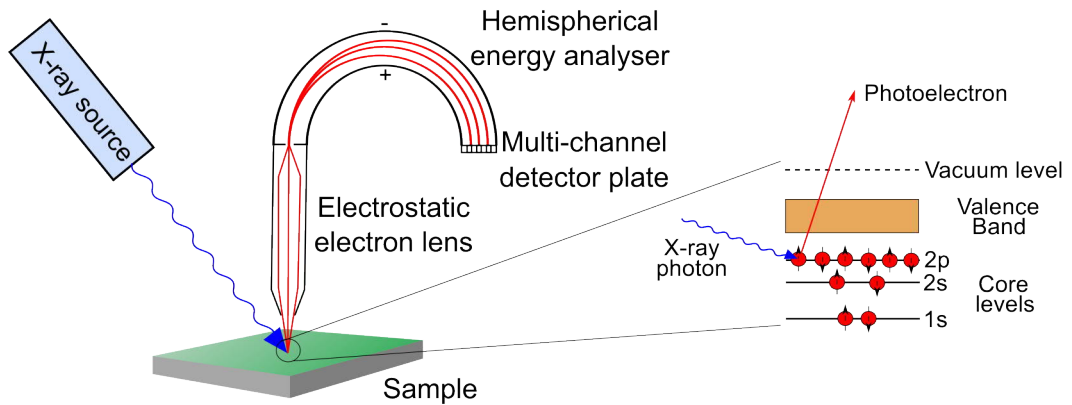


Figure 2.2: Simplified schematic of a typical XPS experimental setup and the core level photoelectron emission process. Photons from the x-ray source interact with electrons in the core levels and valence band of the sample. The energy from the photons is transferred to the electrons which are ejected into the vacuum. The lenses focus these electrons into the analyser, which selects electrons of specific energies to be counted by the detector.

X-rays can penetrate a solid sample to depths greater than 1000 nm, however, due to inelastic scattering, the electrons ejected due to x-ray photons at energies typical for XPS, around 1 keV, travel only relatively short distances within a sample. The inelastic mean free path (IMFP) of an electron can be defined as the average distance that an electron of a given energy will travel between inelastic scattering events within a medium. Figure 2.1 shows a plot of empirical values for the electron attenuation length, $\lambda = 3 \times \text{IMFP}$, versus electron kinetic energy through various materials, fitted with what is known as the Universal Curve. In XPS, the IMFP is usually between 1-4 nm, making XPS a surface sensitive technique. XPS is usually performed in UHV conditions due to the low electron IMFP at atmospheric pressures.

A schematic of a typical XPS experimental setup is shown in Figure 2.2. The sample is irradiated with x-rays, and the ejected electrons are focused into a hemispherical energy analyser by lenses. A potential is applied to the inner and outer walls of the analyser such that electrons of a specific kinetic energy will follow a semi-circular trajectory onto a multi-channel detector plate. Electrons with a higher (lower) kinetic energy than selected, via choosing the potential across the analyser, will collide with the outer (inner) walls. The electrons that reach the multi-channel detector plate are counted, and by sweeping a retardation voltage on the lenses, a spectrum of kinetic energies can be obtained. Equation (2.1) can be used to convert the spectrum to a binding energy scale.

2.1.1 Features of an XPS spectrum

Core level peaks

In a typical XPS spectrum, as shown in Figure 2.3, a series of high intensity peaks can be observed corresponding to electrons ejected from the core levels of atoms within the sample. The spectrum of each element is unique, and the area of each peak is related to the number of atoms of a particular element within the sampled area, therefore information on the chemical composition of the surface of a sample can be obtained through analysis of the peak intensities. Conventionally, the peaks have the following labelling scheme, which shall be used within this thesis: $X\ n l_j$, where X is the atomic element, n is the principal

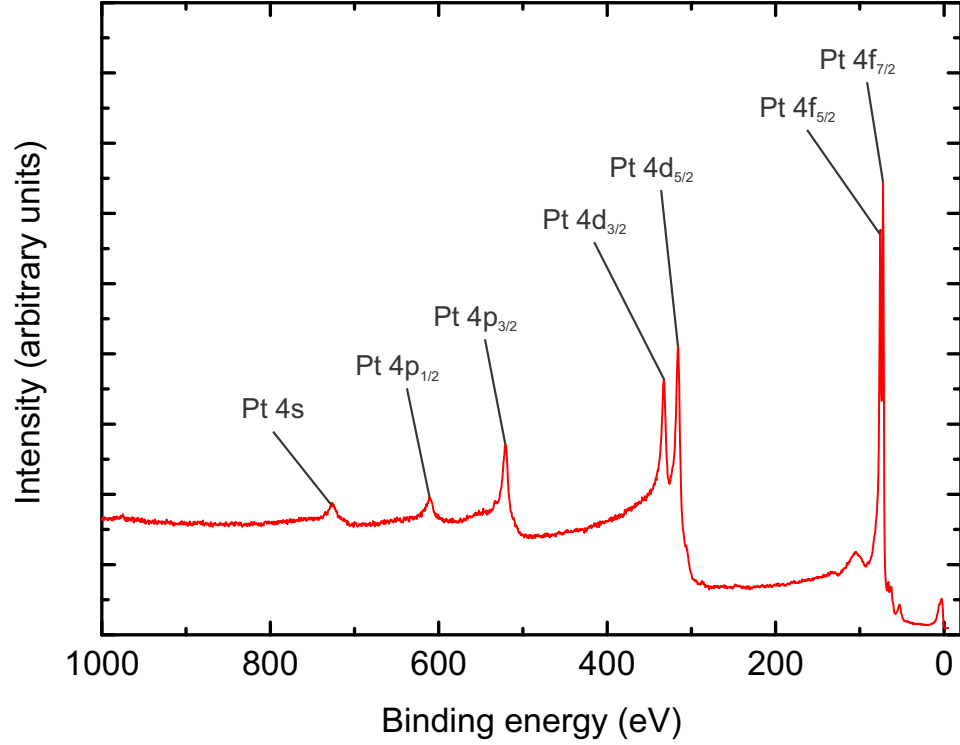


Figure 2.3: Characteristic binding energy spectrum of a clean platinum crystal in XPS. The Fermi level is defined as zero on the binding energy scale.

quantum number, l is the orbital angular momentum quantum number ($s = 0$, $p = 1$, $d = 2$, $f = 3$, etc.), and j contains information about the spin of the electron and is included where distinction is necessary. Where $l \neq 0$, $j = l \pm s$, where s is the spin of the electron. A magnetic interaction between the orbital angular momentum and the spin of the electron occurs, leading to a splitting of a degenerate state into two components with offset energy. This initial state effect, called spin-orbit splitting, results in a doublet peak in the XPS spectrum with an intensity ratio dependent on the degeneracy of each spin state, $2j + 1$.

Another source of splitting of core level peaks in XPS spectra is the coupling of a remaining unpaired electron with unpaired electrons in the valence levels in the final state of the atom. This results in an ion with several possible final state configurations of unpaired electron couplings with differing energies, producing a core level peak split into several components. This effect

is called multiplet splitting.

There are several contributors to the width of a core level peak. The principal contributions are due to the lifetime of the core hole, the spectral width of the photon source radiation, the analyser resolution, multiplet splitting, Franck-Condon broadening, etc. The resulting peak is a convolution of these factors, and is usually approximated using a mixture of a Gaussian function and a Lorentzian function. In this thesis, peak fitting was performed using the CasaXPS data processing software [67]. This software uses a least squares fit for optimisation.

Chemical shifts

The observed binding energy of a core level peak is simply the orbital energy of the ejected photoelectron, ϵ_k , minus the relaxation energy of the remaining electrons on the atom and of the surrounding atoms, $E_r(k)$:

$$E_B = -\epsilon_k - E_r(k). \quad (2.2)$$

The orbital energy ϵ_k can be calculated using Koopman's Theorem with the assumption that the orbitals of the ion following photoemission are identical to those of the initial state of the atom [68]. This does not take into account electron correlation and the effect of relativistic energies, however they are typically small enough to be ignored [69]. If the initial state of the atom is changed, for example by chemical bonds with other atoms, the observed binding energy of the electrons in that atom will also change.

A change in the binding energy of an electron due to chemical bonds is called the chemical shift, ΔE_B . In most cases, ΔE_B can be adequately interpreted solely in terms of initial state effects, i.e.

$$\Delta E_B = -\Delta\epsilon_k. \quad (2.3)$$

Siegbahn and colleagues give several examples of this correlation [70], though caution must be used when attributing chemical shifts solely to initial state effects. It cannot always be assumed that final state effects such as relaxation have a straightforward relationship with changes in the chemical environment,

and this can have an impact on the measured binding energy. In principle, however, it is possible to ascertain the bonding environments of the elements present in the spectra through analysis of the binding energies of the core level peaks.

Valence band

The region of an XPS spectrum with kinetic energy closest to the energy of the incoming photons, i.e. with binding energy close to zero, is known as the valence band region, as it corresponds to electrons excited out of the valence band of a material. The intensity spectrum in this region is the density of states (DOS) integrated across the Brillouin zone and broadened (typically with a Gaussian function). For metals, a Fermi step function, broadened due to thermal effects, approximately describes the intensity across the Fermi level and can be used for calibration of the binding energy scale. For semiconductors, on the other hand, the presence of a band gap means that there is no intensity between the valence band maximum (VBM) and the Fermi level.

Plasmons

Photoelectrons emitted from the core levels of an atom can experience losses in kinetic energy due to interactions with collective vibrations of the free electrons within the material, both in the bulk and at the surface. This manifests itself either as a series of evenly spaced, small peaks, or as an asymmetric broadening on the high binding energy side of a core level peak. There are two types of plasmonic interactions: intrinsic and extrinsic. Intrinsic plasmons are the result of a screening response to the sudden creation of a core hole in the atom, whereas extrinsic plasmons are excited as the photoelectron propagates through the solid. The two types of plasmons are indistinguishable. This effect is most pronounced in metals, due to their high free electron concentrations.

Auger peaks

The Auger emission process is a relaxation due to the creation of an ion with an inner shell vacancy following the ejection of a photoelectron. An electron from a higher energy level may fall into this vacancy, accompanied by a release

of energy. Though this energy is usually released in the form of an emitted photon, the energy can also be transferred to another electron, resulting in its ejection from the atom. This Auger electron has a kinetic energy that corresponds to the difference in energy levels of the initial electronic transition minus the ionisation energy for the electron shell that the Auger electron was emitted from. Hence, the kinetic energy of Auger electrons is independent of the photon energy of the incoming x-rays.

Satellites

There are two additional processes that can produce satellite peaks. These are caused by the sudden change in the effective charge due to the loss of shielding electrons when a core electron is removed by photoionisation. Shake-up satellites are the result of the interaction of an outgoing photoelectron interacting with a valence electron and exciting it to a higher energy level. The loss in kinetic energy of the photoelectron produces peaks on the higher binding energy side of the core level peak, corresponding to the discrete energy levels required to excite the valence electron. Shake-off satellites, similarly, are as a result of the interaction of the photoelectron with a valence electron, however in this case the valence electron is given enough energy to be ejected from the atom completely. This results in additional broad structures in the spectrum, and contribution to the inelastic background.

An additional source of satellite features is present when taking XPS measurements using a non-monochromated x-ray source. The x-rays from the source anode have a range of energies that are characteristic of that material. Typically, an anode material is chosen because of a dominant, strong resonance in the x-ray spectrum. A monochromator reduces the distribution of the photon energies, therefore improving resolution, and also removes x-rays emitted from minor resonance lines of the anode. These x-rays with differing photon energies produce satellite peaks with energy offset from the main peak.

Background

As can be observed in Figure 2.3, a step-like background is present in XPS spectra. Inelastic scattering of photoelectrons decreases their kinetic energy

and results in a “tail” on the high-binding energy side of the peaks. This background is normally subtracted for the purpose of peak-fitting, with the Shirley model for XPS backgrounds used throughout this thesis [71].

2.1.2 Quantification from XPS

As mentioned in Section 2.1.1, the area of a core level peak is dependent on the quantity of atoms of a particular element in a particular configuration within the sampled area. The equation used for determining these quantities is

$$I_{ij} = K T(E_{kin}) L_{ij}(\gamma) \sigma_{ij} \int n_i(z) e^{-z/\lambda(E_{kin}) \cos \theta} dz. \quad (2.4)$$

Here, I_{ij} is the area of peak j from element i , K is an experimental constant, $T(E_{kin})$ is the transmission function of the analyser, $L_{ij}(\gamma)$ is the angular asymmetry factor for orbital j of element i , σ_{ij} is the photoionisation cross-section of peak j from element i , $n_i(z)$ is the concentration of element i at a distance z below the surface, $\lambda(E_{kin})$ is the IMFP length, and θ is the angle of emission of the photoelectrons measured with respect to the surface normal.

The instrumental constant, K , contains parameters such as x-ray flux, sampling area, and the acceptance angle of the analyser, all of which can be assumed to be constant over the time period required for acquisition of XPS spectra. The transmission function consists of information regarding the efficiency of the collection lenses, analyser, and detector of the XPS system. The dependence of this function on the kinetic energy of the measured electrons is a result of their retardation as they pass through the lens system [72].

The angular asymmetry factor, $L_{ij}(\gamma)$, takes into account differences between different types of orbital, with a dependence on the angle γ between the incident x-rays and emitted photoelectrons. The probability of an electron from orbital j of element i being created by the incident x-ray is called the photoionisation cross-section, σ_{ij} . The values for σ_{ij} used throughout this thesis are taken from [73].

The IMFP, $\lambda(E_{kin})$, depends on both the kinetic energy of the electron and the material that it is travelling through. The equations describing have been developed by Seah and Dench [66], and values for the IMFP used in this thesis have been calculated using the QUASES software utilising the Tanuma,

Powell, and Penn algorithm [74]. The $\cos \theta$ term is to account for changes in the path length for electrons to leave the sample from a depth z as the angle, θ , between the (assumed flat) sample surface and analyser lens is varied. As changing θ away from 0° increases the path length for photoelectrons from a particular depth, fewer originating from greater depth contribute to the spectra as θ increases, effectively increasing the surface sensitivity of the technique. Information about the distribution of atoms as a function of depth can be gathered by taking advantage of this and making measurements at various values of θ .

Usually, elemental percentages or ratios are required, rather than absolute amounts, meaning that determining the absolute values of all of the quantities in Equation (2.4) is not necessary, as many of the quantities cancel out if values are computed. For spectra taken at a constant angle θ , the concentration A_i of an element i in a sample of uniform stoichiometry is given by

$$A_i = \frac{I_{ij}/T(E_{kin}) L_{ij} \sigma_{ij} \lambda(E_{kin})}{\sum_{k=1}^n I_{kj}/T(E_{kin}) L_{kj} \sigma_{kj} \lambda(E_{kin})}. \quad (2.5)$$

This equation can further be simplified by using peaks from electrons of similar kinetic energy for analysis. The differences in $T(E_{kin})$ and $\lambda(E_{kin})$ will become small and the terms will cancel out, giving

$$A_i = \frac{I_{ij}/L_{ij} \sigma_{ij}}{\sum_{k=1}^n I_{kj}/L_{kj} \sigma_{kj}}. \quad (2.6)$$

2.1.3 Calibration

As shown in Figure 2.4, placing a conducting sample in electrical contact with the spectrometer causes the Fermi level of both the sample and spectrometer to be aligned with each other and positioned at the highest occupied energy level. Equation (2.1) then becomes

$$E_B^F = h\nu - E_{kin} - \phi_{sp}, \quad (2.7)$$

where E_B^F is E_B referenced to the Fermi level E_F , and ϕ_{sp} is the work function of the spectrometer. Therefore it is not necessary to know the work function of each sample analysed by XPS in order to know E_B^F . For spectra presented

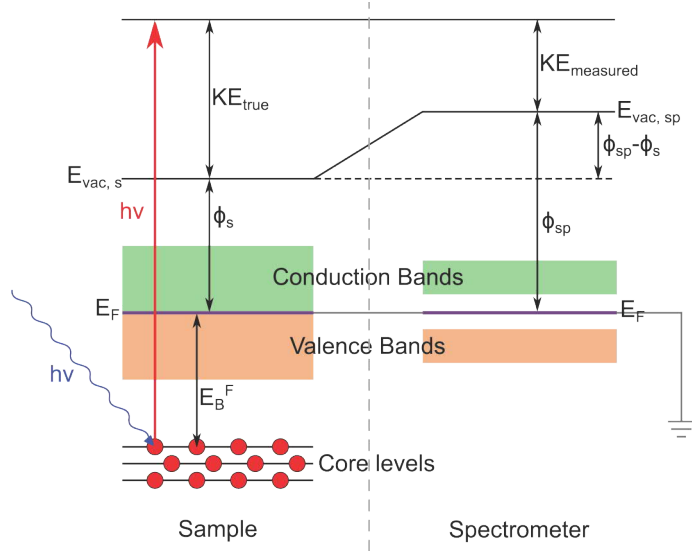


Figure 2.4: The energy level diagram for an electrically conducting sample that is grounded to the spectrometer. The Fermi levels of the sample and spectrometer are aligned ($E_f^s = E_f^{sp}$). The measured value of E_B is therefore independent of the sample work function, ϕ_s , but is dependent on the spectrometer work function, ϕ_{sp} .

in this thesis, the position of the Fermi edge for a clean gold sample was used to determine the work function of the spectrometer.

2.2 Scanning tunnelling microscopy

In this thesis, scanning tunnelling microscopy (STM) is used for the characterisation of the surface structure of well-ordered iron oxide and iron sulfide surfaces. STM was developed in the early 1980s by Gerd Binnig and Heinrich Rohrer [75], taking advantage of the concept of quantum tunnelling. By providing an atomic scale topographical map of electron densities at the surface, different surface structures can be observed and analysed.

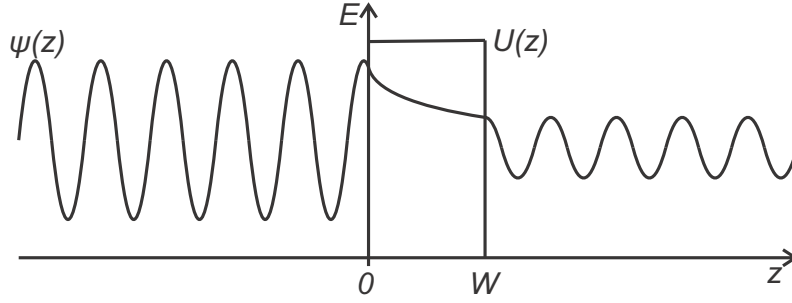


Figure 2.5: The wavefunction of an electron, $\psi(z)$, while moving under constant potential in three regions.

2.2.1 Principle of operation

The time-independent Schrödinger equation for an electron describes its wavefunction $\psi(z)$ while moving within a potential $U(z)$. In one dimension, this is

$$-\frac{\hbar^2}{2m} \frac{d^2\psi(z)}{dz^2} + U(z)\psi(z) = E\psi(z), \quad (2.8)$$

where \hbar is the reduced Planck's constant, m is the mass of the electron, E is its energy, and z is its position.

The wavefunction within three regimes will be considered, as shown in Figure 2.5, either side of and within a barrier of width W . The solution of Equation (2.8) is a travelling wave of the form

$$\psi(z) = A(z)e^{ikz}, \text{ where } k = \frac{\sqrt{2m(E - U(z))}}{\hbar} \quad (2.9)$$

and A is the amplitude of the wave. In the region $0 < z < W$, the potential $U(z) > E$, giving imaginary values for k . Assuming a constant potential U in this region, Equation (2.9) becomes

$$\psi(z) = Ae^{-\kappa z}, \text{ where } \kappa = \frac{\sqrt{2m(U - E)}}{\hbar} \quad (2.10)$$

giving an exponential decay of the wavefunction as it propagates through the barrier. The probability of finding the electron behind the barrier (i.e. at

$z \geq W$) is proportional to the wavefunction squared

$$P \propto |\psi(z)|^2 = |\psi(0)|^2 e^{-2\kappa W}. \quad (2.11)$$

Considering a metallic tip near a surface, the potential of the barrier can be approximated to the average of the work function of the tip and the sample, $U = \phi = (\phi_{tip} + \phi_{sample})/2$. When the tip and the sample are at the same potential, there is no net current flow; the Fermi levels are aligned and there are no empty states of equal energy available for tunnelling into. In STM, a small bias voltage, V , is applied, conventionally to the sample, in order to produce a current, I . Assuming a negative bias applied to the sample, electron states in the sample within $e \cdot V$ of the Fermi level, E_F , can tunnel into states on the other side of the barrier within the tip. This current is proportional to the number of electrons in the sample in this energy range.

Recognising that the sum of the electrons within a small interval can be written as the local density of states of electrons at a point z and energy E , $\rho_s(z, E)$, and that $|\psi(0)|^2$ is a constant,

$$I \propto V \rho_s(0, E_F) e^{-2\kappa W}. \quad (2.12)$$

Using a typical barrier height of 4 eV gives $\kappa \approx 1.025 \text{ \AA}^{-1}$, therefore we can see from Equation (2.12) that a 1 Å increase in barrier width W causes a near-tenfold decrease in current. For this reason, using a tip that has been sharpened such that it has one atom at its end results in nearly all of the current passing through this single atom, and accounts for the extreme sensitivity of the technique to changes in height and its lateral resolution.

2.2.2 Experimental set-up

The required components for an STM experiment, as shown schematically in Figure 2.6, include an atomically sharp tip, a piezoelectric scanner to raster the tip over the sample, feedback electronics, and a computer system to control the tip position, acquire data, and to convert data into images. Experiments are typically performed with vibration isolation for stable operation.

To obtain images, a bias is applied between the tip and sample, and

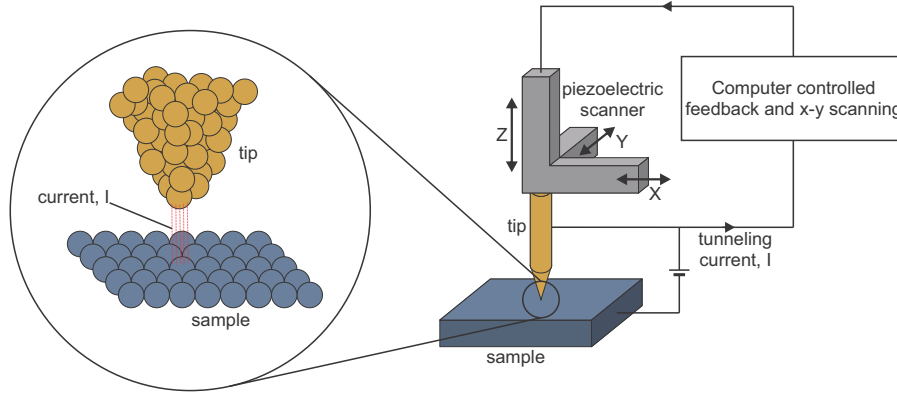


Figure 2.6: Schematic representation of a typical STM experimental setup. The apparatus is isolated from vibrations.

once the tip has been brought near enough to the sample that a tunnelling current can be detected, the computer controls voltages applied to the x-y piezoelectric crystals in order to scan an area of the sample surface. The deformation of the piezoelectric crystals of the scanning apparatus allows sub-nanometer precision in positioning of the tip. The measured tunnelling current is strongly dependent on the distance between the sample and tip, as explained in Section 2.2.1. As the relationship between tip-sample distance and current is exponential, it is usually preferred that a feedback loop is used to keep the tunnelling current constant, thus keeping the tip at a constant height above the surface. The tip height at each x-y position enables a topographical map of the surface to be constructed corresponding to the local density of electronic states.

2.2.3 Image processing

The topographical maps of the surface using STM typically contain mechanical noise from the environment and artefacts introduced by tip instability. To remove these artefacts, images are processed using a variety of techniques. Typically, plane subtraction and flattening are used as a minimum for clarity in the images. In addition, images can be smoothed, filtered using a 2D fast Fourier transform (FFT), or corrected for thermal drift. In this thesis, plane subtraction and flattening are applied to all images. Images in Chapter 6 are

filtered via 2D FFT in order to remove the effect of background electronic oscillatory noise.

2.3 Low energy electron diffraction

Throughout this thesis, low energy electron diffraction (LEED) is used for the characterisation of the crystal structure of surfaces. Electrons are ideal for studying surfaces through diffraction experiments for two main reasons. Firstly, the de Broglie wavelength of electrons is given by

$$\lambda = \frac{h}{\sqrt{2mE}}, \quad (2.13)$$

where h is Planck's constant, and m and E are the mass and energy of the electron respectively. At energies typical for LEED experiments (30-200 eV), this equates to a wavelength of $\sim 1\text{-}2 \text{ \AA}$, which, being of the order or less than the interatomic distances, results in strong diffraction, allowing the atomic structure of the material to be probed. Secondly, the IMFP of electrons at these energies is very short (see Figure 2.1), thereby giving information from only the topmost atomic layers.

2.3.1 Diffraction conditions

Electrons are scattered through interactions with atoms within the sample. In the kinematic approximation of LEED, constructive interference between scattered electrons occurs when the Bragg condition is met. The Bragg condition for diffraction between layers is

$$n\lambda = 2d \sin\theta, \quad (2.14)$$

where n is an integer, d is the atomic layer distance, and θ is the scattering angle. As can be seen in Figure 2.7, $2d \sin\theta$ is the path difference between electrons reflected from subsequent layers, and must equal an integer multiple of λ for constructive interference to occur.

The spatial distribution of the beams of diffracted electrons that experience constructive interference provides information about the crystal lattice,

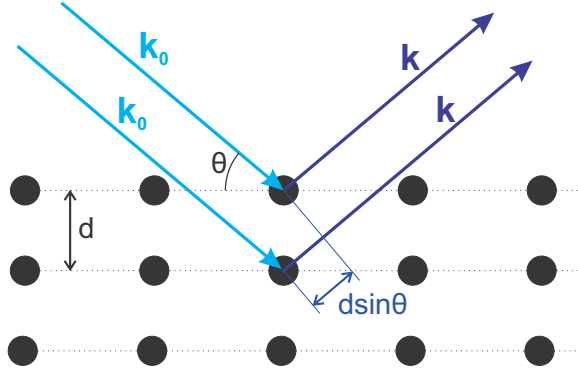


Figure 2.7: Illustration showing geometry involved in Bragg's law for diffraction between layers. The path difference of the outgoing wave vectors \mathbf{k} is equal to $2d \sin\theta$, and constructive interference occurs when this is an integer multiple of the wavelength λ .

as the resulting diffraction pattern is directly related to the crystal reciprocal lattice. The reciprocal lattice is defined by its principal vectors \mathbf{a}^* , \mathbf{b}^* , and \mathbf{c}^* in relation to the lattice vectors of the real space lattice \mathbf{a} , \mathbf{b} , and \mathbf{c} , via the following:

$$\mathbf{a}^* = 2\pi \frac{\mathbf{b} \times \mathbf{c}}{\mathbf{a} \cdot (\mathbf{b} \times \mathbf{c})}, \quad \mathbf{b}^* = 2\pi \frac{\mathbf{c} \times \mathbf{a}}{\mathbf{b} \cdot (\mathbf{c} \times \mathbf{a})}, \quad \mathbf{c}^* = 2\pi \frac{\mathbf{a} \times \mathbf{b}}{\mathbf{c} \cdot (\mathbf{a} \times \mathbf{b})}. \quad (2.15)$$

Therefore, points in the reciprocal lattice can be written as $\mathbf{G}_{\mathbf{hkl}}$, such that

$$\mathbf{G}_{\mathbf{hkl}} = h\mathbf{a}^* + k\mathbf{b}^* + l\mathbf{c}^*, \quad (2.16)$$

where h , k , and l are integers.

If \mathbf{k}_0 is the incident wave vector and \mathbf{k} is the scattered wave vector, the Laue condition for diffraction is given by

$$\mathbf{k} - \mathbf{k}_0 = \mathbf{G}_{\mathbf{hkl}}, \quad (2.17)$$

i.e. for constructive interference to occur, the scattering vector $\Delta\mathbf{k} = \mathbf{k} - \mathbf{k}_0$ must equal a reciprocal lattice vector.

The surface of the crystal represents a breaking of its 3D symmetry, with no periodicity in the direction normal to the surface. This, in combination with the surface sensitivity of LEED experiments, means that the area of the

crystal being probed can be thought of as being two-dimensional. In this case, Equation (2.17) becomes

$$\mathbf{k}^{\parallel} - \mathbf{k}_0^{\parallel} = \mathbf{G}_{\mathbf{hk}}, \quad (2.18)$$

where \mathbf{k}^{\parallel} and \mathbf{k}_0^{\parallel} are components parallel to the surface, and $\mathbf{G}_{\mathbf{hk}} = h\mathbf{a}^* + k\mathbf{b}^*$ is a vector of the 2D reciprocal lattice.

2.3.2 Ewald construction

This diffraction can be represented by the Ewald construction, the 2D version of which is shown in Figure 2.8. Firstly, the points of the reciprocal lattice are drawn. The 2D surface can be thought of as a 3D lattice having an infinite lattice spacing in the direction perpendicular to the surface, i.e. $|\mathbf{c}| \rightarrow \infty$, and therefore the length of the reciprocal lattice vector $|\mathbf{c}^*| \rightarrow 0$, leading to lattice rods extending from the surface at the points of the 2D reciprocal lattice. An incoming wavevector \mathbf{k}_0 is drawn, ending at one of the 2D reciprocal lattice points. Then, a sphere of radius $|\mathbf{k}_0| = 2\pi/\lambda$ is drawn, centred at the origin of \mathbf{k}_0 . The points where this sphere intersects the lattice rods are the points where the condition of Equation (2.18) is met, and define the scattered wave vectors \mathbf{k} for diffracted beams.

2.3.3 Experimental setup

A typical experimental setup for a LEED experiment is shown in Figure 2.9, the main components of which are an electron gun, a sample holder with the sample under investigation, and a set of four hemispherical grids and fluorescent screen for observing the scattered electrons. The experiment takes place under UHV conditions due to the low IMFP of electrons through air.

The electron gun consists of a cathode filament, a Wehnelt cylinder, an anode, and electrostatic lenses. The cathode is set to a negative potential ($-V$), and has a current passed through it, while the anode is kept at ground potential. Thus, electrons emitted by the cathode are accelerated to an energy of $e \cdot V$ towards the anode. The material used for this filament is usually a tungsten wire, but sometimes a lanthanum hexaboride (LaB_6) single crystal emitter is used because its low work function allows electrons to be easily

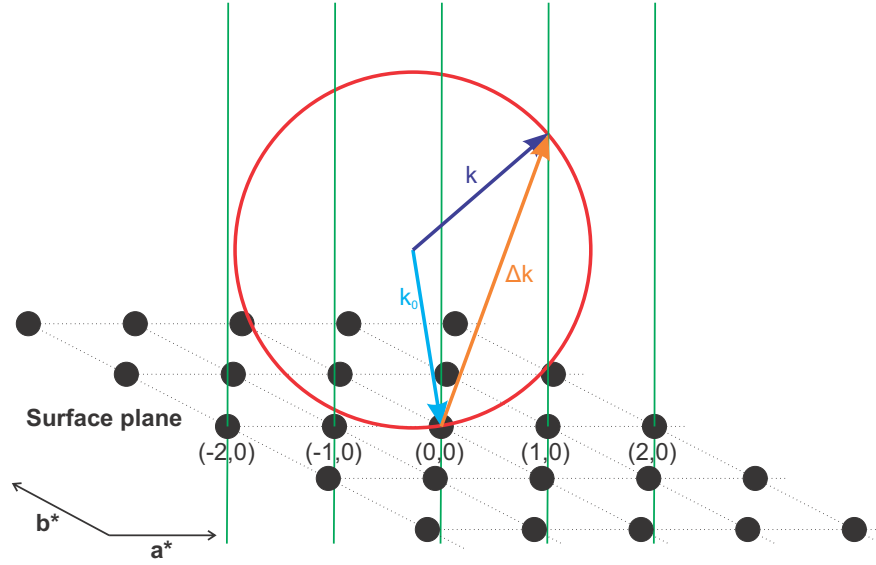


Figure 2.8: Ewald construction for diffraction from a 2D surface lattice. The incoming wave vector is \mathbf{k}_0 and terminates at a reciprocal lattice point labelled $(0,0)$. The intercepts of the lattice rods with the Ewald sphere (here drawn in 2D for clarity) determine the scattered wave vectors \mathbf{k} of the diffracted beams. One can see that the parallel component of the scattering vector $\Delta\mathbf{k} = \mathbf{k} - \mathbf{k}_0$ is equal to the 2D reciprocal lattice vector $\mathbf{G}_{\mathbf{hk}}$.

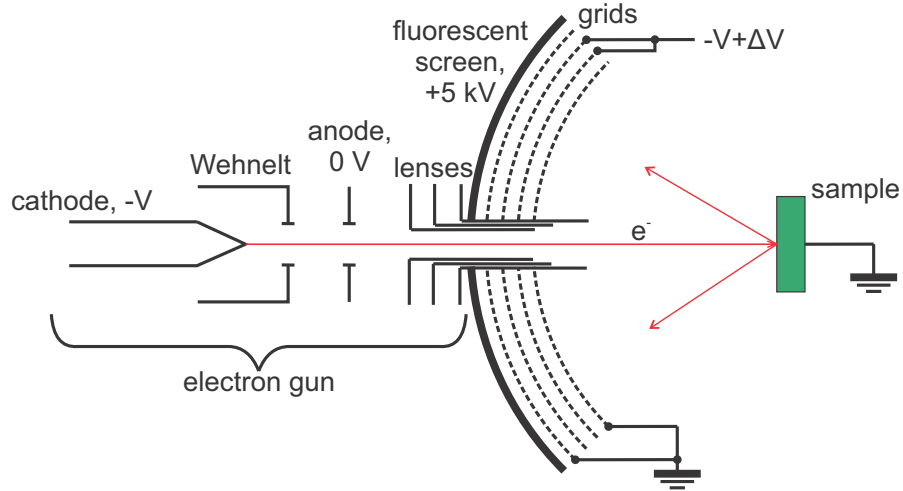


Figure 2.9: Schematic of a typical LEED experiment. Experiments take place inside a UHV chamber and the resultant diffraction pattern on the fluorescent screen is observed through a viewport or window.

extracted from it. The Wehnelt cylinder is biased relative to the cathode, and plays the roles of both controlling the size of the area of the filament from which electrons are extracted and for focussing the extracted electrons into a narrow beam. The electrons that pass through a hole at the centre of the anode are then focussed onto the sample by lenses. The sample is kept at ground potential to prevent charging.

The electrons diffracted by the sample travel through the vacuum to the grid system. The second and third grids are set to a potential slightly lower than the energy of the electrons emitted from the electron gun. This is to ensure that inelastically scattered electrons are unable to pass through the grid system due to not having the energy to overcome the potential barrier. The first and fourth grids are kept at ground potential in order to maintain a field-free space in the vacuum and to shield the high voltage of the screen respectively. The screen is set to a positive voltage of several keV in order to accelerate the inelastically diffracted electrons in the space between the fourth grid and the screen such that they cause fluorescence on impact. The diffraction pattern can then be observed on the screen. In some systems, a microchannel plate (MCP) is placed between the grids and the detection screen and acts as an electron multiplier. This allows the electron gun to be operated at a lower filament current, thus reducing the radiation damage suffered by the sample during measurement.

Considering the Ewald construction and the geometry of the LEED experiment, one can think of the diffraction pattern on the screen as being essentially a view of the surface reciprocal lattice. By increasing the energy of the incoming electrons, the Ewald sphere radius becomes larger and the diffraction spots move closer toward the spot corresponding to the specular beam. The diffraction spots are indexed as (h, k) according to Equation (2.18), with the specular spot being accepted as the $(0, 0)$ point. At normal incidence of the electron beam, this spot is located in the centre of the LEED pattern.

2.3.4 Interpretation of LEED patterns

Much information regarding the surface structure can be gained upon inspection of data from LEED experiments. Firstly, a qualitative impression of the

perfection of the surface under investigation can be obtained. Defects and deviations from a perfect periodic structure contribute to background intensity in the diffraction pattern and a broadening and weakening of diffraction spots. Hence, the more background intensity and broadening of spots is observed, the higher the level of disorder in the surface.

The geometrical positions of the LEED spots give information about the crystal lattice under investigation. In the simplest case, the surface has a 2D lattice that corresponds to a simple, bulk termination of the crystal. This would be called a 1×1 LEED pattern, and is not affected by any displacement of the surface layer perpendicular to the surface. To minimise surface energy, many surfaces undergo a reconstruction at the surface which can result in superstructures with different periodicities. These superstructures will have a 2D reciprocal lattice that results in diffraction spots appearing in the LEED pattern. From this, it is possible to identify the size of superstructure unit cells relative to the unreconstructed unit cell.

The intensity distribution profile of the LEED spots can be used to reveal information about surface imperfections, as deviations from the ideal 2D periodicity will result in disruption of the sharp spot profile. For example, a decrease in the size of domains on the surface results in a broadening of the diffraction spots.

The intensity of a spot at a particular energy is dependent on the atomic arrangement within the unit cell. In order to reveal the exact atomic configuration of the surface region, the intensity of LEED spots is measured as a function of the energy of the primary electron beam, and an iterative trial-and-error approach is used to match the intensities calculated for trial structures. This will be expanded upon in Chapter 3.

2.4 X-ray diffraction

For characterisation of the crystal structure of the iron sulfide film, x-ray diffraction (XRD) was used. XRD is a non-destructive technique that can provide detailed information about the lattice of a single crystal. X-rays are scattered through interactions with atoms within the sample, and, as in the case of LEED, Bragg's law (Equation (2.14)) describes diffraction between

layers. In this case, λ is the wavelength of the incident x-ray beam. X-ray sources are chosen such that the wavelength is less than interatomic distances, e.g. Cu $K\alpha$ radiation with a wavelength of 1.54 Å.

The interaction of x-rays with matter is much weaker than that of electrons, therefore they are able to penetrate much deeper into the material. The large IMFP of x-rays makes XRD a bulk-sensitive technique, in contrast to the surface sensitivity of LEED. The diffraction conditions are the same as those given in Section 2.3.1 for LEED in Equation (2.17), i.e. that for constructive interference to occur, the scattering vector must equal a reciprocal lattice vector.

For XRD, the Ewald construction is in 3D, in contrast to the 2D version presented in Section 2.3.2. A cross-section of this Ewald construction is shown in Figure 2.10. Because XRD is a bulk technique, breaking of the periodicity of the crystal lattice at the surface can be neglected and the reciprocal lattice is represented using points rather than the rods used in the 2D case. An incoming wavevector \mathbf{k}_0 is drawn, ending at one of the reciprocal lattice points. Then, centred at the origin of the incoming wavevector, a sphere of radius $|\mathbf{k}_0| = 2\pi/\lambda$ is drawn. The Laue condition, given in Equation (2.17), is met where the sphere intersects the reciprocal lattice. This defines the scattered wave vectors \mathbf{k} for diffracted beams.

Measurement of single crystal samples typically involves placing the sample in the x-ray beam in various orientations, and detection and counting of diffracted beams at various positions around the sample. The collection of these beams reveals the diffraction pattern, giving the reciprocal lattice points which can be used to determine the crystal structure.

The weak interaction of x-rays with matter also means that diffraction can be described accurately by assuming that x-rays are only scattered once. This is useful for solving the crystal structure of the sample, as the theoretical considerations for calculating the intensities of diffracted beams are much simpler than for LEED. The intensity of diffracted beams is proportional to the square of the structure factor of the unit cell, which depends on the distribution of electron density within the lattice. Once an electron density map has been generated, a model structure is refined by assigning atoms to the areas of electron density, and further still through varying parameters until

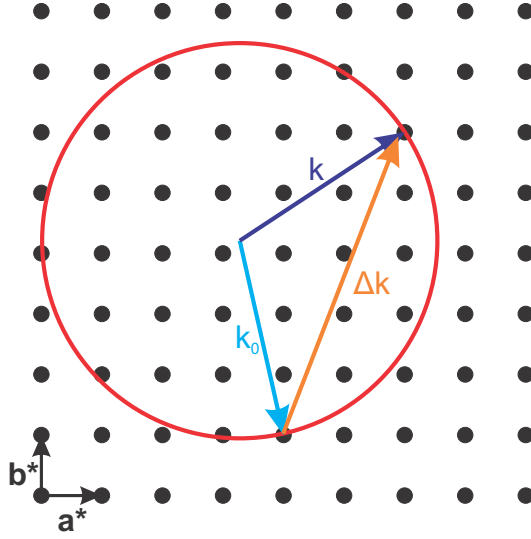


Figure 2.10: Cross section of the Ewald construction for diffraction from a 3D lattice. The incoming wave vector is \mathbf{k}_0 and terminates at a reciprocal lattice point, and the places where the Ewald sphere intersects with a reciprocal lattice point determine the scattered wave vectors \mathbf{k} of the diffracted beams.

a satisfactory agreement is reached. To find agreement between model and experiment requires the calculation of intensities from the structure factor of the model structure, F_{calc} , which are compared to those derived from the observed intensities, F_{obs} . The quality of a solution is assessed using an R-value, R , given by

$$R = \frac{\sum ||F_{obs}| - |F_{calc}||}{\sum |F_{obs}|}. \quad (2.19)$$

Chapter 3

Theoretical Methods

This chapter will outline the principles and theoretical methods behind the calculations performed in order to determine the surface structure of iron sulfide films.

3.1 I/V-LEED

As mentioned at the end of subsection 2.3.4, the intensity of a diffraction spot in a LEED pattern at a particular energy is dependent on the atomic arrangement within the unit cell. The measurement of this intensity as a function of the energy of the primary electron beam results in an intensity-voltage curve (I/V-curve). The kinetic theory of electron scattering in LEED as presented in section 2.3 is inadequate for understanding the intensity modulations in such spectra. This is because in the kinematic approximation borrowed from other techniques, such as x-ray scattering, only single scattering is taken into account, however the interaction of low energy electrons with atomic centres is many orders of magnitude greater than that of x-rays, resulting in multiple scattering effects. This has led to the development of the dynamical theory of LEED, as laid out in detail by Van Hove and Tong in the context of the SATLEED program used throughout this thesis [76], and more generally by Pendry [77]. The technique of using I/V-curves to determine the structure of the surface under investigation is called intensity-voltage LEED (I/V-LEED).

This technique proceeds via a trial-and-error approach. A set of experimental I/V-curves is measured, and a trial structure is assumed for the

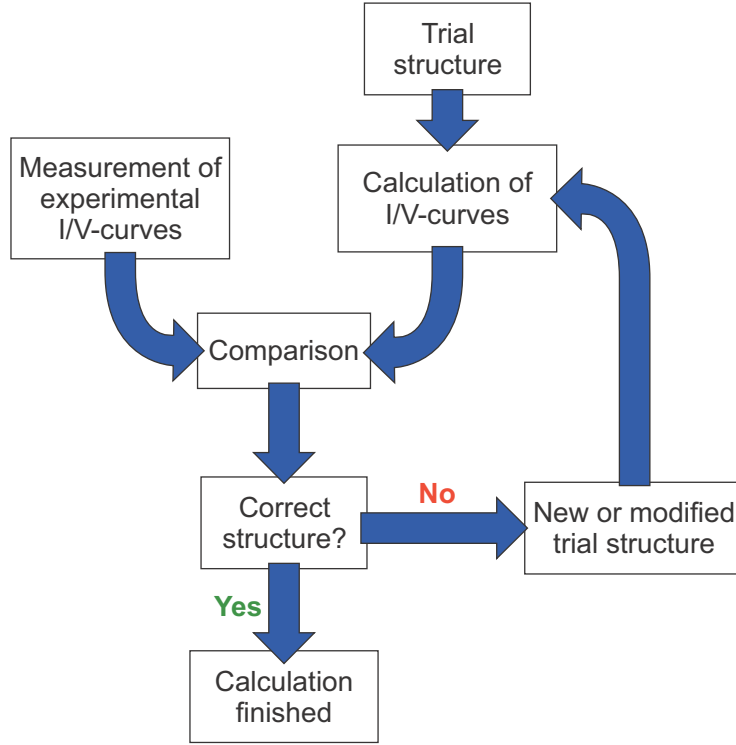


Figure 3.1: Schematic showing the logical approach to structure determination using I/V-LEED.

sample. The theoretical I/V-curves for the trial structure are calculated and compared with the experimental I/V-curves of the sample. If the curves are identical, the trial structure exactly matches the sample structure. In practice, there must always be small deviations between the measured and calculated curves due to approximations within the theory. If the I/V-curves differ, the trial structure is modified or changed, and a new set of I/V-curves are calculated. This proceeds until satisfactory convergence is reached between theory and experiment. The process is illustrated in Figure 3.1.

3.1.1 Principles

It is possible to understand the basic principles of the features observed in an I/V-LEED spectrum by considering the following. Firstly, a one-dimensional space is considered with a semi-infinite crystal composed of evenly-spaced atoms from $x = 0$ to $x = \infty$. An incoming wave e^{ikx} with wavevector k

is incident on the crystal from $x = -\infty$ and is scattered by each atom such that the scattering can be described by complex coefficients of reflection r and transmission t .

In the weak scattering limit, corresponding to kinematic theory, $|r|$ is very small and $|t|$ is approximated as 1. These approximations result in a reflection of the wave given by

$$\sum_{j=0}^{\infty} r e^{ik2aj} e^{-ikx} = \frac{r}{1 - e^{ik2a}} e^{-ikx}, \quad (3.1)$$

where a is the lattice parameter of the crystal and $r e^{ik2aj}$ represents the amplitude factor for the wave travelling to the $(j + 1)$ th atom and back. The amplitude of the reflected wave is generally small except for wavevectors that fulfil the Bragg condition $k2a = n2\pi$ (see Equation 2.14), where the amplitude is infinite, as shown in Figure 3.2(a). This infinite intensity, violating current conservation, is due to the initial approximation that $|t| = 1$. This is rectified by using an improved physical description with $|t| < 1$. With this new description, the amplitude factor must now become $r t^{2j} e^{ik2aj}$ to account for transmission twice through each intervening atom. Instead of Equation 3.1, the reflection of the wave is now given by

$$\sum_{j=0}^{\infty} r t^{2j} e^{ik2aj} e^{-ikx} = \frac{r}{1 - t^2 e^{ik2a}} e^{-ikx}. \quad (3.2)$$

It is immediately clear that, since $|t| < 1$, the maxima in amplitude of the reflected wave are no longer of infinite height, though they remain at the same wavevectors fulfilling the Bragg condition, as can be seen from Figure 3.2(b).

The above description is still incomplete with regard to current conservation, as the wave is only either reflected or transmitted at any single atom. It must be considered that for each transmission of the wave, the current lost from the initial wave goes into a reflected wave, and this in turn can be reflected. For current conservation, these multiple reflections must be calculated to infinite order to account for all of the current lost from the primary beam. This is achieved through a self-consistent treatment within Bloch wave theory. The outcome of this treatment is that the diffraction peaks are truncated, re-

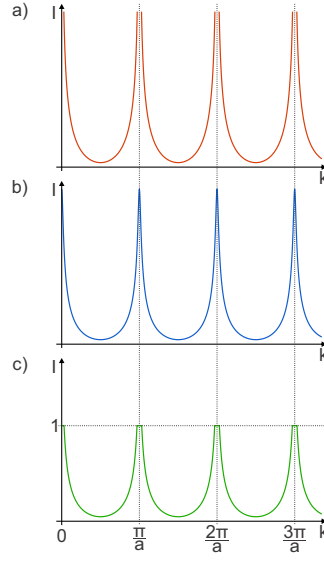


Figure 3.2: Reflected intensities of the electron wave as a function of wavenumber k as dynamical effects are introduced: (a) very small reflection coefficient and total transmission, (b) limited transmission, and (c) multiple scattering.

sulting in flat peaks with a height of 1 as shown in Figure 3.2(c). These flat peaks correspond to band gaps within the crystal, where no propagation of the electron wave may take place and therefore total reflection occurs.

Extending this analogy to three-dimensions leads to periodicities in additional dimensions and a corresponding increase in the number of beams in which elastically scattered electrons can travel. As outlined in subsection 2.3.1, the surface of a crystal has 2D periodicity, and the 2D reciprocal lattice vectors, $\mathbf{G}_{\mathbf{hk}}$, characterise the set of beams. If a is the layer spacing and \mathbf{g} is a beam which is diffracted into \mathbf{g}' by each layer, then the Bragg condition for constructive interference between layers is given by

$$k_{\perp}(\mathbf{g}) \cdot a + k_{\perp}(\mathbf{g}') \cdot a = n \cdot 2\pi, \quad (3.3)$$

where n is an integer and $k_{\perp}(\mathbf{g})$ is the component of the wavevector of \mathbf{g} perpendicular to the plane of the layers.

When multiple scattering is introduced here, it becomes apparent that the condition in Equation 3.3 is met by different scattering paths at different

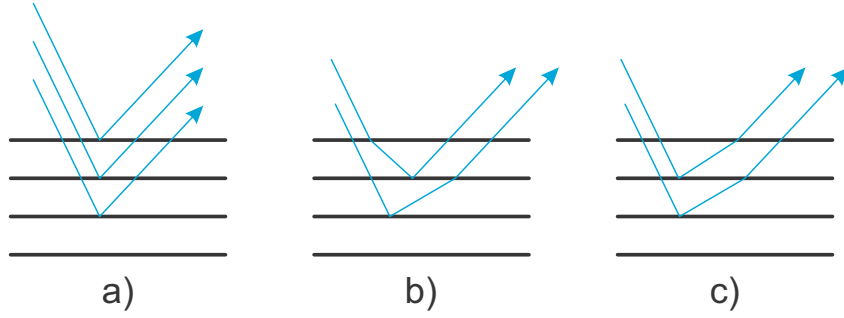


Figure 3.3: Schematic showing how different paths caused by strong multiple scattering in LEED will have different path lengths meeting the Bragg condition at different values of the wavenumber k .

wavelengths, which therefore have peaks at different energies. This is illustrated in Figure 3.3. The presence of these additional multiple-scattering peaks are partly responsible for the difficulty in trying to understand I/V-curves within the kinematic approximation.

Computation of the scattering process, though complex, may be approached through a hierarchical approach in three steps as illustrated in Figure 3.4. Firstly, scattering from a single atom is calculated. Secondly, these atoms are arranged into atomic layers, for which layer diffraction matrices can be computed. Finally, the layers, and therefore the layer diffraction matrices, are stacked to yield the total reflection matrix of the surface.

The interaction of an electron with matter is much stronger than that for x-rays, therefore the kinematic approximation is not an appropriate description. In reality, an electron is scattered by every atom along its path, and this scattering can be described by solving the Schrödinger equation. A spherical atomic potential can be assumed, despite the non-spherical symmetry of the atomic environment, because the electrons at the energies used for LEED are high enough above the Fermi energy that scattering is dominated by the nucleus and the spherically symmetric inner electron shells of the atom. A “muffin-tin” approach is used for the description of the spherical potential of the atoms, which is arranged such that the spheres of neighbouring atoms touch each other, and the areas in between have a constant inner potential, V_{0r} . This potential increases the energy of an electron entering the crystal so

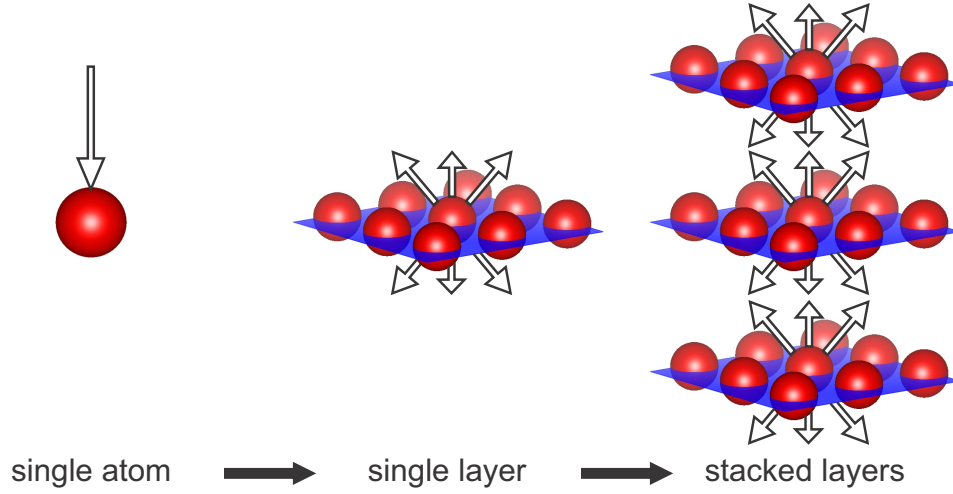


Figure 3.4: Schematic showing the heirarchy of dynamical I/V-LEED calculations.

that its total kinetic energy $E = E_i + V_{0r}$, where E_i is the initial energy of the electron.

When an electron enters the spherical potential around an atom, its energy increases. With this comes a corresponding shortening of its wavelength, as shown for a simplified case in Figure 3.5 for an electron above a square potential well. This results in a shifting of the phase relative to an electron that has not passed through the potential. These phase shifts must be accounted for in determining the energies at which the Bragg condition is met for diffraction to occur, typically resulting in the Bragg peaks moving to lower energies in comparison to the simple kinematic approximation given above. Due to the spherical symmetry of the atomic potential, these phase shifts are usually described using angular momentum l , with a cut-off at a maximum value l_{max} where the phase shifts are assumed to be negligible. Solving the Schrödinger equation results in a set of phase shifts δ_l which fully describe the multiple scattering within the atom.

Scattering within an atomic layer is then treated self-consistently, also in angular momentum space, with spherical waves outgoing from each atom expanded to neighbouring atoms within the layer. The self-consistent approach is required because electrons may be scattered back to the original atom. A matrix inversion formalism is used for this approach, the dimensions of which

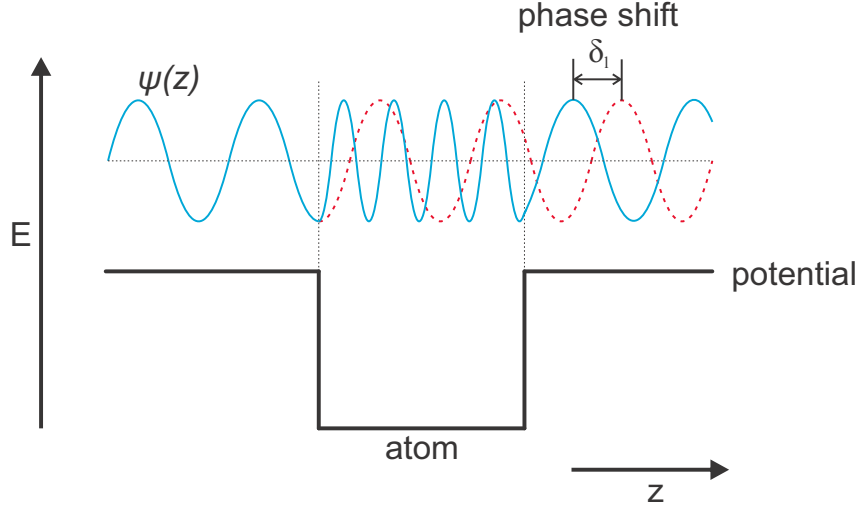


Figure 3.5: Schematic of the phase shift that occurs for an electron above a potential well. The wavelength of the electron is shortened above the well, leading to a shift of phase, δ_l , relative to if the well was not present (dashed line).

scales with l_{max}^2 .

A momentum space representation is appropriate for the total diffraction from the layer because of its translational symmetry. The atomic scattering amplitudes are summed and converted into a set of plane waves with surface parallel momenta $(\mathbf{k}_{\parallel} + \mathbf{g})$, which results in matrices of layer diffraction amplitudes $M_{gg'}^{\pm\pm}$, where the \pm signs indicate the direction of in- and outgoing plane waves.

In order to describe the full diffraction by the surface, the matrices $M_{gg'}^{\pm\pm}$ are used to stack the layers. Another matrix inversion is required here in order to self-consistently account for multiple diffraction between layers. A layer doubling scheme can be used, whereby neighbouring layers are coupled so that in each inversion step the number of layers can be doubled. Alternatively, in cases where the spacing between layers is larger than 1 Å, the fact that forward diffraction ($M_{gg'}^{++}$ or $M_{gg'}^{--}$) dominates over backward diffraction ($M_{gg'}^{+-}$ or $M_{gg'}^{-+}$) can be used in order to avoid the matrix inversion and speed up computation. This procedure is known as renormalised forward scattering (RFS) [78].

Because an electron travelling through a solid experiences loss of energy due to inelastic interactions such as phonon excitations, attenuation of

the beam must be considered. This is described by using a complex inner potential $V_0 = V_{0r} + V_{0i}$, with the imaginary part, also known as the optical potential V_{0i} , causing an attenuation of the spherical and plane waves describing the electron. This value is typically around 4-5 eV, and is slightly energy dependent ($V_{0i} \propto E^{\frac{1}{3}}$). Thermal vibrations are also included within the theory for the atomic scattering amplitudes through the use of energy-dependent Debye-Waller factors.

3.1.2 Comparing theory and experiment

Having calculated a set of I/V-curves for a structure, they must be compared with the experimental I/V-curves. For this, a quantitative measure of the similarity of the curves is necessary. The numerical value assigned to this is called a reliability factor, or R-factor. Numerous methods of calculating R-factors exist, however the most commonly used is the Pendry R-factor [79], which shall be used throughout this thesis.

As the positions of the peaks in the I/V-curves depend on the constructive and destructive interference caused by the interplay between electron wavelength and path difference, the Pendry R-factor puts an emphasis on the positions of the maxima and minima in the I/V-curves, rather than the absolute intensities. The logarithmic derivative, L , of the intensity, I , with respect to energy is used where

$$L = \frac{\partial I / \partial E}{I}. \quad (3.4)$$

Because multiple scattering can lead to zero intensity in the I/V-curves due to destructive interference, a bounded function Y is used to prevent instances of infinitely large L , where

$$Y = \frac{L}{1 + (LV_{0i})^2} \quad (3.5)$$

This also reduces the sensitivity to experimental errors in regions of low intensity.

The Pendry R-factor, R_P , is then simply defined as the mean square

deviation of the Y functions for theory ($Y_{\mathbf{g},th}$) and experiment ($Y_{\mathbf{g},ex}$)

$$R_P = \sum_{\mathbf{g}} \int (Y_{\mathbf{g},th} - Y_{\mathbf{g},ex})^2 dE \bigg/ \sum_{\mathbf{g}} \int Y_{\mathbf{g},th}^2 - Y_{\mathbf{g},ex}^2 dE. \quad (3.6)$$

The lower the R-factor, the better the agreement between theory and experiment. An R-factor of $R_P = 0$ corresponds to perfect agreement, whereas $R_P = 1$ indicates uncorrelated curves. Anticorrelated curves produce $R_P = 2$.

The variance of R_P is defined as

$$var(R_P) = R_P \sqrt{\frac{8V_{0i}}{\Delta E}}, \quad (3.7)$$

where ΔE is the total energy range of the data, and allows for the estimation of error limits for the set of parameters used for the trial structure [79].

3.1.3 Search algorithms

In order to find the correct structure, it is necessary to find the trial structure which gives the best R-factor when compared to the experimental data. While for simple unreconstructed surfaces this may be quite straightforward, as the complexity of the system increases, so does the number of trial structures required in order to effectively scan the parameter space of possible structures. To determine the best-fit structure corresponding to a minimum in the R-factor, the parameter space should be scanned in an efficient manner.

Finding the structure giving the minimum R-factor, i.e the minimum difference between the calculated and experimental I/V-curves, is essentially an optimisation problem in a D -dimensional parameter space, with D being the number of parameters describing the trial structure, such as the atomic coordinates, Debye temperatures, and inner potential. The trial structures can be represented by a vector in D -dimensional space, with the R-factor mapping this vector to a real number ($\mathbb{R}^D \rightarrow \mathbb{R}$). This mapping defines a hyper surface, with the optimal R-factor being the deepest minimum, or global minimum, of this surface.

Several considerations must be made in approaching this optimisation problem. To make the search process more feasible, the parameter space is

often greatly restricted to a much smaller subspace in the region of the expected structure. This is often done through chemical or physical intuition, for example by excluding regions representing unphysical atomic distances or through analogy with systems with a similar structure to the one under investigation, or through the guidance of results from complementary experimental techniques. Proper consideration of symmetry can also greatly reduce the dimension of the search space.

In addition, an appropriate search method must be selected. In general, the hyper surface mapped by the R-factor will have many minima, with only one global minimum corresponding to the correct structure. While in principle a simple search of every point in a densely spaced grid in the search space would yield the global minimum R-factor, in practise this is usually impractical due to the sheer computational time required to perform calculations at each point. Randomly varying parameters would find the global minimum eventually, however search algorithms are usually used and are designed such that minima in the R-factor hyper surface are attractive.

Various search algorithms exist with varying effectiveness and ranges of validity. An example of a simple optimisation algorithm is Powell’s method [80] in conjunction with Tensor LEED [81–83]. In Tensor LEED, the I/V-curves of trial structures are calculated via perturbation of a reference structure. While this method is very fast, it requires that the initial reference structure is very close to the structure with the global minimum R-factor, otherwise it will simply find a local minimum or leave its range of validity. More sophisticated algorithms employ strategies to enable the search to be performed over a much larger space and to be able to distinguish local minima from the global minimum. In this thesis, I/V-LEED is used to characterise the surface of a previously unidentified material, therefore the differential evolution (DE) algorithm of Storn and Price [84] will be the method principally used as it has been shown to have a large convergence range of relative to several other commonly used algorithms [85].

The DE algorithm is one of several global search algorithms inspired by the theory of the evolution of species in nature. In these algorithms, each trial structure is described by its genome (the parameters defining the structure) and is considered as an individual within a population of trial structures. The

R-factor then denotes the evolutionary fitness of the individual. New individuals, “offspring”, are then generated and introduced to the population, replacing an individual if it meets particular criteria, to produce a new generation of the population. This process is repeated until convergence is reached.

In the DE algorithm, the individuals are represented by vectors, and the offspring are generated as a perturbation (mutation) of the genome of individuals within the parent population. The initial population is generated randomly following a normal distribution around an individual representing an initial trial structure. A population in generation G with N individuals consists of N D -dimensional vectors $\mathbf{X}_{i,G}$, where $i = 1, 2, \dots, N$ and D is the number of fit parameters. Mutated vectors $\mathbf{M}_{i,G+1}$ for generation $(G + 1)$ are created using

$$\mathbf{M}_{i,G+1} = \mathbf{X}_{j,G} + F \cdot (\mathbf{X}_{k,G} - \mathbf{X}_{l,G}), \quad (3.8)$$

where the indices $j, k, l \in \{1, 2, \dots, N\}$ are mutually different, different to i , and randomly chosen, and $F \in (0, 2]$ is an amplification factor for the differential variation $(\mathbf{X}_{k,G} - \mathbf{X}_{l,G})$.

The genetic diversity of the mutant population is then increased by computing a set of trial vectors $\mathbf{T}_{i,G+1} = (\mathbf{T}_{1,i,G+1}, \mathbf{T}_{2,i,G+1}, \dots, \mathbf{T}_{D,i,G+1})$ mixing parameters from the mutant vectors with those in the parent generation. The parameters $\mathbf{T}_{v,i,G+1}$ ($v = 1, 2, \dots, D$) are chosen such that

$$\mathbf{T}_{v,i,G+1} = \begin{cases} \mathbf{M}_{v,i,G+1}, & \text{if } \text{random}(v) \leq C \text{ or } v = \text{rnb}(i) \\ \mathbf{X}_{v,i,G+1}, & \text{otherwise} \end{cases}. \quad (3.9)$$

Here, $\text{random}(v) \in [0, 1]$ is the v th evaluation of a random number generator, $C \in [0, 1]$ is a crossover constant chosen to control the degree to which mutated parameters are included into the trial vectors, and $\text{rnb}(i) \in \{1, 2, \dots, D\}$ is randomly chosen and guarantees the inclusion of at least one parameter from the mutated vector.

Finally, the trial vector must be evaluated for fitness to be included in generation $(G + 1)$. If the fitness of trial vector $\mathbf{T}_{i,G+1}$ is better than that of the corresponding parent vector $\mathbf{X}_{i,G+1}$, then it replaces it in the population. In this case, a lower R-factor is considered to be better fitness, leading the population to gravitate toward a minimum. The parameters F and C determine

extent of the search space and the diversity of the population respectively, and therefore control the overall performance of the algorithm. The size of the population determines how thoroughly the search space is sampled.

Chapter 4

$\text{Fe}_3\text{O}_4(001)$ Growth on $\text{Pt}(001)$

4.1 Introduction

In this chapter, the growth of thin $\text{Fe}_3\text{O}_4(001)$ films on a metallic substrate is addressed. The use of a metal support facilitates using surface science tools, in particular the use of vibrational and electron spectroscopies, in contrast to studies of films grown on insulating $\text{MgO}(001)$ substrates. It is believed that, at the time of the study, growth of $\text{Fe}_3\text{O}_4(001)$ on a metal support has been mentioned only by Fonin et al. [86] for a $\text{W}(001)$ substrate in the course of work function measurements, however, detailed surface structure characterization has not been provided. As $\text{Pt}(111)$ has successfully been used for epitaxial growth of crystalline $\text{Fe}_3\text{O}_4(111)$ films, initial considerations point to the use of $\text{Pt}(001)$ as a substrate to grow (001) -oriented films. The $\text{Pt}(001)$ surface unit cell length of 2.77 \AA leads to a lattice mismatch of only 0.9 % with $\text{Fe}_3\text{O}_4(001)$. It should be noted, however, that Ritter et al. [87] have briefly mentioned that the growth of multilayer iron oxide films on both $\text{Pt}(001)$ and $\text{Pt}(111)$ leads to (111) -exposing surfaces. In this chapter, it will be shown that well-ordered $\text{Fe}_3\text{O}_4(001)$ films can successfully be grown on $\text{Pt}(001)$ and also that the two most stable terminations can both be achieved through variation of growth parameters.

4.2 Experimental details

The experiments were carried out in a UHV chamber, with a base pressure of 2×10^{-10} mbar, equipped with STM (from Omicron) and LEED and Auger electron spectroscopy (AES) (from Specs). The surface of a Pt(001) crystal (from MaTeck) was prepared through cycles of Ar^+ -sputtering and UHV annealing until the characteristic hex-reconstruction was observed in LEED, as shown in Figure 4.1(a). Iron was deposited onto the sample using an e-beam assisted evaporator (EFM 3, Omicron). The deposition rate of $\sim 7 \text{ \AA}/\text{min}$ was calibrated by STM in the same way as in ref. [88], where it was shown that Fe atoms on Pt(001) at low coverages undergo atomic site exchange, with Fe atoms preferentially sitting in the sub-surface region and Pt islands forming at the surface.

4.3 Results and analysis

Since previous studies, using cycles of Fe deposition in UHV and oxidation, of the preparation of Fe_3O_4 films on both Pt(111) and Pt(001) resulted in (111)-oriented films [87, 89], the first approaches examined here attempted film growth by Fe deposition in an oxygen ambient (reactive deposition), followed by annealing at elevated temperatures to achieve well-ordered films.

Increasing amounts of iron, between 8 and 50 nm, deposited onto a Pt(001)-hex surface in 10^{-5} mbar of O_2 at 300 K causes LEED patterns to vanish, thus indicating a highly disordered surface. Subsequent annealing in UHV at 550 K led to the appearance of some diffuse diffraction spots. Effectively the same surface was obtained by reactive deposition with the sample held at 550 K. Further annealing to 645 K and then to 775 K, for 60 min each, considerably improves film ordering, as judged by LEED, but the resultant surfaces exhibited hexagonal symmetry Figure 4.2. Indeed, STM inspection of the annealed films revealed a relatively rough surface Figure 4.2(a), where a hexagonal lattice of protrusions with an $\sim 6 \text{ \AA}$ periodicity are observed, along with vacancy-type defects and extended areas resembling biphasic ordered structures, all well documented for highly defective $\text{Fe}_3\text{O}_4(111)$ films and crystal surfaces [90, 91]. Although precise structures were not determined here, it

is concluded that iron oxide growth directly onto the Pt(001) surface leads to the formation of 111-oriented films. It seems plausible that under these conditions the interface constitutes of an FeO(111)-like layer, as previously found for monolayer films [89, 92]. In addition, a recent study addressing the Pt/Fe₃O₄ interaction [93] showed that charge transfer from a transition metal oxide to Pt apparently maximizes the number of Pt-cation (in this case Fe) contacts at the interface, which will certainly be higher in the case of a close-packed (111) structure. If this is the case, such an FeO(111)-like interfacial layer probably drives the film growth towards (111) faces, even on Pt(001). In order to diminish this effect, in the next approach, an Fe buffer layer was employed, as first used by Spiridis et al. for a MgO(001) substrate [34].

Deposition of a 4 nm thick Fe layer onto the clean Pt(001) surface in UHV leads to a lifting of the hex-reconstruction of the Pt. The remaining (1×1) diffraction spots (see Figures 4.1(a) and 4.1(b)) could be assigned to an epitaxially grown Fe(001) layer, which has only a small mismatch with Pt(001) ($\sim 3\%$), since Auger spectra showed no Pt signal. Subsequent deposition of 4 nm of Fe at 300 K in $\sim 5 \times 10^{-6}$ mbar of O₂ resulted in a diffuse diffraction pattern (Figure 4.1(c)). However, upon prolonged annealing at 775 K, the LEED pattern gradually transforms into the one well-documented for a Fe₃O₄(001)-($\sqrt{2} \times \sqrt{2}$)R45° reconstructed surface (Figure 4.1(d)). Further annealing at 1020 K for 10 min produced even sharper diffraction spots. STM images revealed wide terraces with few screw dislocations (Figure 4.3(a)). The terraces show atomic rows in the [110] direction and anti-phase domain boundaries, both typical of the B-termination [21]. High-resolution images also revealed some vacancy-type defects and ad-species (Figures 4.3(b) and 4.3(c)).

The above preparation was fully reproducible. It should be noted that the sample temperature during iron reactive deposition should be relatively low (300 K in this case), otherwise the metallic Fe layer can, at least partly, be oxidized, and as such the situation becomes very similar to film growth without the Fe buffer layer. Indeed, reactive deposition at 550 K on top of the 4 nm-thick buffer layer led to a mixture of (001) and (111) surfaces as shown in Figure 4.4. An increase in oxygen pressure (in the range $> 10^{-5}$ mbar) sometimes caused the formation of holes within the films, and additional spots in the LEED pattern characteristic of FeO(111)/Pt(001) [89], as shown in

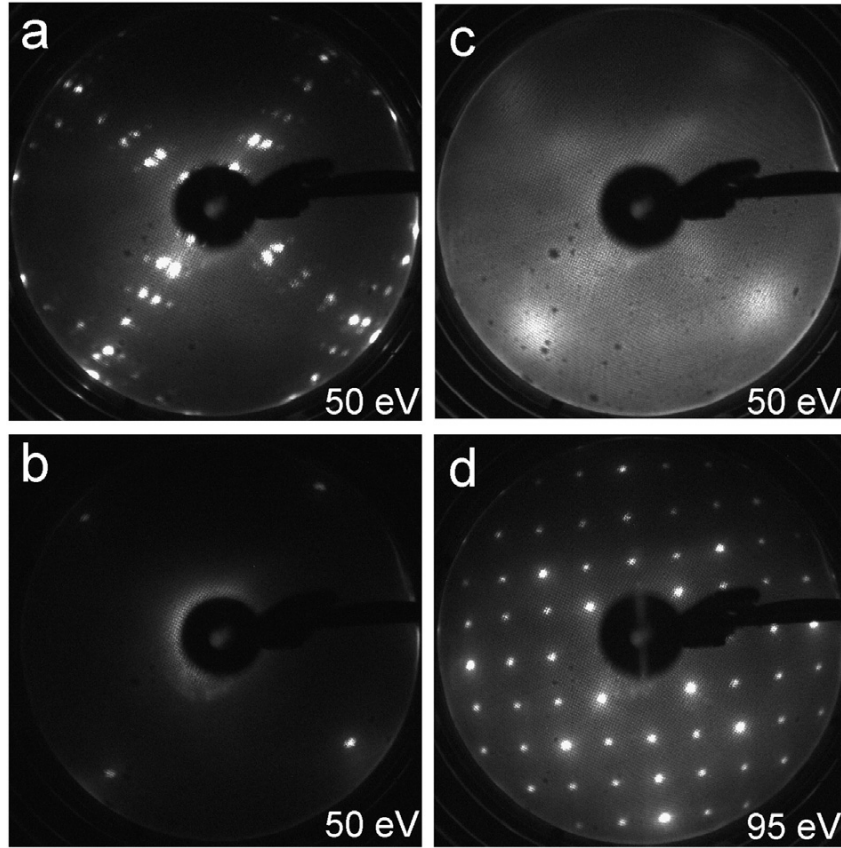


Figure 4.1: LEED patterns, observed at energies as indicated, for the clean Pt(001)-hex reconstructed surface (a); after deposition of 4 nm-thick Fe layer (b); further reactive deposition of 4 nm Fe in 5×10^{-6} mbar of O_2 at 300 K (c); final annealing at 775 K for 100 min (d).

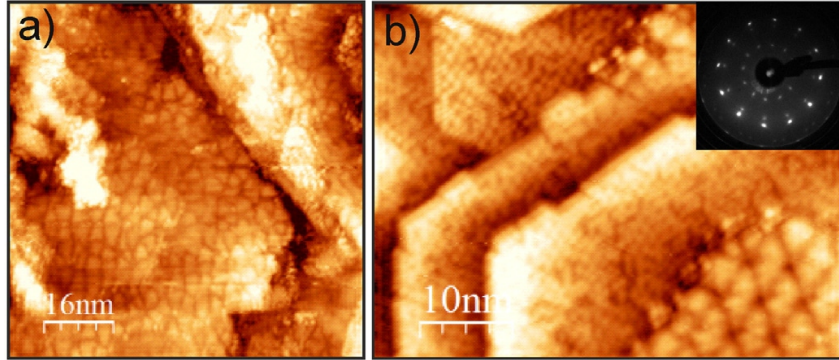


Figure 4.2: STM images of the films prepared by 25 nm Fe reactive deposition on clean Pt(001) and subsequent annealing in UHV at 645 K for 60 min (a) and then at 775 K (b) for 60 min. Tunnelling conditions: (a) bias = -3 V, current = 0.05 nA; (b) -1 V, 0.1 nA. The inset shows the LEED pattern at 95 eV.

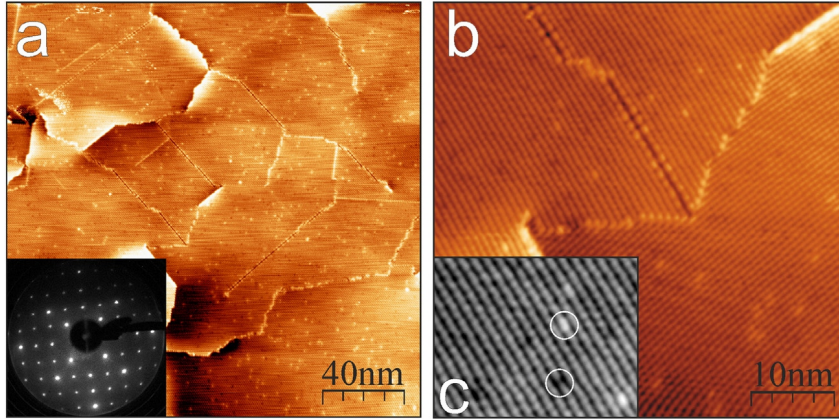


Figure 4.3: STM images of the $\text{Fe}_3\text{O}_4(001)$ film on Pt(001) prepared as described in the caption to Figure 4.1 after additional UHV-annealing at 1020 K for 10 min. In image (c) (size 30 nm \times 24 nm), a vacancy-type defect and an ad-species are highlighted by circles. Tunnelling bias = 1.5 V, and current = 4 nA. Inset in panel (a) shows LEED pattern at 95 eV.

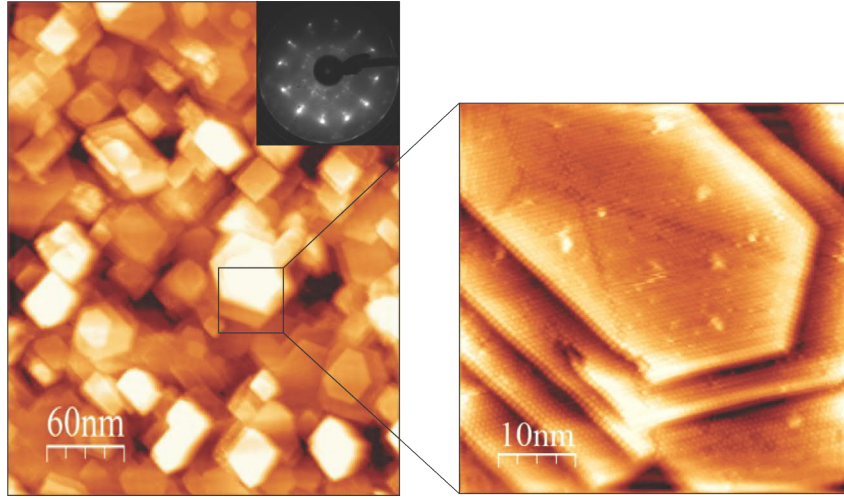


Figure 4.4: STM images and LEED pattern (inset) at 95 eV of the film prepared by reactive deposition at 550 K on top of the 4 nm-thick buffer layer. In addition to rectangular-shaped terraces, those showing the hexagonal shape expose the (111) surfaces as zoomed in. Tunnelling conditions: bias = -3 V, current = 0.2 nA.

Figure 4.5. Nonetheless, the results nicely demonstrate that well-ordered, thin $\text{Fe}_3\text{O}_4(001)$ films can be grown on a $\text{Pt}(001)$ substrate. It is also clear that the presence of a buffer layer several nm thick is necessary for the growth of (001)-oriented films on $\text{Pt}(001)$.

In the next set of experiments, a much thicker Fe buffer layer (~ 50 nm) was deposited on the $\text{Pt}(001)$ surface at 300 K in order to further elucidate the role of the Fe buffer layer in the preparation of $\text{Fe}_3\text{O}_4(001)$ films. An oxide film was then formed by reactive Fe deposition at 550 K in 10^{-5} mbar of O_2 . The sample was further annealed in UHV at 775 K for ca. 60 min. Although the LEED pattern immediately showed an $\text{Fe}_3\text{O}_4(001)-(\sqrt{2} \times \sqrt{2})\text{R}45^\circ$ reconstructed surface, high resolution STM images revealed a different surface from those obtained for the sample that had a 4 nm-thick Fe buffer layer. In fact, the images in Figure 4.6 are virtually identical to those previously reported for a dimer-terminated surface [34]. Since this preparation, in essence, repeats the recipe used by Spiridis et al. for a $\text{MgO}(001)$ substrate, such a similarity in the final structures suggests that the substrate (e.g. $\text{MgO}(001)$ and $\text{Pt}(001)$) itself favours solely the growth of an $\text{Fe}(001)$ buffer layer, which in

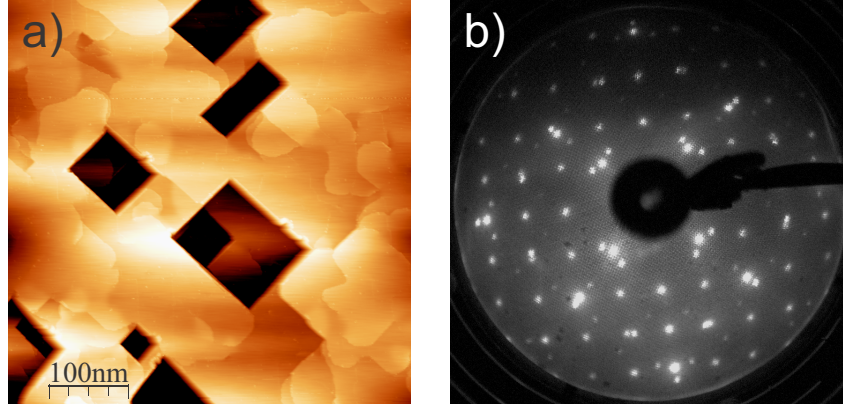


Figure 4.5: STM image (a) and LEED pattern at 95 eV (b) of the film prepared at a higher O_2 pressure of 2×10^{-5} mbar. Tunnelling conditions: bias = -2.9 V, current = 0.10 nA.

turn governs the growth of a (001)-oriented Fe_3O_4 film. It is also clear that the thickness of the buffer layer plays a role in the eventual termination of the film, with the thick layer providing a reservoir of Fe to stabilize an Fe-rich, dimer termination. This would imply that Fe atoms have a high mobility within the Fe_3O_4 bulk. In the case of the thin buffer layer, it may be that the buffer layer becomes entirely oxidized, thereby depleting the source of Fe that would otherwise maintain an Fe-rich termination.

To monitor transformations of the surface of the $Fe_3O_4(001)$ films in more detail, films prepared with a 4 nm-thick buffer layer were examined using STM and LEED as a function of annealing time at 775 K. The film annealed for only 10 min appears to have the dimer termination (Figure 4.7(a)), with additional defect structures, as observed for the preparation of the film with a thick Fe buffer layer (Figure 4.6). The structure continued as the sample was annealed for longer periods of time (Figure 4.7(b)), until it became the B-terminated surface after 100 min (Figure 4.7(c)). The corresponding LEED patterns are shown below the images. Annealing of the as grown films at higher temperatures, up to 1020 K, accelerates this process, but results in the same B-terminated surface. Further oxidation in 10^{-6} mbar of O_2 results in a pristine surface with low defect densities, and this step can be incorporated into the growth procedure.

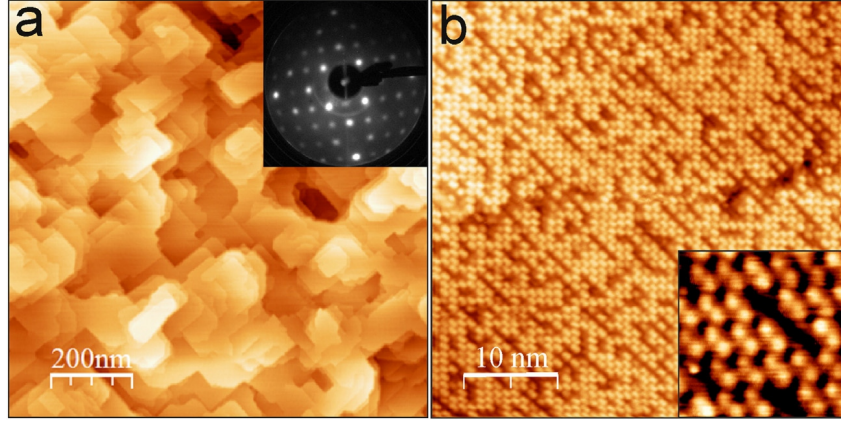


Figure 4.6: Large scale (a) and high-resolution (b) STM images of the film prepared on a 50 nm-thick Fe buffer layer. Tunnelling conditions: bias = -3.0 V, current = 0.10 nA; (inset) -1.5 V, 0.10 nA. Inset in panel (a) shows LEED pattern at 95 eV.

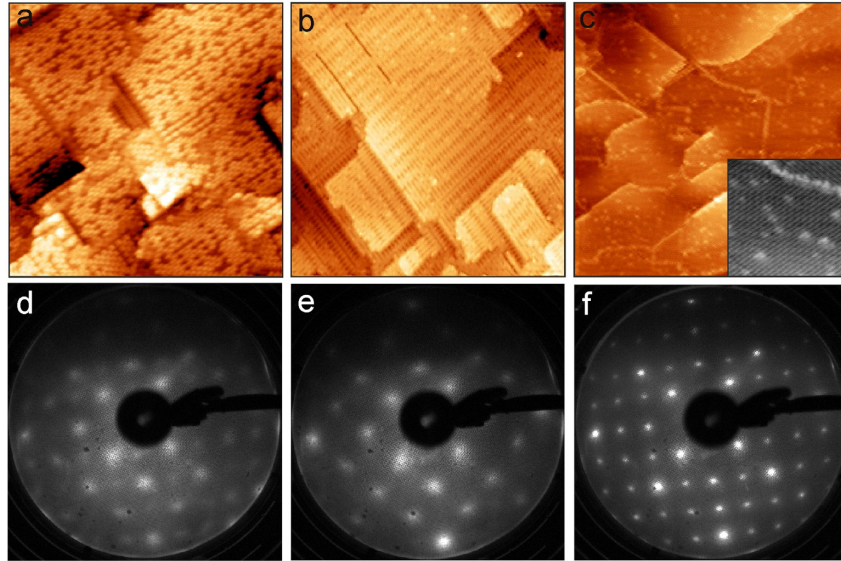


Figure 4.7: (a-c) STM images and (d-f) corresponding LEED patterns at 95 eV of the $\text{Fe}_3\text{O}_4(001)$ film grown on 4 nm-thick Fe buffer layer UHV-annealed at 775 K for 10 (a), 60 (b), and 100 (c) min. Image sizes: 50 nm \times 50 nm (a,b), 100 nm \times 100 nm (c); bias (a,b) = -2 V, (c) = -3 V; current: (a) = 0.1 nA, (b) = 2.0 nA, (c) = 0.64 nA.

The similarity of STM images presented in Figure 4.7 to those achieved by Novotny et al. [35] by depositing Fe onto a B-terminated surface of a single crystal sample is noted. In particular, it is observed that the sample, after 100 min of annealing at 775 K, resembles that of the B-terminated surface with 0.025 ML of Fe deposited at 300 K, implying that this surface still has a slight excess of Fe. The termination observed after 60 min of annealing bears similarities to the surface seen after 0.8 ML of Fe was deposited on the B-terminated surface and then flashed to 423 K. In the latter case, the termination was assigned by Novotny et al. to pairs of octahedrally coordinated Fe-atoms. This structure differs from the dimer model proposed by Spiridis et al. [24, 34] regarding the positions of the Fe atoms. Note, however, that as Spiridis’s model is based on STM studies of films grown on a 20 nm thick Fe buffer layer on MgO(001) at considerably higher temperatures, i.e. 773 K, it may well be that these two models are for two different structures.

Figure 4.7 shows that the Fe-rich, dimer-terminated surface transforms into a mixed Fe and O B-terminated surface upon prolonged annealing. Since the sample annealing was performed in UHV, the transformation indicates diffusion of the surface Fe atoms into the bulk in order to achieve the most stable B-termination observed on single crystal samples. The fact that such a transformation was not observed here for the samples with a much thicker buffer layer suggests that it is the buffer layer that supplies Fe to stabilize the otherwise unstable dimer termination. Spiridis et al. also observed the dimer termination only on films grown on an Fe buffer layer [34]. In the case of the 4 nm buffer layer, this layer may be depleted during annealing, most likely via Fe migration into the Pt crystal bulk. The Fe diffusion across the film may explain the formation of intermediate structures, as shown in Figure 4.8, which appear to be metastable as their formation critically depends on the film preparation conditions.

It is still unclear whether the buffer layer is completely oxidized or if metallic Fe remains underneath and/or migrates into the Pt. However, from this study it is concluded that the thickness of the Fe buffer layer may be used to control the surface termination.

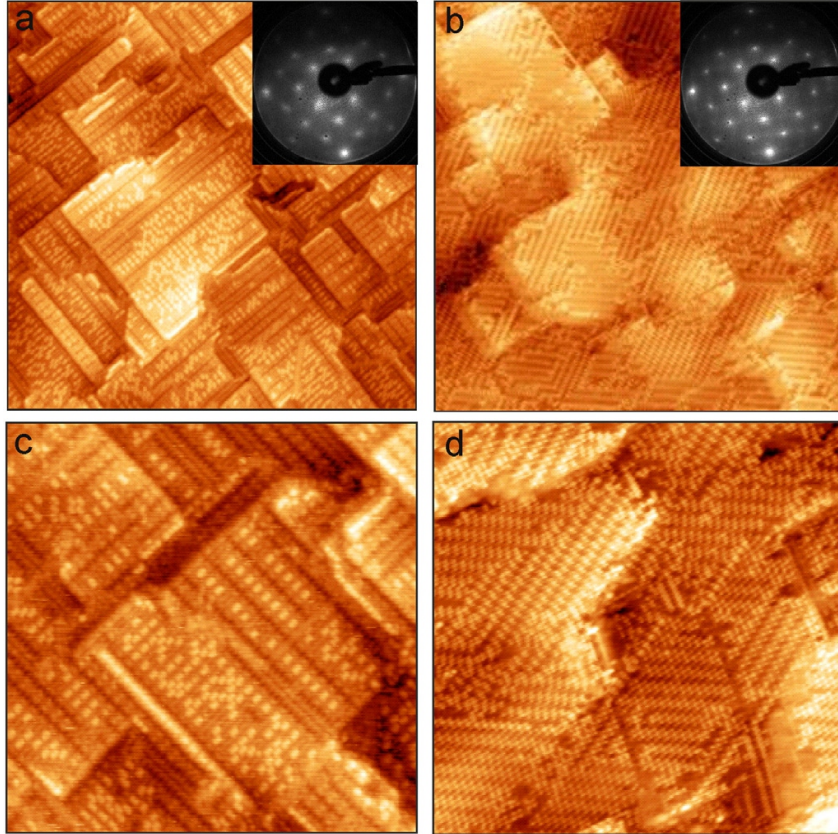


Figure 4.8: STM images of intermediate surface structures observed on the $\text{Fe}_3\text{O}_4(001)$ film grown on 4 nm-thick Fe buffer layer UHV-annealed at 775 K for 40 min (a,c) and 70 min (b,d). Image sizes: 100 nm \times 100 nm (a,b), and 50 nm \times 50 nm (c,d); sample bias = -2 V; current: 2.0 nA (a,c), and sample bias = -1.45 V; current: 0.08 nA (b,d).

4.4 Conclusions

Reproducible growth recipes for $\text{Fe}_3\text{O}_4(001)$ films on $\text{Pt}(001)$ with two stable terminations dependent on growth conditions have been provided. These terminations have the same $(\sqrt{2} \times \sqrt{2})\text{R}45^\circ$ reconstruction, and are not trivial to distinguish without STM. Growth of both of these terminations requires the presence of a buffer layer to balance the stoichiometry of the film and ensure that it grows epitaxially as the (001) surface. Intermediate terminations were observed during the annealing process for the B-terminated surface, with the surface changing from a dimer-like structure through several Fe-rich surfaces before eventual complete transformation to the B-termination, therefore care must be taken to ensure that the surface has fully transformed into the B-termination prior to experiments. This process can also be accelerated through the use of higher temperatures, and a surface with very low defect densities can be achieved by further annealing in oxygen. With the growth of these thin films, it is now possible to do reactivity studies on these surfaces under well-controlled conditions.

Chapter 5

Iron Sulfide Growth

5.1 Introduction

The goal of the work presented in this chapter was to prepare a well-ordered iron sulfide thin film in order to facilitate surface science studies, with a particular aim of producing greigite (Fe_3S_4). As mentioned in Section 1.4, the iron sulfides are abundantly found on earth and play a key role in many biogeochemical and industrial processes [36, 37, 39], however their surface properties are not well understood at the atomic level. Contributing to this paucity of knowledge is the lack of high-purity, single crystal samples for study. This chapter will outline the preparation of such a film, enabling surface science studies to be performed.

5.2 Growth chamber

Film growth was performed in a purpose-built preparation chamber, required in order to avoid S contamination in the analysis chambers used. The chamber was designed to fit with two separate UHV systems, and consisted of a sample stage with heating provided from a lamp, a quartz microbalance (QMB) for calibration of the Fe deposition rate, an EFM3 evaporator from Omicron fitted with a 99.99+ % purity Fe rod from Goodfellow, an independent UHV pumping system, and a sulfur source as described below. It was found that sulfur within the chamber reacted with standard copper sealing gaskets causing cor-



Figure 5.1: Photograph showing the corrosion of copper gaskets caused by sulfur in the growth chamber before their replacement with Ag-plated gaskets.

rosion, as shown in Figure 5.1, prompting their replacement with Ag-plated gaskets.

The first UHV was fitted with facilities for LEED, AES, high resolution electron energy loss spectroscopy (HREELS), and sample sputtering and annealing. The second UHV system had an analysis chamber for performing XPS measurements, LEED with a MCP detector, a quadrupole mass spectrometer (QMS) for temperature programmed desorption (TPD) measurements, an STM, and facilities for sputtering and annealing samples.

5.3 Iron and sulfur sources

A primary consideration for the growth of the iron sulfide film is the method of delivery of the constituent elements. For the iron, a standard molecular beam epitaxy (MBE) source would suffice as in the case for iron oxides, however choosing a source for the sulfur is not so straightforward. Possible delivery methods include using H_2S as a carrier gas or the evaporation of elemental

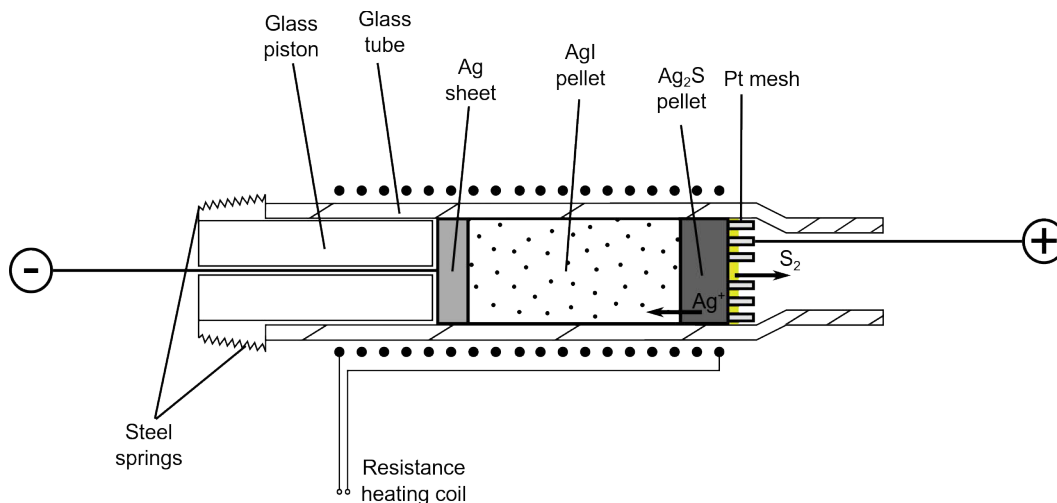


Figure 5.2: Schematic of the electrochemical cell used to deposit sulfur. With the cell heated to 200 °C, applying a potential across the cell allows Ag to be added to or removed from the Ag_2S pellet. When the Ag concentration decreases to a critical value, sulfur sublims on the surface and vaporises into the vacuum chamber.

sulfur within the chamber. Using H_2S was decided against as a first option due to its toxicity. Elemental sulfur evaporates in a range of molecular forms, with S_8 rings being the most stable. In this case, the dissociation barrier of these rings would be a limiting step in the growth process, in addition to a lack of precision in control of the growth process.

From analogy with Fe_3O_4 , it was felt that an optimal solution may include the delivery of S_2 molecules to the surface. A solution for this is the use of an electrochemical cell, first described by Wagner [94]. The cell was constructed in house following the design of Heegemann [95], and a schematic of its design is shown in Figure 5.2.

The cell consists of a Ag sheet as the cathode, a AgI pellet, a Ag_2S pellet, and finally a Pt mesh as the anode, all within a quartz glass tube. A glass piston held in place by springs ensures electrical contact between the components as the volume of the pellets varies, and a type K thermocouple is pressed into contact with the Ag sheet. A heating filament is wrapped around the glass tube and heats the cell to ~200 °C; this is the temperature at which Ag^+ ions become mobile within the Ag_2S pellet. AgI is an ionic conductor,

therefore when a potential is applied across the cell as shown in Figure 5.2, Ag^+ ions flow toward the Ag sheet. Because of the chemical potential this produces at the interface with the Ag_2S pellet, the now-mobile Ag^+ ions move from the Ag_2S into the AgI. This results in a decrease in the Ag concentration in the Ag_2S , and once it reaches a critical value, liquid sulfur is formed and vaporises into the chamber. Under UHV conditions and at $\sim 200^\circ\text{C}$, it has been shown that the sulfur vapour consists almost entirely of S_2 molecules [96]. The rate of formation and evaporation of sulfur molecules is directly proportional to the current passed through the cell, therefore this method of providing sulfur for the film growth ensures consistent and repeatable growth conditions.

5.4 Choosing a substrate

A number of materials were considered for use as a substrate. The first consideration for growth of a well ordered film is the lattice mismatch, as described in Section 1.2.2. Greigite, the sulfide analogue to magnetite, has a cubic inverse spinel structure with a lattice constant of 9.88 \AA . According to some experiments, the (111) surface is active toward CO_2 reduction [97], though greigite nanocrystals produced via hydrothermal synthesis exhibit facets of both (111) and (001) faces (Supplementary material in Ref. [97]). The (111) surface of greigite has a lattice constant of 6.99 \AA . Among the materials considered were platinum, gold, copper, tungsten, molybdenum, iron, silver, and tantalum. Other considerations taken into account include ease of procurement, cost, and preparation requirements for the different potential substrate materials.

5.4.1 Pt(111)

The first substrate for attempting to grow an iron sulfide film was Pt(111). The surface unit cell of Pt(111) is 2.77 \AA , meaning that a ratio of 5:2 between the substrate and film gives a mismatch of 0.9 %. The Pt substrate was cleaned using cycles of sputtering and annealing at 1200 K until a sharp (1×1) pattern was shown by LEED as shown in Figure 5.3(a), before being transferred to the growth chamber. Several growth recipes were attempted.

Fe was deposited at a rate of $0.68\text{ \AA}/\text{min}$ simultaneously with the cur-

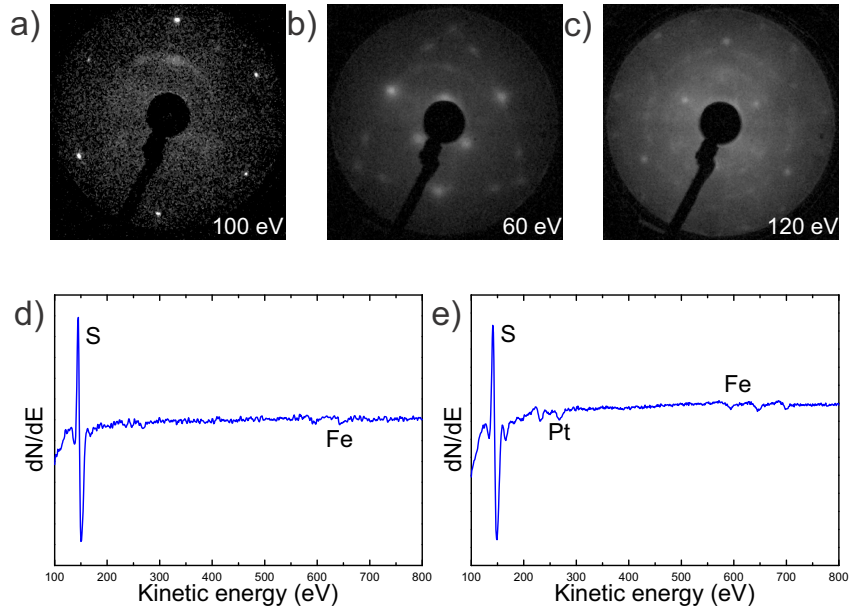


Figure 5.3: LEED images of (a) the Pt(111) substrate, (b) the iron sulfide film following annealing to 875 K, and (c) 925 K, at 100 eV, 60 eV, and 120 eV, respectively. AES spectra of the film (d) immediately following film growth, and (e) following annealing at 925 K.

rent across the sulfur cell $I_S=15$ mA, with the sample at room temperature, for 40 min. The partial pressure of sulfur in the growth chamber P_S was approximately 5×10^{-6} during operation of the cell.

Following growth, no LEED pattern was visible from the sample, and AES showed small Fe peaks relative to S (Figure 5.3(d)). The film was annealed in 50 K steps for 10 min intervals, starting from 375 K, until a LEED pattern became visible. At 875 K a LEED pattern was observed, however it showed signs of faceting on the surface (Figure 5.3(b)). Further annealing to 925 K confirmed this, as shown in Figure 5.3(c), and AES spectra showed the presence of Pt (Figure 5.3(e)), perhaps due to Pt mixing in the film.

In an attempt to prevent this mixing, an Fe buffer layer of 18 nm was incorporated into the growth process. In this case, the Fe deposition rate was 1.8 Å/min, with the sulfur source at the same settings as above. No LEED pattern was visible even following annealing to 775 K for 10 min, and AES again showed only a small amount of Fe was present (Figure 5.4(a)). Further deposition of 5 Å of Fe was performed, and AES showed a large increase in Fe content (Figure 5.4(b)). A LEED pattern became faintly visible following annealing at 525 K (Figure 5.4(c)), however was worsened by annealing to 775 K, and after annealing to 875 K LEED spots from the substrate were visible (Figure 5.4(d)) and the AES spectrum in Figure 5.4(e) showed a large Pt component corresponding to approximately 60 % of the total atomic concentration, according to the relative sensitivity factors given in the Handbook of Auger Electron Spectroscopy [98].

In conclusion, it became apparent that heating the sample to temperatures required for ordering of a film caused a gradual loss of Fe, most likely into the Pt bulk. This effect of Fe and Pt intermixing is not unknown [88, 99, 100], and is also seen to a lesser extent in Chapter 4.

5.4.2 Pt(001)

A change of approach was decided to test if growth of the (001) surface of greigite was possible using Pt(001). According to Ref. [97], the main surface exposed by greigite nanocrystals is the (001) surface. If this surface is more stable, it may be that the increased stability inhibits migration of Fe into the

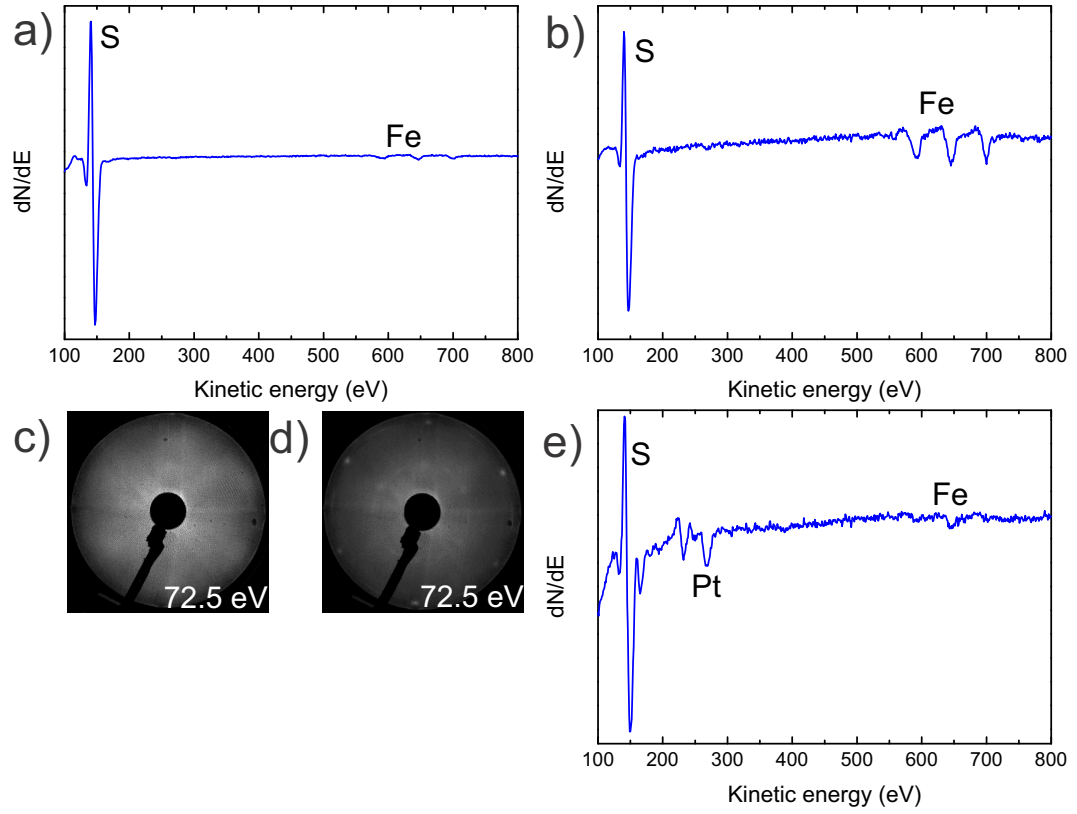


Figure 5.4: AES spectra from the second iron sulfide film grown on Pt(111) (a) immediately following film growth, (b) following further deposition of 5 Å of Fe, and (e) following annealing at 875 K, and LEED images at 72.5 eV following annealing at (c) 575 K, and (d) 875 K.

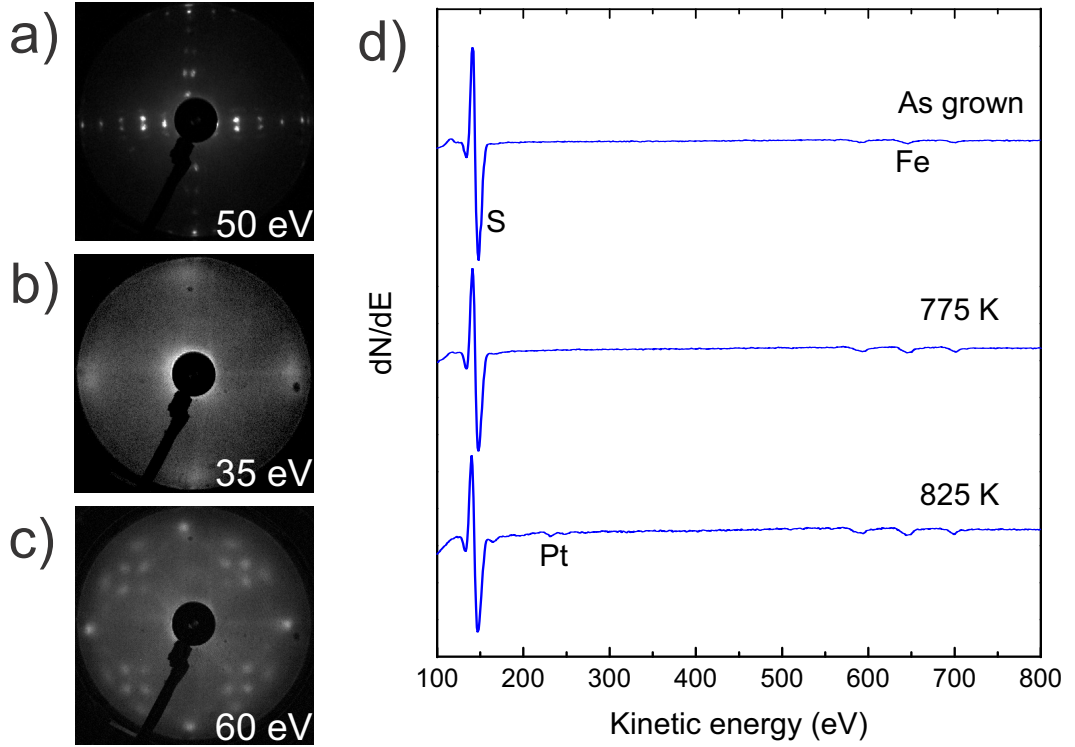


Figure 5.5: LEED patterns from (a) the Pt(001) substrate showing the hex reconstruction, and films following annealing at (b) 475 K, and (c) 775 K, and (d) AES spectra from the film after growth and following annealing at 775 K and 825 K.

Pt bulk. Considering the bulk lattice constant of Pt of 3.94 Å and the greigite (111) lattice constant of 9.88 Å, the 5:2 ratio of the lattice constants again gives a lattice mismatch of 0.9 %. The Pt(001) surface was cleaned via cycles of sputtering and annealing at 1200 K until the Pt(001)-hex reconstruction was clearly visible (Figure 5.5(a)) and no contamination was observed using AES.

Initial preparation attempts incorporated an Fe buffer layer of 10 nm, followed by growth of a sulfide film with various deposition parameters. Using an Fe deposition rate of 2.5 Å/min and $I_S = 15$ mA for 5 min, AES spectra showed only a small amount of Fe relative to S, as shown in Figure 5.5(d). Faint ordering was visible following annealing to 475 K (Figure 5.5(b)). Ordering of

the surface, as judged by LEED, was only clearly visible following annealing to 775 K, and produced a LEED pattern as shown in Figure 5.5(c), and AES spectra showed an increase in Fe. Further annealing to 825 K caused Pt peaks to appear in the AES spectrum.

Preparations using various rates of deposition were used in an attempt to reduce the high concentration of sulfur. Using an Fe buffer layer of ~ 20 nm, an iron sulfide film was deposited with an Fe deposition rate of $3 \text{ \AA}/\text{min}$ and $I_S = 0.15 \text{ mA}$ for 5 min, after which a diffuse LEED pattern became visible (Figure 5.6(b)), and the atomic concentration of Fe in the AES spectrum was $\sim 17 \%$ (Figure 5.6(d)). Following annealing of the film to 575 K for 10 min, the background in the LEED image was reduced, and additional spots became visible, as can be seen from Figure 5.6(c). From the position of the spots relative to those of the Pt substrate (Figure 5.6(a)), rotated 45° from the substrate unit cell spots and at a $\frac{\sqrt{2}}{2}$ smaller distance from the centre, it is estimated that the lattice constant of this film is $\sim 5.55 \text{ \AA}$, which is similar to the lattice constant of pyrite (5.42 \AA). The AES spectrum (Figure 5.6(e)), however, shows the presence of Pt in the film and a small O contamination peak.

The growth chamber was moved to the second UHV system and a newly polished Pt(001) crystal was used as a substrate. A film was grown on top of a 10 nm buffer layer, with 4 min of deposition time of Fe at a rate of $4.5 \text{ \AA}/\text{min}$ and $I_S = 15 \text{ mA}$. Following annealing to 800 K, the film showed an ordered structure, with high background intensity, as shown in Figure 5.7(a), however XPS (Figure 5.7(b)) showed that there was a large concentration of Pt within the film, implying either decomposition, diffusion, or dewetting of the deposited film.

The next growth attempts on this substrate used a reduced Fe deposition rate of $2.76 \text{ \AA}/\text{min}$ for 6 min with the simultaneous deposition of S with $I_S = 15 \text{ mA}$ on top of a 10 or 20 nm thick Fe buffer layer. Following annealing to 750 K, the LEED pattern shown in Figure 5.5(c) was again observed, with lower background intensity, shown in Figure 5.8(a). XPS showed that Pt was absent from the sample surface (Figure 5.8(b)), and the ratio of Fe to S was approximately 1:1. Quantification was done using the Fe 3p and S 2p peaks, as their proximity reduces the contribution of the transmission function of the

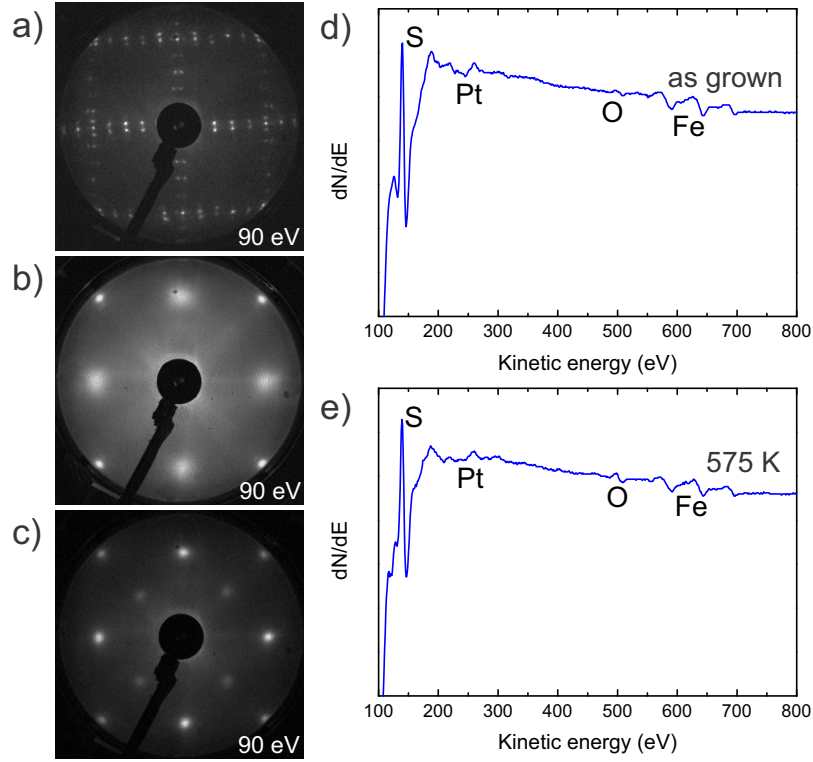


Figure 5.6: LEED patterns at 90 eV from (a) the Pt(001) substrate showing the hex reconstruction, and the iron sulfide film grown using a reduced S deposition rate following (b) film growth, and (c) annealing at 575 K, and AES spectra from the film (d) after growth and (e) following annealing at 575 K.

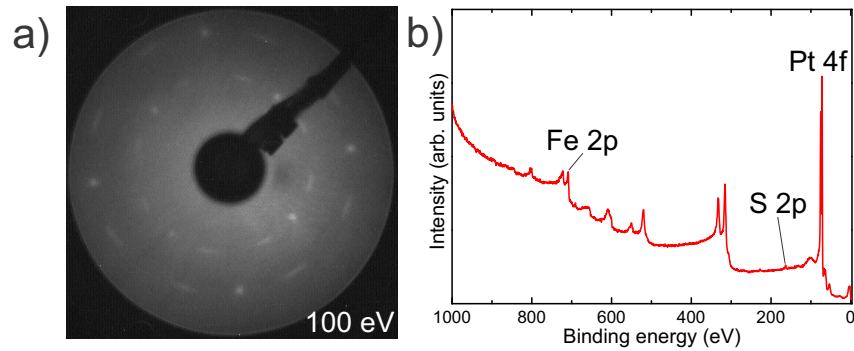


Figure 5.7: (a) LEED pattern at 100 eV following annealing to 800 K of an iron sulfide film grown on Pt(001) using a 10 nm buffer layer, and (b) survey XPS spectrum showing large presence of Pt within the film relative to Fe and S.

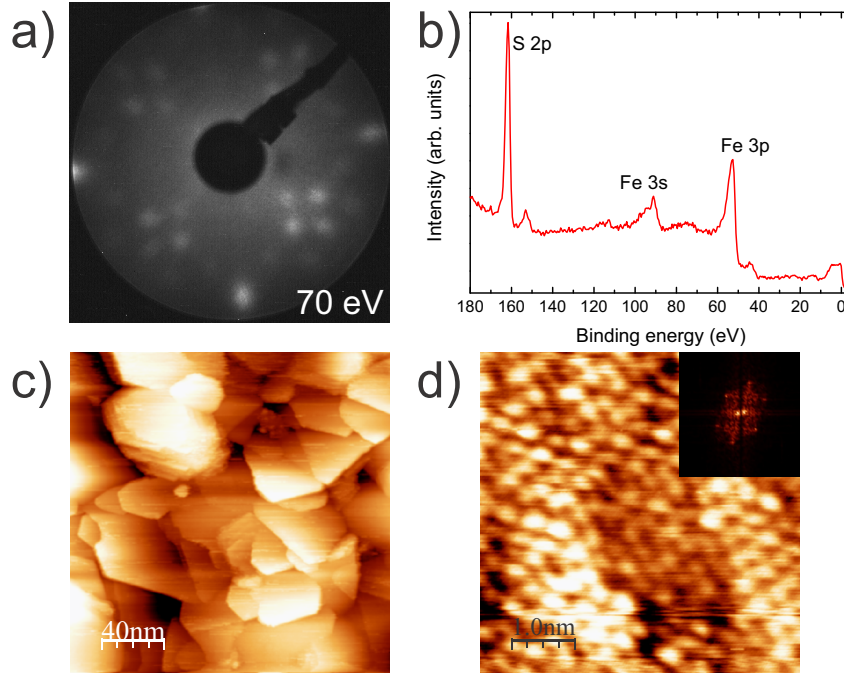


Figure 5.8: (a) LEED pattern from iron sulfide film grown on an Fe buffer layer on Pt(001) following annealing to 750 K. (b) XPS spectrum showing the absence of Pt from the sample surface and a 1:1 ratio of Fe and S. (c) and (d) STM images of film showing hexagonal morphology, with inset of (d) showing its FFT. Tunneling conditions: (c) bias = 0.97 V, current = 0.055 nA, (d) bias = -2.0 V, current = 0.2 nA.

analyser and the IMFP of the electrons through the sample, and the relative sensitivity factors were taken from Yeh and Lindau [73]. STM images (Figures 5.8(c) and 5.8(d)) from this sample showed hexagonally shaped terraces of varying sizes. Indeed the FFT in the inset to Figure 5.8(d) shows a hexagonal atomic periodicity at the surface.

The sample was further annealed in the presence of S_2 ($I_S = 15$ mA) at 775 K to try to increase the S content of the film, improve the ordering at the surface, and prevent the loss of material from the film. XPS (Figure 5.9(b)) shows that the ratio of Fe to S following this annealing in S_2 was approximately 1:1.9. This led to the observation of a clock-like LEED pattern (Figure 5.9(a)). Further annealing to 800 K led to increased ordering (Figure 5.9(c)), but also an increase in Pt observed in the film in XPS spectra (Figure 5.9(d)). Anneal-

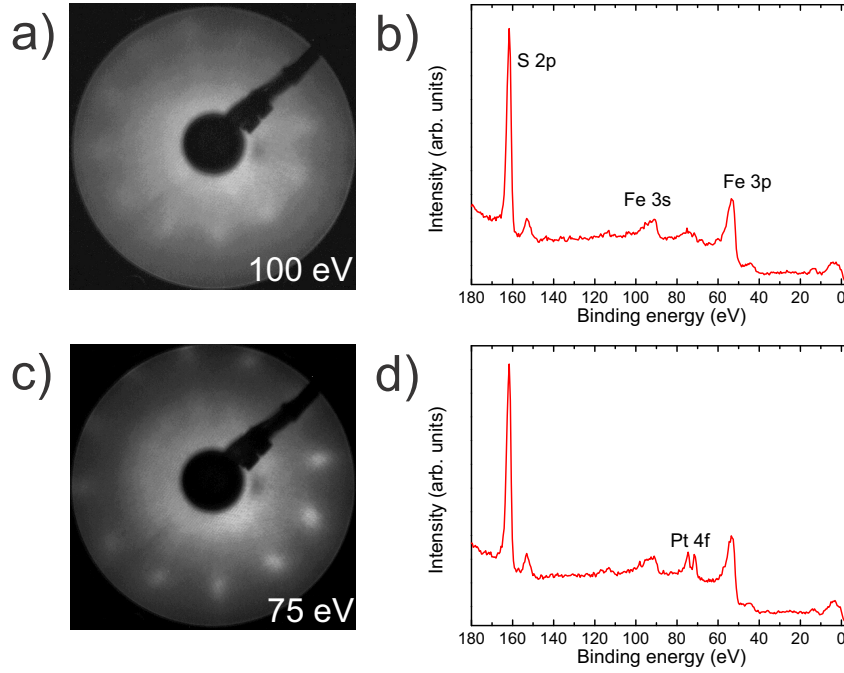


Figure 5.9: (a) LEED pattern and (b) XPS spectrum of iron sulfide film annealed in the presence of S_2 at 775 K, and (c,d) following further annealing at 800 K in UHV.

ing above 800 K did not improve the film quality and led to decomposition of the film.

Having recognised that annealing while depositing S_2 led to a hexagonal clock-like LEED pattern, higher temperature during growth was used. Without using a buffer layer, an iron sulfide film was grown at 775 K using an Fe deposition rate of $1.7 \text{ \AA}/\text{min}$ and $I_S = 15 \text{ mA}$ for 30 min. The LEED pattern from this film showed many spots from the overlaying of patterns from two different structures Figure 5.10(a). One of the structures was of hexagonal symmetry, with rotational domains resulting in a clock-like pattern. The other structure had a square LEED pattern. Annealing to 775 K in UHV led to the some of the spots to move closer together, forming a cross-like shape (Figure 5.10(b)). In both cases the XPS spectra showed a large Pt peak corresponding to an atomic concentration of $\sim 35 \%$ and the ratio of Fe to S was approximately 2:3 (Figure 5.10(f)). Annealing to 825 K brought spots from the square pattern ever closer together, as shown in Figure 5.10(c). Further

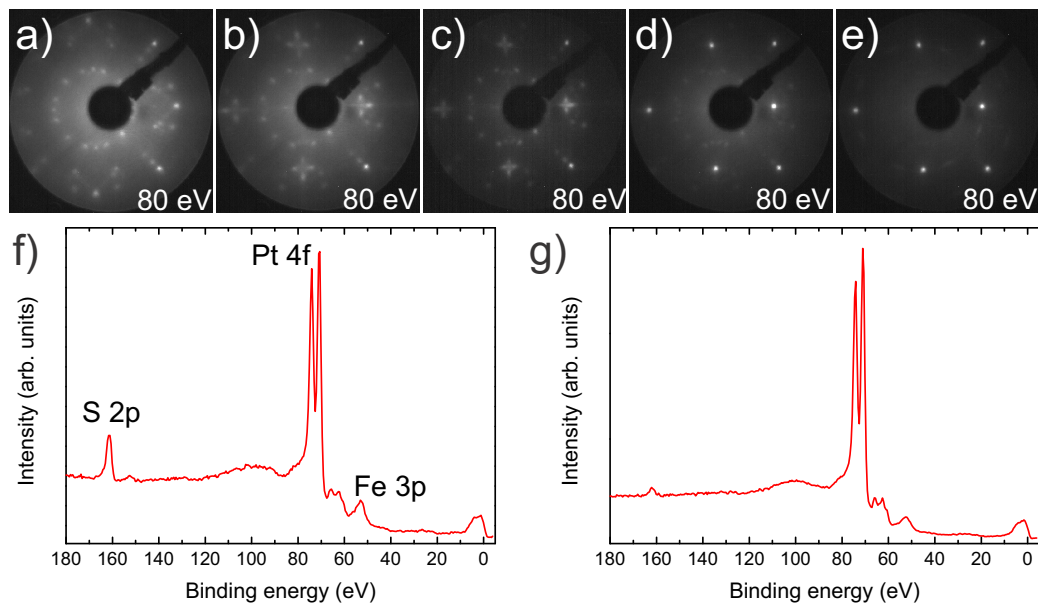


Figure 5.10: LEED patterns from an iron sulfide film grown at 775 K (a) following growth, and following annealing in UHV at (b) 775 K, (c) 825 K, (d) 875 K, and (e) 900 K, and XPS spectra of the film following annealing at (f) 775 K and (g) 900 K.

annealing at 875 K led to the cross-like arrangement of spots to converge into a single sharp spot (Figure 5.10(d)), and annealing to 900 K resulted in a LEED pattern (Figure 5.10(e)) similar to that shown in Figure 5.7(a). XPS (Figure 5.10(g)) showed that the surface now consisted mainly of Pt (~65 %).

The above preparation method was repeated, however for 150 min for a much thicker film and to try to prevent Pt migration or loss of material from the film, however after annealing to 800 K, Pt was again visible in XPS spectra. In order to discover the temperature of decomposition of the film, a TPD experiment was performed. The sample was heated at a constant rate of 0.5 K/s from 200-865 K in front of a QMS and the desorption of atoms and molecules from the surface was detected. As can be seen from Figure 5.11, there is a peak in desorption of S (mass 32) at ~850 K, which corresponds to S desorbing due to decomposition of the film. In the inset of Figure 5.11 it can be seen that an exponential increase in desorption begins from ~700 K.

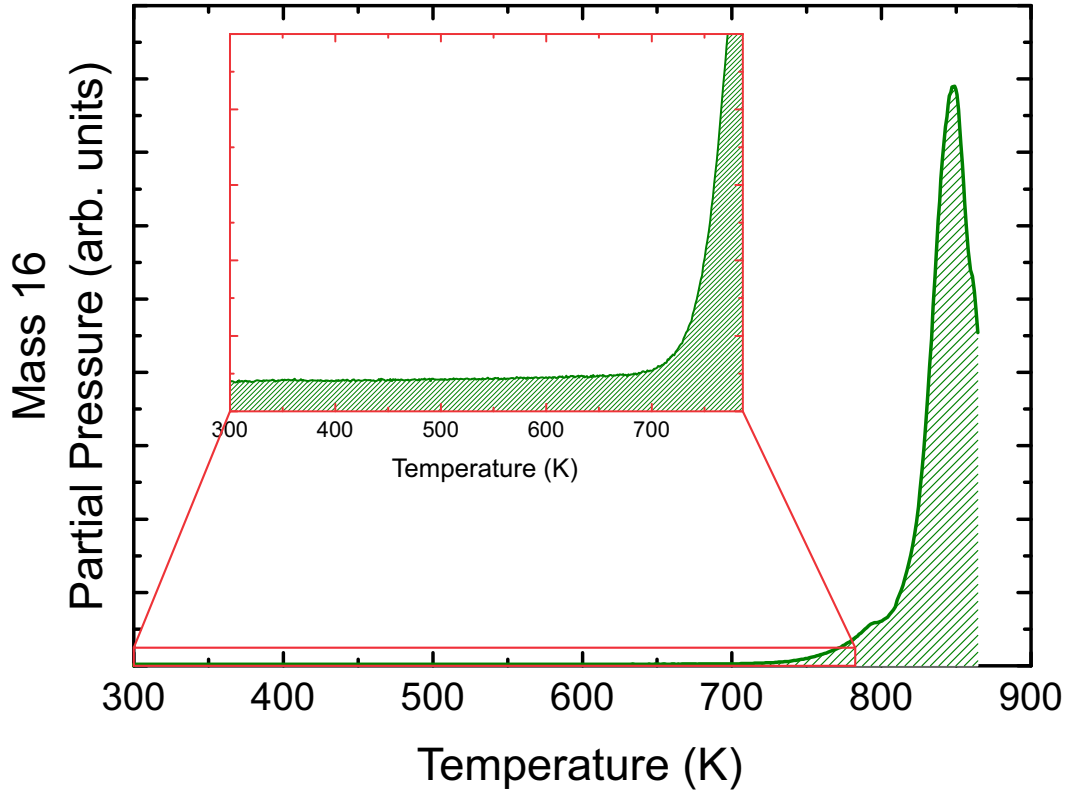


Figure 5.11: Mass 32 TPD spectrum from an iron sulfide film prepared on Pt(001) showing a large sulfur desorption peak at ~ 850 K, with an onset of desorption, shown in the inset, at ~ 700 K.

These numbers provide an upper limit for annealing of prepared films, and shows that the loss of material from the film is due to a combination of S evaporation due to decomposition and Fe diffusing into the Pt substrate.

A final attempt at growth on the Pt(001) substrate was attempted. The deposition rate for Fe was $1.65 \text{ \AA}/\text{min}$ with $I_S = 15 \text{ mA}$ for 30 min, and the sample temperature was 625 K. Following film growth, LEED showed a clock-like pattern without the additional spots as observed previously (Figure 5.12(a)), however annealing to 650 K caused the appearance of four additional spots from the substrate (Figure 5.12(b)) and the appearance of Pt in the XPS spectra. A simulated LEED pattern of Fe_3S_4 is shown in Figure 5.12(c), showing similarity with the observed LEED pattern from the film and its relationship with the substrate, giving an estimate of $\sim 7.0 \text{ \AA}$ for the film lattice parameter. Further annealing at 650 K only resulted in a marginal

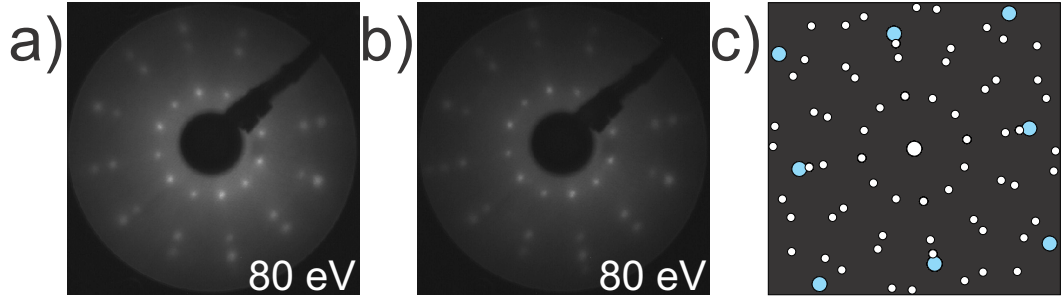


Figure 5.12: LEED patterns from a film grown at 625 K (a) following growth, and (b) after annealing in UHV at 650 K, and (c) a simulated LEED pattern for $\text{Fe}_3\text{S}_4(111)$ on $\text{Pt}(001)$ showing substrate spots in pale blue.

decrease in background intensity. Annealing at higher temperatures led to increased intensity of the substrate spots in LEED and of the Pt peaks in XPS.

5.4.3 Au(111)

Because intermixing of Pt and Fe prevented annealing of iron sulfide films to temperatures that produce highly ordered surfaces, Au was chosen as a substrate. The (111) surface of Au was chosen because of the apparent preference of the iron sulfide film to grow with a hexagonal structure. The lattice constant of Au is 4.08 Å, giving a surface lattice parameter of 2.88 Å. This results in a lattice mismatch of 3 % with an $\text{Fe}_3\text{S}_4(111)$ film.

The Au crystal was cleaned through cycles of sputtering and annealing at ~900 K, until a hexagonal LEED pattern was visible as shown in Figure 5.13(a) and no contamination was seen using XPS. Films were grown with an Fe deposition rate of 1.6-2.1 Å/min and $I_S = 5$ mA for 30 min, with the sample held at 625 K. A hexagonal LEED pattern was immediately visible following growth, as shown in Figure 5.13(b), which became sharper and contained less background intensity following annealing for 10 min at 650 K (Figure 5.13(c)). A comparison with the LEED pattern of Au(111) at 127 eV, as shown using the blue circles in Figure 5.13(d), reveals that the film has a unit cell ~2.5 times larger than that of Au(111), i.e. ~7.2 Å, however dis-

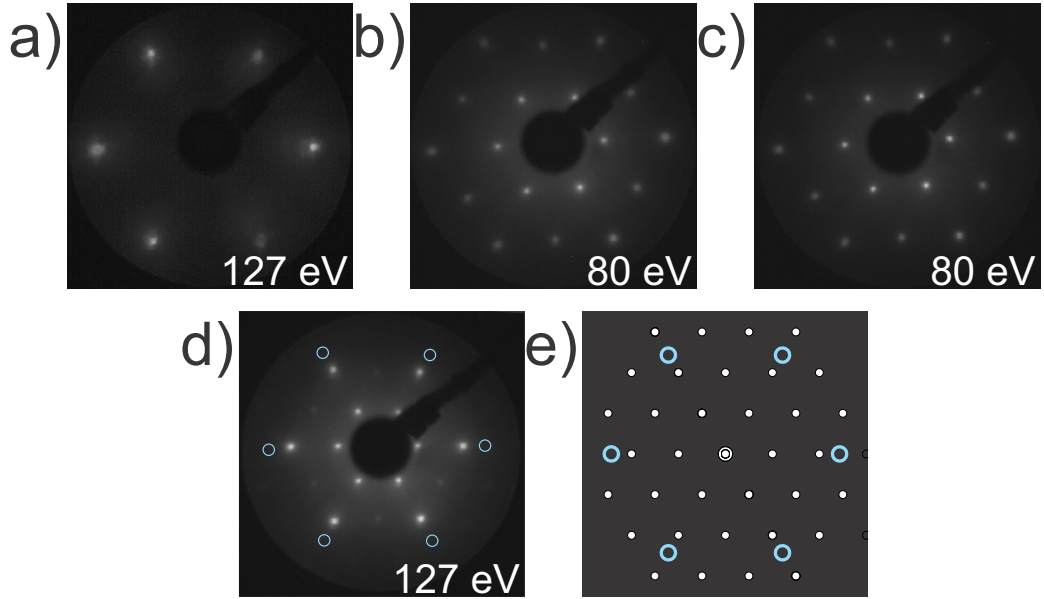


Figure 5.13: LEED patterns from (a) the cleaned Au(111) substrate, (b) the first iron sulfide film following growth at 625 K, (c) following further annealing in UHV at 650 K, (d) at 127 eV with an overlay of the positions of the Au(111) spots from (a) as pale blue circles, and (e) a simulated LEED pattern of $\text{Fe}_3\text{S}_4(111)$ on Au(111) showing substrate spots as pale blue circles.

tortion of the LEED pattern caused by the use of a MCP detector prevented precise measurement of the surface lattice constant. An undistorted simulation of the LEED pattern of an $\text{Fe}_3\text{S}_4(111)$ film (lattice constant 7.0 \AA) on Au(111) is shown in Figure 5.13(e) for comparison.

Additional deposition of Fe and S on top of the previously grown film in the same manner as described above, followed by annealing at 700 K in ambient S_2 ($I_S = 5 \text{ mA}$) and annealing in UHV at 700 K, resulted in a LEED pattern with very low background intensity, indicating a highly ordered film (Figure 5.14(a)). XPS spectra from these films (Figure 5.14(b)) showed an approximate Fe:S ratio of 1:1.9, as calculated from the areas of the Fe 3p and S 2p peaks. The area of the Au 4f peaks indicated a total Au concentration of $<1 \%$.

Deposition of 1.4 \AA of Fe on top of an iron sulfide film at room temperature led to a different LEED pattern being recorded, as shown in Fig-

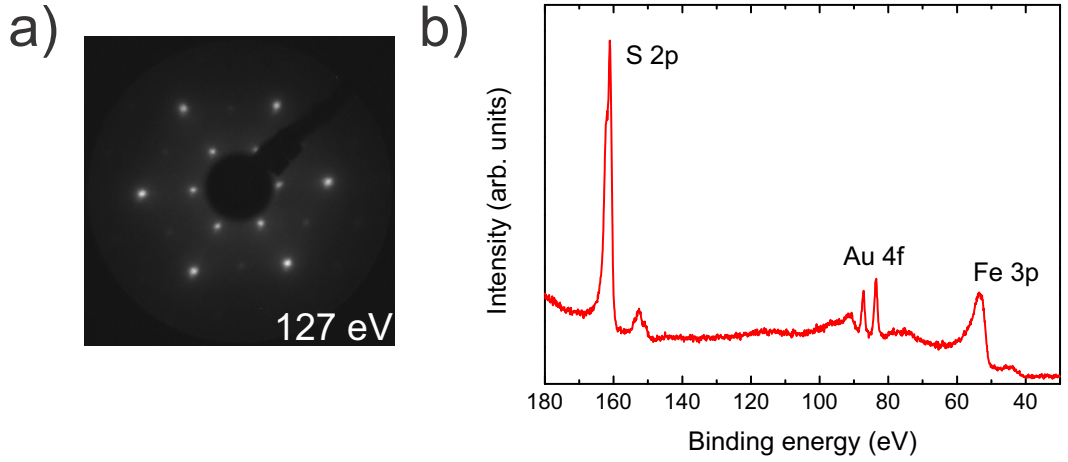


Figure 5.14: (a) LEED pattern and (b) XPS spectrum from iron sulfide film following annealing in ambient S_2 at 700 K followed by UHV annealing at the same temperature.

ure 5.15. This reconstruction, however, was no longer visible following annealing at 550 K for 5 minutes. Following further deposition of 1 nm of Fe on the film, no LEED pattern was observed, however annealing at 550 K for 5 minutes produced the same LEED pattern as shown in Figure 5.15. This LEED pattern was no longer visible following a further 10 minutes annealing at 550 K. The LEED pattern is a $(\sqrt{3}/2 \times \sqrt{3}/2)R30^\circ$ reconstruction with respect to the periodicity of the film surface prior to Fe deposition. The lattice parameter from the newly observed LEED spots is ~ 6.0 Å, which is similar to the lattice parameter for troilite FeS (5.997 Å). The disappearance of these LEED spots following annealing could be due to Fe migrating into interstitial sites within the bulk of the iron sulfide film, or alternatively migrating into the bulk of the Au substrate.

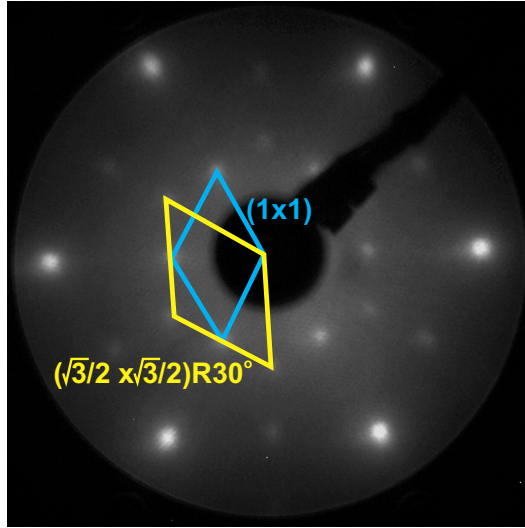


Figure 5.15: LEED pattern at 80 eV taken from the iron sulfide film following the deposition of 1.4 Å of Fe.

5.5 Conclusions

A growth recipe for the preparation of well-ordered, single crystal iron sulfide films has been discovered, using Fe deposited via MBE and S from an electrochemical cell. The growth process requires a separate growth chamber to protect UHV components from corrosion by the sulfur. A Au(111) crystal was used as a substrate for the well-ordered films, giving a ratio of approximately 5:2 of lattice constant with the iron sulfide layer. Attempts to grow iron sulfide films on a Pt substrate were hindered by the migration of Fe into the Pt bulk. Characterisation of the stoichiometry and structure of these films are the topics of Chapter 6.

Chapter 6

Iron Sulfide Film Characterisation

6.1 Introduction

The successful discovery of a growth recipe for well-ordered iron sulfide films that can be studied using surface science tools is presented in Chapter 5. The next requirement is the characterisation of the film. As seen in Section 1.4, there is a wide range of compositions for iron sulfide materials, therefore it is of great importance to characterise the films resulting from this growth procedure. This is the focus of this chapter. The techniques used for characterisation are XPS, STM, I/V-LEED, and XRD. The iron sulfide films studied in this chapter were grown using the recipe given in Section 5.4.3, using a Au(111) substrate, an Fe deposition rate of 1.6-2.1 Å/min, and a current across the sulfur source of $I_S = 5$ mA. The films were grown to thicknesses of 5-20 nm.

6.2 XPS

As mentioned in Section 5.4.3, the ratio of Fe to S determined from XPS for the iron sulfide layers was approximately 1:1.9. This alone would indicate a stoichiometry close to FeS₂, however, in addition to the usual error margins inherent in quantification, a study by McIntyre et al. led to the conclusion that XPS quantification for iron sulfides consistently gives higher S ratios than expected due to factors such as surface reconstructions and poor description of background intensities [101, 102]. For further analysis, the Fe 2p and S 2p

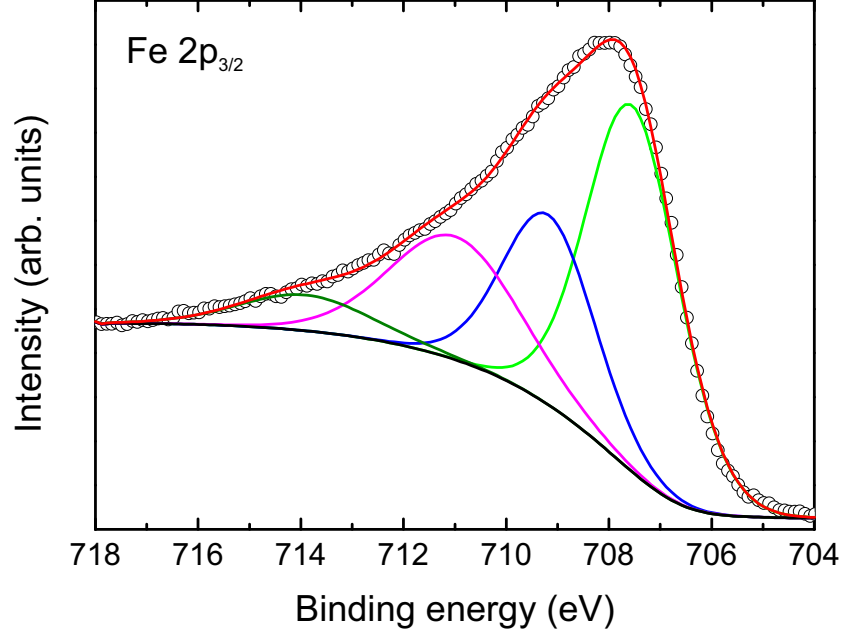


Figure 6.1: XPS spectrum of the Fe 2p peak from the iron sulfide film. The peak has been fitted with four peaks, at 707.5 eV, 709.2 eV, 711.0 eV, and 713.9 eV based on values found in literature for iron sulfides [103–105].

regions of the XPS spectrum were measured using Mg K α radiation in the second UHV chamber described in Section 5.2.

6.2.1 Fe 2p

The Fe 2p_{3/2} region shown in Figure 6.1 has been fitted with four peaks, at 707.5 eV, 709.2 eV, 711.0 eV, and 713.9 eV, above a Shirley background. In iron sulfide materials, the peak at 707.5 eV is commonly assigned to Fe(II)-S and the peaks at 709.2 eV and 711.0 eV to Fe(III)-S. The peak at 713.9 eV is assigned to a satellite peak [103–105]. The peak areas and assignments are given in Table 6.1.

In XPS spectra of pyrite, the Fe 2p_{3/2} peak is dominated by the Fe(II)-S (Fe²⁺ bonded to sulfur within the lattice) peak, as the Fe in the pyrite bulk is in the Fe²⁺ oxidation state. There are additionally minor contributions due to Fe²⁺ and Fe³⁺ surface states [106]. This is true for both the mainly-studied (001) surface and the (111) surface [107]. Here, however, the contribution of

Table 6.1: Table of XPS Fe 2p peak assignments for the iron sulfide film.

Chemical state	Binding energy (eV)	FWHM (eV)	Area (%)
Fe(II)-S	707.5	2.0	43
Fe(III)-S	709.2	2.0	23
Fe(III)-S	711.0	3.0	26
Fe(II)-S satellite	713.9	3.0	8

the peaks assigned to Fe(III)-S is equal to that of the Fe(II)-S, indicating that both Fe^{2+} and Fe^{3+} are present throughout the film. This ratio of Fe(II)-S and Fe(III)-S is also present if the Fe $2p_{3/2}$ peak is fitted using the multiplets theoretically derived by Gupta and Sen for free ions [103, 108]. The ratio of Fe^{2+} to Fe^{3+} in this film is smaller than that found for pyrrhotite, which contains $\sim 68\%$ Fe(II)-S [103], but closer to the ratio of 56% Fe(II)-S obtained for troilite [105]. The spectra of both troilite and pyrrhotite display a more pronounced shoulder on the lower binding energy side of the Fe $2p_{3/2}$ peak. This has been explained by the increased Fe concentration leading to smaller distances between Fe atoms which interact, producing a binding energy peak at the energy expected for metallic iron [109]. The only Fe 2p XPS spectrum from greigite found for comparison contained a large oxide component and was not well-resolved [110], however from the inverse spinel structure, without taking into account the surface region, it would be expected that the amount of Fe^{3+} would be twice that of Fe^{2+} .

A comparison of the Fe 2p peak for spectra recorded at normal emission and at 60° of photoemission showed no difference between the shape of the peaks. This seems to indicate that none of the components fitted to the Fe $2p_{3/2}$ peak in Figure 6.1 are specifically associated with surface states. This could be due to a surface terminated with S, with Fe atoms in the subsurface retaining bulk-like positions.

6.2.2 S 2p

For pyrite samples, the main doublet peak corresponding to bulk sulfur is located between 162.5 and 162.8 eV, with surface peaks occurring to lower binding energy [107, 111–114]. Pyrrhotite samples, both monoclinic and hexagonal, exhibit a main peak at ~ 161.2 eV, with an additional doublet at ~ 162.2 eV,

corresponding to fivefold and sixfold coordinated sulfur, respectively. The fivefold coordinated sulfur accounts for $\sim 80\%$ of the total peak area [61, 103]. Additionally, a surface contribution is observed at ~ 160.8 eV for hexagonal pyrrhotite Fe_7S_8 when using a photon energy of 210 eV [61]. Similarly, troilite contains two doublets, at approximately 161.3 and 161.9 eV, also corresponding to fivefold and sixfold coordinated sulfur. In this case, the main doublet is the one at 161.9 eV, as the majority of Fe sites are filled within the troilite lattice leading to higher coordination for the sulfur atoms [105, 109]. A single S 2p XPS spectrum taken from non-oxidised greigite exists in literature, taken using a photon energy of 260 eV. This spectrum was fitted using two doublets of near-equal intensity, at approximately 161.2 eV and 161.9 eV, with the peak at lower binding energy being assigned to surface S atoms.

The S 2p region of the XPS spectrum of the iron sulfide film studied here (Figure 6.2(a)) was fitted using Voigt doublets (50 % Gaussian, 50 % Lorentzian), constrained following the method of Nesbitt et al. [61] such that the S $2p_{1/2}$ and S $2p_{3/2}$ peaks had the same full-width at half-maximum (FWHM) and the S $2p_{1/2}$ peak was of half the area and at +1.19 eV relative to the S $2p_{3/2}$ peak. Figure 6.2(a) shows the S 2p region from the sample acquired at normal emission, fitted with three doublets at 161.4 eV, 162.5 eV and 163.7 eV. The separation of the peaks at 161.4 eV and 162.5 eV of ~ 1.1 eV most closely resembles the separation found in pyrrhotite, and as such a similar assignment to fivefold and sixfold coordinated sulfur can tentatively be made, leading to the conclusion that the film is sub-stoichiometric with respect to FeS. The broad peak at 163.7 eV (FWHM = 2 eV) could either be due to elemental sulfur [101] or an energy loss feature as observed for pyrite [115, 116]. Intensity in this region is also observed on pyrrhotite [61].

Figure 6.2(d) shows the evolution of the S 2p spectrum as the angle of photoemission is varied. The peaks acquired at normal emission and at 70° (grazing) are normalised and compared in Figure 6.2(b), and a line is added to the graph to show the grazing spectrum subtracted from the spectrum at normal emission. A doublet at ~ 160.9 eV is observed in this difference spectrum, which is assigned to surface species from the sulfide. Figure 6.2(c) shows the fit of the spectrum at 70° , with the surface peak, and other parameters constrained to be the same as in the spectrum at normal emission. This surface

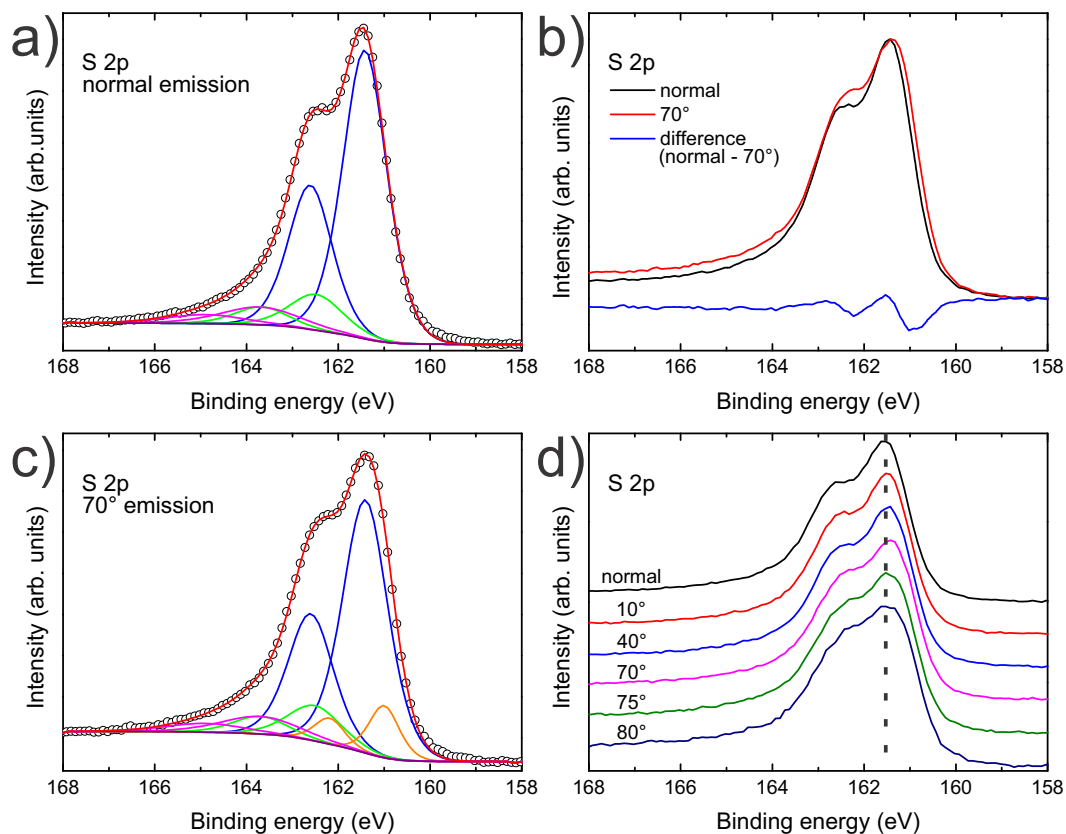


Figure 6.2: (a) S 2p XPS spectrum from the iron sulfide film at normal emission fitted with three doublets at 161.4 eV, 162.5 eV, and 163.7 eV, (b) difference spectrum of the S 2p spectra from the sample taken at normal emission and at 70°, showing the presence of a doublet at ~160.9 eV, (c) S 2p spectrum from the film at 70° fitted with doublets as in (a) and an additional surface doublet at ~160.9 eV, (d) S 2p spectra from the sample as the angle is varied, showing the change in the shape of the S 2p region as the surface components become more prominent.

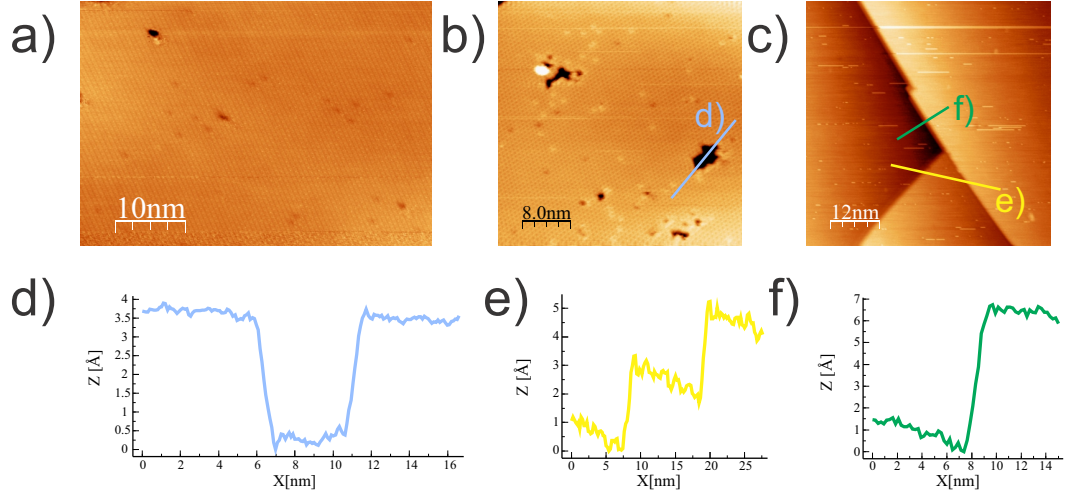


Figure 6.3: (a-c) Large scale STM images of the iron sulfide film. Tunnelling conditions: (a) bias, $V = 1.50$ V, current, $I = 8.72$ nA, (b) $V = -1.61$ V, $I = 0.10$ nA, (c) $V = -2.0$ V, $I = 0.19$ nA. (d-f) Line profiles of the surface along the lines indicated in (b) and (c).

peak follows the trend observed in other iron sulfides of the surface peak being at a lower binding energy than the main peak due to lower coordination. The presence of a surface component, in contrast with the Fe 2p region, supports the conclusion that the film is sulfur-terminated.

6.3 STM

STM measurements were performed on the iron sulfide film in order to gain insight into its surface structure. The images shown in Figure 6.3 show large flat terraces that are tens of nanometers wide. These terraces contain occasional, randomly distributed defects, as well as some holes within the top layer. A line profile, shown in Figure 6.3(d), is taken through the hole in Figure 6.3(b), and gives the depth of the hole as ~ 3 Å. This is approximately the same as the height of the terraces in Figure 6.3(c), as shown in the profile in Figure 6.3(e). Figure 6.3(c) also shows a step of double height, ~ 6 Å, shown in the profile in Figure 6.3(f). The steps of height ~ 6 Å were more commonly found across the surface.

The atomic structure of the surface layer is then investigated. Figure 6.4 shows typical atomic resolution STM images taken from the iron sulfide film following preparation. The length of the surface unit cell vectors is ~ 7 Å, in agreement with the estimate made from the LEED pattern in Section 5.4.3. It can be seen that the unit cell contains four protrusions, of which three of them appear to have the same properties, in contrast with the fourth, single protrusion. That the single protrusion does not appear to be exactly centred within the space between the groups of three atoms could be due to asymmetry of the STM tip. From Figure 6.4(a), it appears that the symmetry of the surface is P3m1. This wallpaper group denotes that the unit cell has three rotation centres of order three and mirror planes passing through all three rotational centres. Additionally, glide reflections in three directions occur, with axes located halfway between adjacent parallel reflection axes. This is shown schematically in Figure 6.7(c). In the STM image, a single protrusion occurs at a centre of rotation within the unit cell, with the other three protrusions centred around another rotational centre. Figures 6.4(b) and 6.4(c) appear to show an additional 180° rotational symmetry not present in Figure 6.4(a).

It was not possible to observe an STM image such as the one in Figure 6.4(a) but rotated by 180° , though some attempt was made to find such areas because such domains could be an explanation for additional symmetry observed in I/V-curves relative to the P3m1 symmetry mentioned above, as expanded on in Section 6.4. A ~ 6 Å step between terraces is shown in Figure 6.5(a), with its line profile shown in Figure 6.5(b). The close up images from the upper and lower terraces, Figures 6.5(c) and 6.5(d) respectively, show an identical orientation. This, however, does not rule out potential 180° rotations that might be observed across steps of half the height.

Domain boundaries were observed within terraces of the iron sulfide film, and some examples are shown in Figures 6.6(a) to 6.6(c). Either side of the domain boundaries, the surface lattice is translated by half of a unit cell vector, therefore they can be considered as anti-phase domain boundaries. As shown in Figure 6.6(a), they can often be found in the vicinity of defects/holes, and may even be their cause.

STM images from iron sulfide surfaces are relatively scarce in literature, providing little for comparison. For pyrite and tetragonal FeS, the only STM

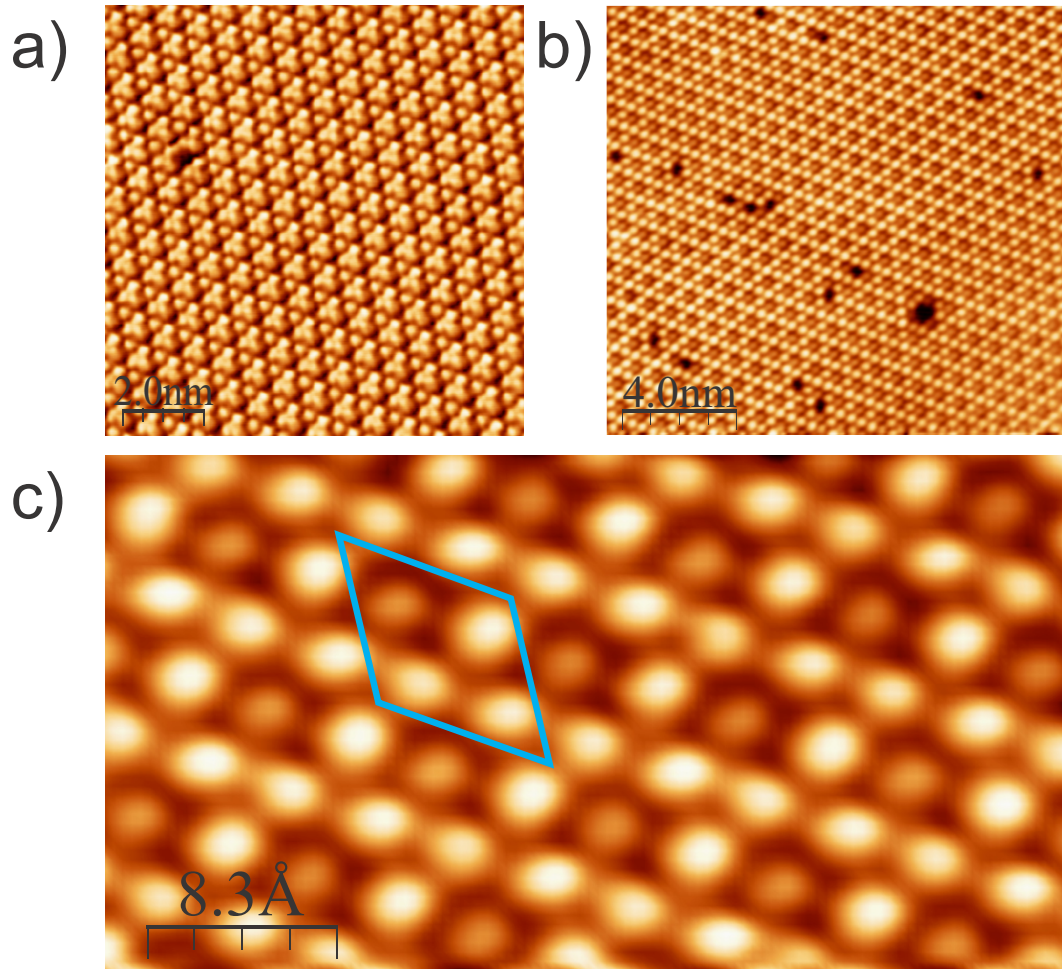


Figure 6.4: Atomic resolution STM images of the iron sulfide film surface. The surface unit cell is highlighted in (c). Tunnelling conditions: (a) bias, $V = -2.0$ V, current, $I = 1.0$ nA, (b) $V = 1.50$ V, $I = 2.50$ nA, (c) $V = 1.97$ V, $I = 5.04$ nA.

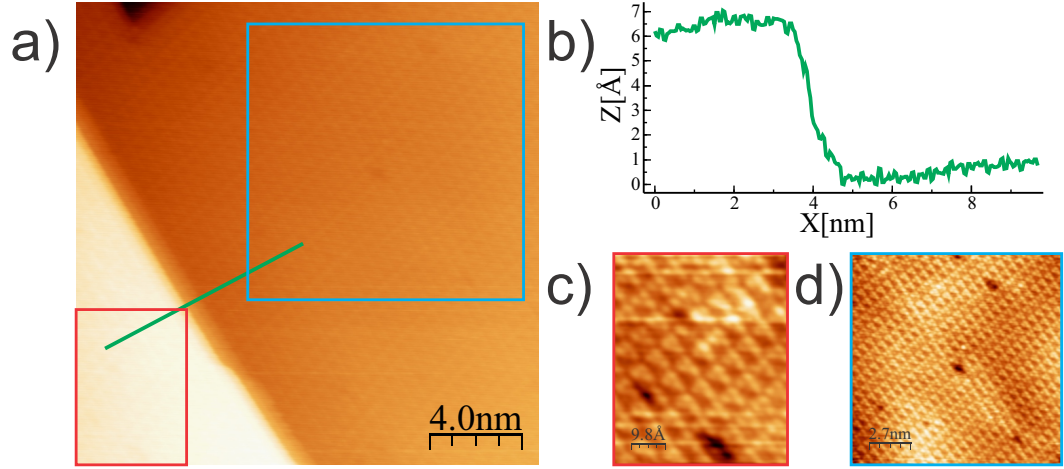


Figure 6.5: (a) STM image taken across a 6 Å step, (b) line profile along green line in (a), (c,d) close up images from the upper and lower terraces from (a) respectively, as indicated by the red and blue boxes, showing the same surface orientation across both terraces. Tunnelling conditions: bias, $V = 2.0$ V, current, $I = 1.17$ nA.

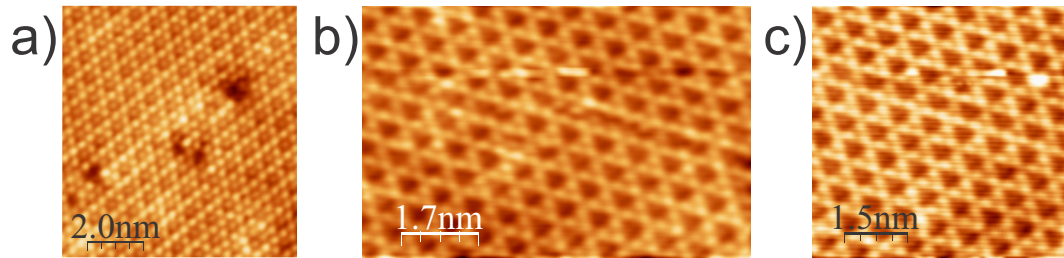


Figure 6.6: STM images showing anti-phase domain boundaries at the iron sulfide film surface. Tunnelling conditions: (a) bias, $V = -1.61$ V, current, $I = 5.0$ nA, (b,c) $V = -2.0$ V, $I = 5.0$ nA.

images found came from square (001) surfaces and therefore are not useful for comparison here [39, 117, 118]. For monoclinic Fe_7S_8 , however, a study has been performed by Becker et al. investigating its (001) surface using STM [119]. The images presented within that study show some similarities to the STM images presented here. A surface unit cell containing three sulfur atoms is presented, with the sulfur atoms producing images similar to that shown in Figure 6.6(b) when imaged with the sample biased to -3.5 V. However, a fourth protrusion as in Figure 6.4(a) is not visible in any of the images presented and it is believed that the removal of a fourth sulfur atom, when considering a bulk-like sulfur layer, leads to greater thermodynamic stability. Furthermore, in the work by Becker et al., changing the sample bias to -0.5 V made the non-equivalence of the three terminating sulfur atoms apparent. On the other hand, in the images presented in this thesis, any non-equivalence between the surface protrusions is indistinguishable from an effect of the tip or background noise, and images taken with a similar bias of -0.2 V do not show bright protrusions that could be identified with sulfur atoms. In fact, according to the calculations performed in the study of Becker et al., the non-equivalence of the surface atoms should be clear for any bias voltage between 0.0 V and -3.0 V.

Two step sizes are observed in the study on $\text{Fe}_7\text{S}_8(001)$ by Becker et al. The smallest step size presented is 2.9 Å, corresponding to the distance between two sulfur layers. Going across such a step, the orientation of the three terminating sulfur atoms is rotated by 180°. The two planes are not energetically equivalent, due to differing distances to the next Fe layer within the unit cell, therefore the large majority of steps observed are ~ 5.8 Å. $\text{Fe}_3\text{S}_4(111)$ is similar, with distances between sulfur layers of ~ 2.9 Å, and ~ 5.7 Å between equivalent layers. Likewise, the pyrrhotite system and troilite, based on a distorted NiAs-type unit cell, have comparable distances between S layers.

6.4 I/V-LEED

To attempt to reach a conclusive characterisation of the atomic structure of the surface of the film, I/V-LEED measurements and calculations were performed. The spots were assigned labels according to the convention described

in Section 2.3.3 and I/V-curves were recorded from the sample. The sample was kept at 96 K throughout the measurements to reduce background intensity, and a Helmholtz coil was used to prevent deflection of electrons by the earth's magnetic field.

Analysis of the I/V-curves showed that certain spots had the same intensity profile, as indicated by colour in Figure 6.7(a). The Au(111) surface has a P3m1 symmetry, denoting three-fold rotational symmetry with one mirror plane as shown in Figure 6.7(c). The LEED pattern from such a surface has spots of the same intensity as indicated in Figure 6.7(b). From Figure 5.13, it can be seen that the (0,1) spot of the iron sulfide film lies on the same axis as that of the Au(111) substrate indicating that the unit cell vectors of the film and the substrate point in the same directions. The symmetry of the overlying iron sulfide film must be able to achieve the symmetry observed from the I/V-curves. This could be achieved by an averaging of different rotational domains across the surface if the film contains mirrors planes rotated 30° from those of the Au(111) substrate. Alternatively, if the film does not contain the appropriate symmetry itself, a hexagonal phase at the interface with the substrate may provide a template where rotational domains rotated by 180° may exist.

Of the iron sulfides, greigite and pyrite have the approximate hexagonal unit cell size for their (111) faces to match the unit cell experimentally observed. Additionally, smythite ($\text{Fe}_{3+x}\text{S}_4(001)(0 \leq x \leq 0.3)$) has a lattice parameter of 3.465 \AA , which would correspond to a surface lattice parameter of 6.93 \AA if a (2×2) reconstruction were present. It has once been reported that troilite also has a hexagonal structure with a lattice parameter of 3.43 \AA which also would give a lattice parameter close to what is observed if there were a (2×2) reconstruction, however this was in 1925 [120] and several papers in the intervening years have given the lattice parameter as $\sim 5.97 \text{ \AA}$. A metastable cubic FeS phase also exists, with a unit cell length of 5.423 \AA , possibly leading to a (111) face with a (2×2) reconstruction and a lattice parameter of 7.67 \AA , however the high stability of the films grown in this work, even after several months in vacuum, could be considered as an argument against this phase.

The pyrrhotites, $\text{Fe}_{1-x}\text{S}(001)(0 \leq x \leq 0.125)$, contain a complex variety of stoichiometries and structures caused by ordering of Fe vacancies. They

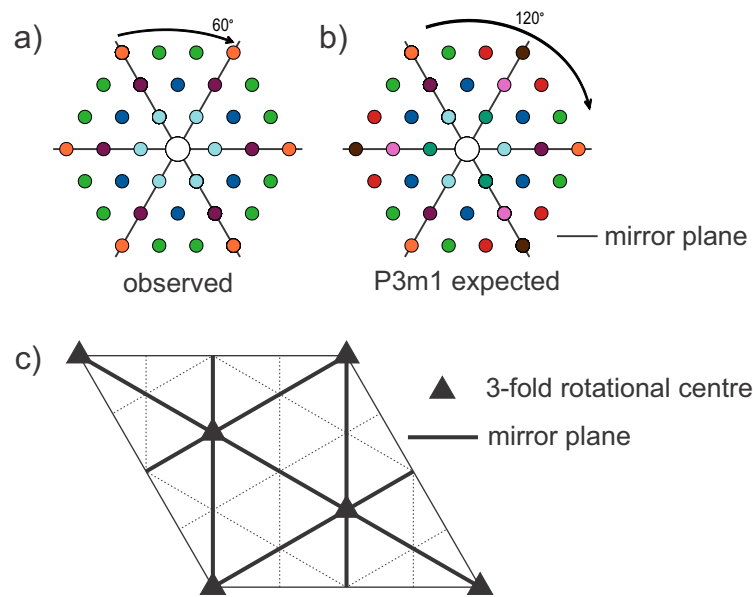


Figure 6.7: (a) Schematic diagram indicating with colour the LEED spots from the iron sulfide film whose I/V -curves show the same intensity profile, along with (b) the equivalent intensity profiles expected for a sample having $P3m1$ symmetry on a $\text{Au}(111)$ substrate. (c) 2D representation of the symmetry of a unit cell with $P3m1$ symmetry. Dashed lines in (c) indicate glide planes perpendicular to the page with the glide parallel to the plane of the page and along the line.

Table 6.2: Table showing *R*-factors from bulk greigite $\text{Fe}_3\text{S}_4(1\ 1\ 1)$ terminations.

Termination	Best <i>R</i> -factor
Fe_{kag}	0.383
Fe_{tet1}	0.364
Fe_{oct}	0.617
Fe_{tet2}	0.427
S_{S2}	0.272
S_{S1}	0.342

exist in both monoclinic and hexagonal forms derived from the NiAs unit cell structure, with the monoclinic forms being stable below ~ 525 K and the hexagonal forms only stable above this temperature or with higher Fe concentrations [121]. While the structure of monoclinic Fe_7S_8 is relatively well known, there is a wide range of structures with different arrangements of Fe vacancies for various stoichiometries within the pyrrhotite range [122] which are problematic for characterisation [123]. The symmetry observed from the I/V-curves suggests that if the film is pyrrhotite, it would be one of the hexagonal phases.

Initial calculations were performed based on possible bulk terminations of greigite $\text{Fe}_3\text{S}_4(1\ 1\ 1)$ as labelled in Figure 6.8. In order to avoid local minima, the interlayer distances of the first three atomic layers were varied for the initial starting parameters of the search procedure. Greigite exhibits the same $\text{P}3\text{m}1$ symmetry as $\text{Au}(1\ 1\ 1)$, therefore the intensity of the $(0, 1)$ and $(1, 0)$ spots were averaged together to produce the curves with the observed symmetry. These initial calculations were done using a dataset measured from 50 to 350 eV. Adding together the range of energies measured for each set of equivalent spots, the total energy range of the curves for comparison with the calculated structures was 1212 eV. The *R*-factors obtained are shown in Table 6.2.

As can be seen from Table 6.2, the bulk termination that produced the lowest *R*-factor was with the S_{S2} layer with the S_{tri2} layer above the Fe_{tet2} layer (see Figure 6.8 for layer naming scheme). This was followed by the S_{tri1} layer with the S_{S1} atom above the Fe_{kag} layer. Together, this appears to suggest that the surface may be sulfur-terminated, however the *R*-factor of 0.272 is still too high to conclude that the model accurately represents the structure of the surface of the film.

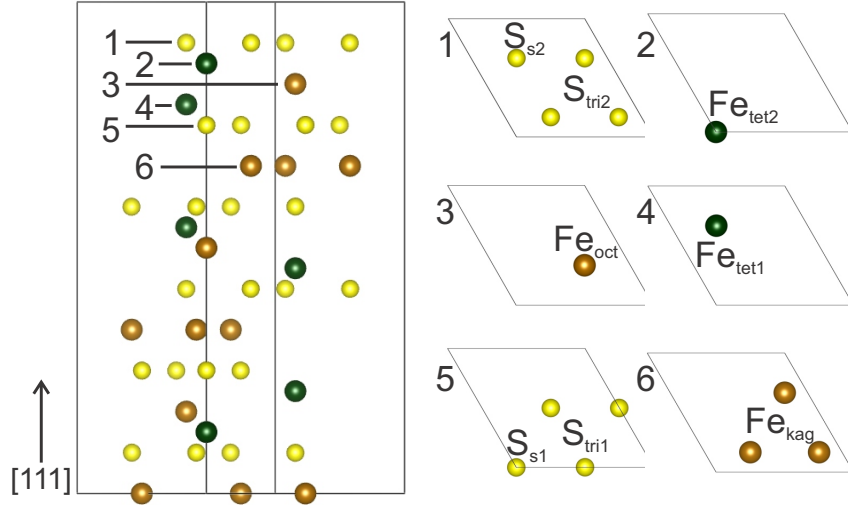


Figure 6.8: $\text{Fe}_3\text{S}_4(111)$ unit cell, with top view of layers 1-6, showing the naming of the atoms or groups of atoms. The layers 1-6 are repeated, shifted laterally to lie around the different rotational centres.

Bulk terminations for pyrite $\text{FeS}_2(111)$ were also trialled, and the results from these calculations are shown in Table 6.3. The best R-factor achieved was 0.464, however the symmetry of the (111) plane in pyrite is $P3$, leading to difficulties rationalising the observed symmetry of the I/V-curves. Additionally, the (001) surface of pyrite is the most energetically favourable and the double bonds between the sulfur atoms make it unlikely that the (111) surface would have grown on the $\text{Pt}(001)$ substrate as seen in Section 5.4.2.

For smythite $\text{Fe}_{3+x}\text{S}_4(001)$ ($0 \leq x \leq 0.3$), a (2×2) reconstruction was simulated by doubling the unit cell vectors for the top layers and vertically displacing atoms that lay at rotational centres of symmetry. The place where it would be expected that the bulk structure is terminated is between the consecutive S layers, satisfying the Tasker conditions for neutrality of the surface.

Table 6.3: Table showing R-factors from bulk pyrite $\text{FeS}_2(111)$ terminations.

Termination	Best R-factor
Fe	0.502
Single S above Fe	0.464
Double S layer	0.499
Between the two S layers	0.556

Smythite also has a glide plane which would produce the observed symmetry of the I/V-curves, however the best R-factor achieved for smythite was only 0.541.

The troilite FeS structure given by Alsen [120] was also trialled using a (2×2) reconstruction constructed in the same way as for smythite. As a hexagonal phase with symmetry $P6_3mmc$ (space group 194), it would clearly lead to the correct symmetry for the intensities of the I/V-curves, though it would be difficult to explain the prevalence of double steps observed in STM. From the calculations using modified bulk terminations, the best R-factor obtained was 0.447.

Hexagonal pyrrhotite Fe_7S_8 -3C with the structure given by Nakano et al [124] was also trialled. Here, the 3C signifies that within the Fe_7S_8 unit cell the ordering of the Fe vacancies takes place over 3 subcells of the NiAs-like structure along the c -axis. This structure is trigonal, with $P3Fe_121$ symmetry, which gives the apparent space group $P6_222$ when twin-related domains are considered. Bulk terminations consisting of either 3 or 4 sulfur or iron atoms allowed to vary according to the search procedure. The best R-factor obtained was 0.416, from a structure which contained 4 sulfur atoms in the topmost layer.

Having tried the bulk-like terminations for the above materials without a satisfactory conclusion, attention was then turned towards various reconstructions and rearrangements of the surface layers. $Fe_3S_4(111)$ had given the best R-factors, and it is clear that the optimum configurations consisted of sulfur terminated layers.

Theoretical calculations of the surface structure of $Fe_3S_4(111)$ have been performed by Roldan and de Leeuw to investigate water dissociation on greigite surfaces [125]. They found that the optimum surface structures for the (111) surface consisted of either an Fe_{oct} terminated film or a film terminated by the Fe_{kag} layer. However, they found that when they allowed the surface to relax, the terminating Fe atoms moved into the subsurface, leaving a sulfur termination and an accumulation of Fe beneath the sulfur layer. From this, it is surmised that there may be a tendency for additional Fe to be present in subsurface layers. Additionally, Fe_3S_4 may easily accommodate additional Fe in interstitial sites in a manner similar to Fe_3O_4 or as seen in the range of

stoichiometries of the pyrrhotite system.

Structures similar to those calculated by Roldan and de Leeuw were used as trial structures, which were then optimised and allowed to relax. The Fe_{oct} termination with the Fe_{oct} and Fe_{tet1} atoms moved beneath the S_{s1} and S_{tri1} layers yielded an R-factor of 0.486. Removing the Fe_{oct} atom from this structure lowered the R-factor slightly, to 0.479. The other termination, with an Fe_{kag} layer instead moving beneath the sulfur layer, gave an R-factor of 0.488. Adding a single Fe_{tet1} atom to the topmost Fe_{kag} layer of the S_{s1} bulk termination resulted in an R-factor of 0.383.

Other trial structures were attempted with variations of bulk structures. A structure was trialled with an Fe_{kag} layer termination, with an additional S atom placed in the space between the triplets of Fe atoms. Following optimisation, the best R-factor achieved was 0.411.

A structure was tried where layers 5 and 6 in Figure 6.8 were repeated, with layer 5 terminating the film. This resulted in an R-factor of 0.293, which is similar to the best R-factor obtained for the bulk-like terminations. Again, noting the perceived tendency for Fe to gather in the subsurface region in the calculations of Roldan and de Leeuw, an additional Fe atom was placed in the topmost Fe_{kag} layer. This led to a reduction in the R-factor to 0.178, with the I/V-curves shown in Figure 6.9(a).

The calculations yielding this R-factor allowed 20 parameters describing atomic positions to be varied, as well as the lattice parameter and the u parameter describing the position of the sulfur atoms within the unit cell. In addition to this, the Debye temperatures and the imaginary part of the inner potential were optimised, giving a total of 27 parameters varied. This number of parameters, in conjunction with a total energy range of only 1212 eV, suggest that an R-factor of 0.178 is not sufficient to have confidence that the trial structure is correct. To overcome this hurdle, experimental data from larger range of 1807 eV was used and the calculations were rerun. Following optimisation using the differential evolution algorithm, the best R-factor achieved was 0.272, and the I/V-curves are shown in Figure 6.9(b). This shows that the model does not accurately reflect the surface structure of the film because the model does poorly at predicting the curves outside of the initial fitting range, though there may be aspects which closely resemble the true structure.

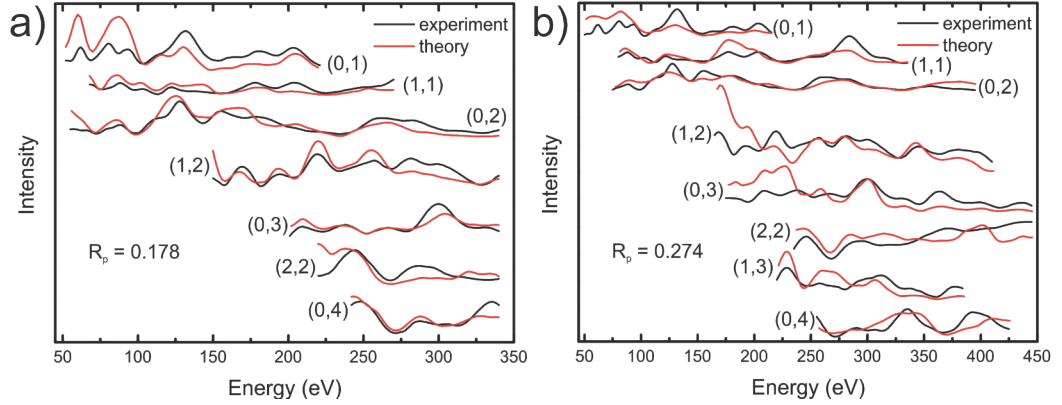


Figure 6.9: I/V -curves from the reconstructed greigite surface (a) giving an R -factor of 0.178 for a total fitting range of 1212 eV, and (b) over an extended range of 1807 eV giving an R -factor of 0.272.

6.5 X-ray diffraction

Due to the difficulties in determining the surface structure of the iron sulfide film with I/V -LEED caused by the large parameter space that needs to be searched, an XRD experiment was performed in the X-ray Physics and Nanoscience department of the DESY Research Centre in Hamburg. An iron sulfide film was grown using the recipe outlined in Chapter 5 and was transported to Hamburg within a small vacuum chamber with a battery-powered ion pump. The sample was kept at pressures below 1×10^{-7} mbar for the duration of the transfers between chambers and throughout the transport between the institutions.

Several reflections and their symmetry equivalent reflections were measured and the observed structure factors F_{obs} were deduced using Lorentz, polarisation, and intercepted beam corrections. These are listed in Table 6.4. The experimental error dF was taken from the range of intensities measured for symmetry equivalent reflections. The XRD measurements revealed that the film had unit cell parameters $a = b = 3.48 \pm 0.05$ Å, $c = 5.85 \pm 0.05$ Å, taking the Au lattice parameters as a reference. Indexing of the spots and their symmetry show that the film belonged to the hexagonal space group 186

Table 6.4: Table showing the measured intensities (in counts) of the reflections F_{obs} , their error dF , and the value calculated for the model F_{calc} . The model gives a final R -value of 0.182.

Reflection	F_{obs}	dF	F_{calc}	$ F_{calc}-F_{obs} /F_{obs}$
(100)	280.92	42.60	169.96	0.39
(110)	463.69	36.90	483.03	0.04
(200)	136.26	20.44	127.20	0.07
(101)	215.25	15.10	172.64	0.20
(201)	115.02	10.60	127.32	0.11
(102)	327.44	82.70	328.62	0.00
(112)	53.89	8.08	63.59	0.18
(202)	174.39	40.70	254.91	0.46

($P6_3mc$). These unit cell parameters reveal that the ~ 7 Å periodicity observed in LEED and STM is as a result of a (2×2) surface reconstruction. The space group, $P6_3mc$, requires that the stacking of the structure in the c direction is AbAc, and the best fit to the data is a film that has a NiAs structure. The refinement of the structural model was done using three parameters: the Fe occupancy, the z coordinate of the S atoms, and an overall scale factor. The calculated structure factors F_{calc} for the best fit structure are given in Table 6.4. The final R -value for the best fit to the data was $R = 18.1$ %.

Table 6.5 presents the refined atomic positions of the best fit to the observed diffraction peaks. Interestingly, following optimisation of the fitted structure, the Fe occupancy is given as 77.6 %, giving a stoichiometry of almost Fe_3S_4 . This agrees with the XPS results presented in Section 6.2, as the S 2p spectra show the prevalence of five-fold coordinated S, which would not be present in stoichiometric FeS in the NiAs structure, and the Fe 2p spectra show the presence of both Fe^{2+} and Fe^{3+} ions. Although the Fe occupancy requires almost half of the unit cells in the film to have an Fe vacancy, no superstructure reflections were observed. This means that either the Fe vacancies are not ordered, or that the superstructure reflections are too weak to be detected in the experimental set-up used.

As seen in Table 6.5, the z -coordinate of the sulfur atoms is 0.26. This asymmetry of the S atoms around the Fe layers may help to explain the prevalence of 6 Å steps observed in STM images, though the two sulfur layers do have the same distance to the Fe layer below them.

As mentioned above, the pyrrhotite system, $Fe_{1-x}S(001)(0 \leq x \leq$

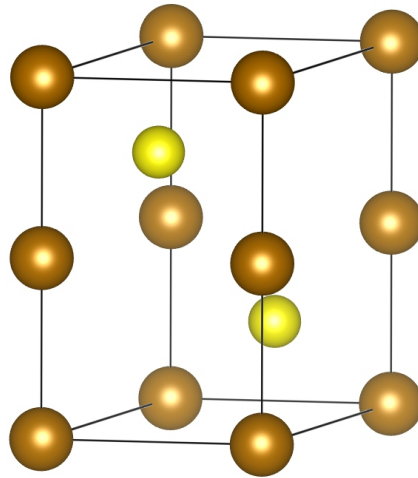


Figure 6.10: NiAs structure of the iron sulfide film as determined by XRD.

0.125), is based on the NiAs unit cell structure, with various distortions and superstructures present due to Fe vacancies. In the case of the film presented here, no superstructures were observed, though this may be due to a weak signal from those diffraction spots. Additionally, it could be possible that there is more Fe within the film that remains disordered, at least at room temperature.

Interestingly, the addition of Fe to the film as shown in Section 5.4.3 led to a periodicity of ~ 6.0 Å being observed in LEED patterns, as displayed in Figure 5.15. Perhaps this additional Fe filled vacancies near the surface and led to a local stoichiometry of FeS, leading to the distortion of the NiAs lattice present in troilite.

Table 6.5: Table showing the refined atomic positions of the best fit to the XRD measurements.

Atom	Occupancy	Multiplicity	Position
Fe	0.776	2	(0, 0, 0)
S	1	2	(1/3, 2/3, 0.26)

6.6 Conclusions

The iron sulfide film has been analysed using a combination of XPS, STM, I/V-LEED, and XRD. The XRD measurements revealed that the bulk structure of the film had a nickeline structure with $P6_3mc$ symmetry and provided lattice parameters of $a = b = 3.48 \pm 0.05 \text{ \AA}$, $c = 5.85 \pm 0.05 \text{ \AA}$. XPS, STM, and I/V-LEED point towards a S terminated film, while XPS agrees with the conclusion from XRD that the film is substoichiometric, with the optimal result from fitting the XRD data giving an Fe occupancy of 77 %. STM and LEED give a surface lattice parameter of $\sim 7 \text{ \AA}$, revealing that the surface undergoes a (2×2) reconstruction.

Chapter 7

Summary and Conclusions

This thesis has investigated the growth of iron oxide and iron sulfide thin films. In Chapter 4, a preparation method was developed for the growth of $\text{Fe}_3\text{O}_4(001)$ films using MBE on a $\text{Pt}(001)$ substrate. This first preparation of well ordered $\text{Fe}_3\text{O}_4(001)$ films on a metallic substrate enables further investigations to be performed using techniques which are unavailable for single crystal samples or films grown on insulating substrates. It was found that an Fe buffer layer was required for growth of the (001) face of Fe_3O_4 films, with growth of the two most stable terminations of $\text{Fe}_3\text{O}_4(001)$ being achieved. The surface termination could be tuned via variation of the thickness of this buffer layer, as the Fe within the film was found to be mobile and easily migrated into the Pt substrate, meaning that the excess Fe present with a thicker buffer layer was able to stabilise the more Fe-rich termination of the film.

Following this, growth of iron sulfide films was studied. Chapter 5 presents the process by which a growth recipe for a highly ordered iron sulfide film was discovered. Iron was deposited from an MBE source, while sulfur was provided by an electrochemical cell. Initially, platinum substrates were used because of the small lattice mismatch with greigite, one of the range of iron sulfides. It was found that although it was possible to grow a film on $\text{Pt}(001)$, it was not stable and decomposed at temperatures that were too low for the film to become well-ordered. Eventually, using a $\text{Au}(111)$ substrate, it was possible to grow a high-quality iron sulfide film.

In Chapter 6, the iron sulfide film was characterised using a variety of techniques. XPS and I/V-LEED suggest that the film is sulfur terminated,

and the surface unit cell parameter was approximated to ~ 7 Å according to LEED and STM, with STM images also exhibiting interlayer distances of ~ 3 Å and predominantly double-layer step heights. XPS showed that the film contained both Fe^{2+} and Fe^{3+} ions, and that it contained both 5-fold and 6-fold coordinated sulfur atoms. XRD measurements showed that the film had $\text{P6}_3\text{mc}$ symmetry, with unit cell parameters $a = b = 3.48 \pm 0.05$ Å, $c = 5.85 \pm 0.05$ Å and a NiAs structure. The surface undergoes a (2×2) reconstruction, and the Fe occupancy was given as 77 %. This new growth recipe for well-ordered iron sulfide thin films paves the way for future investigations into this complex material system using surface science techniques.

Bibliography

- [1] W. Ostwald, *Über katalyse*, No. 200 (Akademische verlagsgesellschaft mbh, 1923).
- [2] C. R. Catlow, M. Davidson, C. Hardacre, and G. J. Hutchings, Philosophical Transactions of the Royal Society A: Mathematical, Physical and Engineering Sciences **374**, 20150089 (2016).
- [3] I. Langmuir, Trans. Faraday Soc. **17**, 607 (1922).
- [4] G. Ertl, Angewandte Chemie International Edition **47**, 3524 (2008).
- [5] D. Goodman, Surface Review and Letters **02**, 9 (1995).
- [6] H.-J. Freund, Rendiconti Lincei **28**, 5 (2017).
- [7] H.-J. Freund, H. Kuhlenbeck, and V. Staemmler, Reports on Progress in Physics **59**, 283 (1996).
- [8] S. A. Chambers, Surface Science Reports **39**, 105 (2000).
- [9] H. Lüth, *Solid Surfaces, Interfaces and Thin Films*, Graduate Texts in Physics No. v. 3 (Springer Berlin Heidelberg, Berlin, Heidelberg, 2010).
- [10] K. Oura, M. Katayama, A. V. Zotov, V. G. Lifshits, and A. A. Saranin, *Surface Science*, Advanced Texts in Physics (Springer Berlin Heidelberg, Berlin, Heidelberg, 2003).
- [11] P. W. Tasker, Journal of Physics C: Solid State Physics **12**, 4977 (1979).
- [12] R. M. Cornell and U. Schwertmann, *The Iron Oxides* (Wiley-VCH Verlag GmbH & Co. KGaA, Weinheim, FRG, 2003).

- [13] C. H. Bartholomew and R. J. Farrauto, *Fundamentals of Industrial Catalytic Processes* (John Wiley & Sons, Inc., Hoboken, NJ, USA, 2005).
- [14] D. G. Rethwisch and J. A. Dumesic, *Applied Catalysis* **21**, 97 (1986).
- [15] W. Lowrie, *Fundamentals of geophysics* (Cambridge university press, 2007).
- [16] E. J. Verwey and P. W. Haayman, *Physica* **8**, 979 (1941).
- [17] M. L. Néel, *Annales de Physique* **12**, 137 (1948).
- [18] A. Yanase and K. Siratori, *Journal of the Physical Society of Japan* **53**, 312 (1984).
- [19] A. Yanase and N. Hamada, *Journal of the Physical Society of Japan* **68**, 1607 (1999).
- [20] Z. Zhang and S. Satpathy, *Physical Review B* **44**, 13319 (1991).
- [21] G. S. Parkinson, *Surface Science Reports* **71**, 272 (2016).
- [22] T. Kendelewicz, P. Liu, C. Doyle, G. Brown, E. Nelson, and S. Chambers, *Surface Science* **453**, 32 (2000).
- [23] R. Bliem, E. McDermott, P. Ferstl, M. Setvin, O. Gamba, J. Pavelec, M. A. Schneider, M. Schmid, U. Diebold, P. Blaha, L. Hammer, and G. S. Parkinson, *Science* **346**, 1215 (2014).
- [24] N. Spiridis, E. Madej, and J. Korecki, *The Journal of Physical Chemistry C* **4**, 2011 (2014).
- [25] J. P. LaFemina, *Crit. Rev. Surf. Chem* **3**, 297 (1994).
- [26] Y. Kim, Y. Gao, and S. Chambers, *Surface Science* **371**, 358 (1997).
- [27] G. Tarrach, D. Bürgler, T. Schaub, R. Wiesendanger, and H. J. Güntherodt, *Surface Science* **285**, 1 (1993).
- [28] F. Voogt, T. Fujii, P. Smulders, L. Niesen, M. James, and T. Hibma, *Physical Review B* **60**, 11193 (1999).

- [29] B. Stanka, W. Hebenstreit, U. Diebold, and S. A. Chambers, *Surface Science* **448**, 49 (2000).
- [30] H. A. Jahn and E. Teller, *Proceedings of the Royal Society A: Mathematical, Physical and Engineering Sciences* **161**, 220 (1937).
- [31] R. Pentcheva, F. Wendler, H. L. Meyerheim, W. Moritz, N. Jedrecy, and M. Scheffler, *Physical Review Letters* **94**, 126101 (2005).
- [32] X. Yu, C. F. Huo, Y. W. Li, J. Wang, and H. Jiao, *Surface Science* **606**, 872 (2012).
- [33] G. S. Parkinson, Z. Novotný, P. Jacobson, M. Schmid, and U. Diebold, *Surface Science* **605**, L42 (2011).
- [34] N. Spiridis, J. Barbasz, Z. Łodziana, and J. Korecki, *Physical Review B* **74**, 155423 (2006).
- [35] Z. Novotny, N. Mulakaluri, Z. Edes, M. Schmid, R. Pentcheva, U. Diebold, and G. S. Parkinson, *Physical Review B* **87**, 195410 (2013).
- [36] D. Rickard and G. W. Luther, *Chemical Reviews* **107**, 514 (2007).
- [37] R. S. C. Smart, J. Amarantidis, W. M. Skinner, C. A. Prestidge, L. La Vanier, and S. R. Grano, in *Solid-Liquid Interfaces* (Springer, Berlin, Heidelberg, 2003) pp. 3–62.
- [38] A. G. Tomkins and B. Morgan, “Sulfide minerals,” in *Encyclopedia of Geochemistry: A Comprehensive Reference Source on the Chemistry of the Earth*, edited by W. M. White (Springer International Publishing, Cham, 2017) pp. 1–3.
- [39] R. Murphy and D. R. Strongin, *Surface Science Reports* **64**, 1 (2009).
- [40] D. Rickard, *Sulfidic Sediments and Sedimentary Rocks*, *Developments in Sedimentology* (Elsevier Science, 2012).
- [41] G. Cody, N. Boctor, J. Brandes, T. Filley, R. Hazen, and H. Yoder, *Geochimica et Cosmochimica Acta* **68**, 2185 (2004).

- [42] G. D. Cody, Annual Review of Earth and Planetary Sciences **32**, 569 (2004).
- [43] M. A. Schoonen and Y. Xu, Astrobiology **1**, 133 (2001).
- [44] G. Wächtershäuser, Microbiological reviews **52**, 452 (1988).
- [45] G. Wächtershäuser, Proceedings of the National Academy of Sciences of the United States of America **87**, 200 (1990).
- [46] G. Wächtershäuser, Progress in Biophysics and Molecular Biology **58**, 85 (1992).
- [47] G. Wächtershäuser, Proceedings of the National Academy of Sciences **91** (1994).
- [48] G. Wächtershäuser, in *Thermophiles: the keys to molecular evolution and the origin of life?*, edited by J. Wiegel and A. W. Michael (Taylor & Francis, 1998) Chap. 4, pp. 47–57.
- [49] M. J. Russell, A. J. Hall, A. G. Cairns-Smith, and P. S. Braterman, Nature **336**, 117 (1988).
- [50] M. J. Russell, A. J. Hall, and D. Turner, Terra Nova **1**, 238 (1989).
- [51] M. J. Russell and A. J. Hall, Journal of the Geological Society **154**, 377 (1997).
- [52] M. J. Russell, D. E. Daia, and A. J. Hall, in *Thermophiles: the keys to molecular evolution and the origin of life?*, edited by J. Wiegel and A. W. Michael (Taylor & Francis, 1998) Chap. 6, pp. 77–126.
- [53] B. J. Skinner, R. C. Erd, and F. S. Grimaldi, The American Mineralogist **49**, 543 (1964).
- [54] U.-P. Apfel and W. Weigand, Angewandte Chemie International Edition **50**, 4262 (2011).
- [55] A. Yamaguchi, M. Yamamoto, K. Takai, T. Ishii, K. Hashimoto, and R. Nakamura, Electrochimica Acta **141**, 311 (2014).

- [56] A. Roldan, N. Hollingsworth, A. Roffey, H.-U. Islam, J. B. M. Goodall, C. R. a. Catlow, J. a. Darr, W. Bras, G. Sankar, K. B. Holt, G. Hogarth, and N. H. de Leeuw, *Chemical Communications* **51**, 7501 (2015).
- [57] M. J. Russell, R. M. Daniel, A. J. Hall, and J. A. Sherringham, *Journal of Molecular Evolution* **39**, 231 (1994).
- [58] M. J. Russell and W. Martin, *Trends in Biochemical Sciences* **29**, 358 (2004).
- [59] G. Wächtershäuser, *Chemistry & Biodiversity* **4**, 584 (2007).
- [60] N. Lane and W. F. Martin, *Cell* **151**, 1406 (2012).
- [61] H. Nesbitt, A. Schaufuss, M. Scaini, G. Bancroft, and R. Szargan, *American Mineralogist* **86**, 318 (2001).
- [62] M. Becker, J. de Villiers, and D. Bradshaw, *Economic Geology* **105**, 1025 (2010).
- [63] M. Becker, *The Mineralogy and Crystallography of Pyrrhotite from Selected Nickel and PGE Ore Deposits and its Effect on Flotation Performance*, Dphil, University of Pretoria (2009).
- [64] D. Trioli, *Il Ragionamento della Caduta di un Sasso dall’Aria difeso in una Lettera Apologetica* (Eredi di Bart. Soliani, Modena, Italy, 1766) p. 120.
- [65] N. Takahashi, Y. Nakatani, T. Yatomi, and T. Nakamura, *Chemistry of Materials* **15**, 1763 (2003).
- [66] M. P. Seah and W. A. Dench, *Surface and Interface Analysis* **1**, 2 (1979).
- [67] N. Fairley, <http://www.casaxps.com> (2010).
- [68] T. Koopmans, *Physica* **1**, 104 (1934).
- [69] J. C. Vickerman, *Surface Analysis: The Principal Techniques*, edited by J. C. Vickerman and I. S. Gilmore (John Wiley & Sons, Ltd, Chichester, UK, 2009).

- [70] K. Siegbahn, C. Nordling, A. Fahlman, R. Nordberg, K. Hamrim, J. Hedman, C. Johansson, T. Bergmark, S. E. Karlsson, I. Lindgren, and B. Lindberg, *Nov. Act. Uppsaliensis*, Nova acta Regiae Societatis Scientiarum Upsaliensis, (Almqvist & Wiksells, Uppsala, 1967).
- [71] D. A. Shirley, Physical Review B **5**, 4709 (1972).
- [72] M. Seah and M. Anthony, Surface and Interface Analysis **6**, 24 (1984).
- [73] J. Yeh and I. Lindau, Atomic Data and Nuclear Data Tables **32**, 1 (1985), arXiv:1203.4508 .
- [74] S. Tanuma, C. J. Powell, and D. R. Penn, Surface and Interface Analysis **21**, 165 (1994).
- [75] G. Binnig, H. Rohrer, C. Gerber, and E. Weibel, Physical review letters **49**, 57 (1982).
- [76] M. A. Van Hove and S. Y. Tong, *Surface Crystallography by LEED*, Springer Series in Chemical Physics, Vol. 2 (Springer Berlin Heidelberg, Berlin, Heidelberg, 1979).
- [77] J. B. Pendry, *Low energy electron diffraction* (Academic Press, London, 1974).
- [78] J. B. Pendry, Journal of Physics C: Solid State Physics **4**, 3095 (1971).
- [79] J. B. Pendry, Journal of Physics C: Solid State Physics **13**, 937 (1980).
- [80] M. J. D. Powell, The Computer Journal **7**, 155 (1964).
- [81] P. Rous and J. Pendry, Computer Physics Communications **54**, 137 (1989).
- [82] P. Rous and J. Pendry, Computer Physics Communications **54**, 157 (1989).
- [83] P. Rous and J. Pendry, Surface Science **219**, 355 (1989).
- [84] R. Storn and K. Price, Journal of Global Optimization **11**, 341 (1997).

- [85] E. Primorac, H. Kuhlenbeck, and H. J. Freund, *Surface Science* **649**, 90 (2016).
- [86] M. Fonin, R. Pentcheva, Y. S. Dedkov, M. Sperlich, D. V. Vyalikh, M. Scheffler, U. Rüdiger, and G. Güntherodt, *Physical Review B - Condensed Matter and Materials Physics* **72**, 104436 (2005).
- [87] M. Ritter, H. Over, and W. Weiss, *Surface Science* **371**, 245 (1997).
- [88] K. He, L. Zhang, X. Ma, J. Jia, Q. Xue, and Z. Qiu, *Physical Review B* **72**, 155432 (2005).
- [89] S. Shaikhutdinov, M. Ritter, and W. Weiss, *Physical Review B* **62**, 7535 (2000).
- [90] N. G. Condon, F. M. Leibsle, T. Parker, A. R. Lennie, D. J. Vaughan, and G. Thornton, *Physical Review B* **55**, 15885 (1997).
- [91] S. K. Shaikhutdinov, M. Ritter, X. G. Wang, H. Over, and W. Weiss, *Physical Review B - Condensed Matter and Materials Physics* **60**, 11062 (1999).
- [92] G. H. Vurens, V. Maurice, M. Salmeron, and G. A. Somorjai, *Surface Science* **268**, 170 (1992).
- [93] M. G. Willinger, W. Zhang, O. Bondarchuk, S. Shaikhutdinov, H.-J. Freund, and R. Schlögl, *Angewandte Chemie International Edition* **53**, 5998 (2014).
- [94] C. Wagner, *The Journal of Chemical Physics* **21**, 1819 (1953).
- [95] W. Heegemann, K. Meister, E. Bechtold, and K. Hayek, *Surface Science* **69**, 1 (1975).
- [96] D. Detry and J. Drowart, *Zeitschrift für Physikalische Chemie* **55**, 314 (1967).
- [97] A. Roldan, N. Hollingsworth, A. Roffey, H.-U. Islam, J. B. M. Goodall, C. R. a. Catlow, J. a. Darr, W. Bras, G. Sankar, K. B. Holt, G. Hogarth, and N. H. de Leeuw, *Chemical Communications* **51**, 7501 (2015).

- [98] L. E. Davis, N. C. MacDonald, P. W. Palmberg, G. E. Riach, and R. E. Weber, *Handbook of Auger electron spectroscopy* (Physical Electronics Division, Perkin-Elmer Corporation, Eden Prairie, MN, 1976).
- [99] D. I. Jerdev and B. E. Koel, *Surface Science* **513**, 1 (2002).
- [100] H. Okamoto, *Journal of Phase Equilibria & Diffusion* **25**, 395 (2004).
- [101] J. R. Mycroft, G. M. Bancroft, N. S. McIntyre, J. W. Lorimer, and I. R. Hill, *J. Electroanal. Chem. Interfacial Electrochem.* **292**, 139 (1990).
- [102] N. S. McIntyre, R. D. Davidson, and J. R. Mycroft, *Surface and Interface Analysis* **24**, 591 (1996).
- [103] A. Pratt, I. Muir, and H. Nesbitt, *Geochimica et Cosmochimica Acta* **58**, 827 (1994).
- [104] M. Mullet, S. Boursiquot, M. Abdelmoula, J. M. Génin, and J. J. Ehrhardt, *Geochimica et Cosmochimica Acta* **66**, 829 (2002).
- [105] J. E. Thomas, W. M. Skinner, and R. S. Smart, *Geochimica et Cosmochimica Acta* **67**, 831 (2003).
- [106] H. W. Nesbitt, M. Scaini, H. Höchst, G. M. Bancroft, A. G. Schaufuss, and R. Szargan, *American Mineralogist* **85**, 850 (2000).
- [107] J. M. Guevremont, A. R. Elsetinow, D. R. Strongin, J. Bebie, and M. A. Schoonen, *American Mineralogist* **83**, 1353 (1998).
- [108] R. P. Gupta and S. K. Sen, *Physical Review B* **12**, 15 (1975).
- [109] W. M. Skinner, H. W. Nesbitt, and A. R. Pratt, *Geochimica et Cosmochimica Acta* **68**, 2259 (2004).
- [110] S. Mlowe, N. S. Osman, T. Moyo, B. Mwakikunga, and N. Revaprasadu, *Materials Chemistry and Physics* **198**, 167 (2017).
- [111] H. W. Nesbitt, *American Mineralogist* **83**, 1067 (1998).
- [112] J. a. Leiro, S. S. Mattila, and K. Laajalehto, *Surface Science* **547**, 157 (2003).

- [113] S. Mattila, J. a. Leiro, and K. Laajalehto, *Applied Surface Science* **212-213**, 97 (2003).
- [114] G. U. von Oertzen, W. M. Skinner, and H. W. Nesbitt, *Radiation Physics and Chemistry* **75**, 1855 (2006).
- [115] M. Bronold, Y. Tomm, and W. Jaegermann, *Surface Science* **314**, 0 (1994).
- [116] A. G. Schaufuß, H. W. Nesbitt, I. Kartio, K. Laajalehto, G. M. Bancroft, and R. Szargan, *Surface Science* **411**, 321 (1998).
- [117] X. Yang, Z. Du, G. Du, Q. Gu, H. Lin, D. Fang, H. Yang, X. Zhu, and H. H. Wen, *Physical Review B* **94**, 1 (2016).
- [118] K. Zhao, H.-C. Lin, W.-T. Huang, X.-P. Hu, X. Chen, Q.-K. Xue, and S.-H. Ji, *Chinese Physics Letters* **34**, 087401 (2017).
- [119] U. Becker, A. W. Munz, R. Lennie, G. Thornton, and D. J. Vaughan, *Surface Science* **389**, 66 (1997).
- [120] N. Alsén, *Geologiska Föreningen i Stockholm Förhandlingar* **47**, 19 (1925).
- [121] D. J. Vaughan and C. L. Corkhill, *Elements* **13**, 81 (2017).
- [122] Z. Izaola, S. González, L. Elcoro, J. M. Perez-Mato, G. Madariaga, and A. García, *Acta Crystallographica Section B Structural Science* **63**, 693 (2007).
- [123] D. Harries, K. Pollok, and F. Langenhorst, *American Mineralogist* **96**, 716 (2011).
- [124] A. Nakano, M. Tokonami, and N. Morimoto, *Acta Crystallographica Section B Structural Crystallography and Crystal Chemistry* **35**, 722 (1979).
- [125] A. Roldan and N. H. de Leeuw, *Proceedings of the Royal Society A: Mathematical, Physical and Engineering Science* **472**, 20160080 (2016).